To the Graduate Council:

I am submitting herewith a dissertation written by Michael John Felty entitled "Adsorption of Propane on the Magnesium Oxide (100) Surface and Synthesis of Anodized Aluminum Oxide." I have examined the final electronic copy of this dissertation for form and content and recommend that it be accepted in partial fulfillment of the requirements for the degree of Doctor of Philosophy, with a major in Chemistry.

John Z. Larese

Major Professor

We have read this dissertation
and recommend its acceptance:

T. Ffrancon Williams

George Kabalka

Norman Mannella

Accepted for the Council

Carolyn R. Hodges
Vice President and Dean of the
Graduate School

(Original signatures are on file with official student records)

Adsorption of Propane on the Magnesium Oxide (100) Surface

and

Synthesis of Anodized Aluminum Oxide

A Dissertation
Presented for the
Doctor of Philosophy Degree
University of Tennessee, Knoxville

Michael John Felty
December 2008

Copyright © 2008 by Michael John Felty.
All rights reserved.

Dedication

To my loving family,

as Grandma always says

“Friends can come and go, but

Family is the one constant in your life.”

Acknowledgements

First, let me say that too many people to list have made this journey possible, and I apologize for leaving anybody out. Please know that I have a special place in my heart for each one of you and will never forget the help you have given me.

I must first thank my parents, Jeanne and Danny. I probably do not want to know all the sacrifices that you two have made to help me accomplish my goals. I only hope that I will show the same amount of selfless love, devotion, and loyalty to my own children one day. I must also thank you both for not making me feel guilty for vegging out on the couch in front of the television when I came home to visit.

Many thanks go to my two sisters, Ellen and Laura. The last few years have been a whirlwind, but as mom says, we are building character. I do not know about you, but I feel I have enough character. Ellen, thank you so much for going out of your way in helping me with my car problems. I hope that it will not be too much longer when I can tell you I have a new car; instead of calling to pick me up on the side of the interstate.

I also need to thank my mother-in-law, Syble, and sister-in-law, Kathy. The two of you have made my life more enjoyable since I have gotten to know you. Syble, the

past couple of years would have been insurmountable if it was not for you. Thank you for everything that you have done.

I must also thank my first chemistry teacher, Angela Biggs, and first research advisor, Thandi Buthelezi. Mrs. Biggs, without you, I would never have appreciated the world of chemistry. I hope that when I am standing in front of a classroom full of students, I will be able to impart the same amount of excitement for science to them as you have to me. And Thandi, I hope that I have just as much fun with my first students as we did doing research and preparing to give talks and posters.

Now to the people who have given me practical support, lended a hand when necessary, and shared their time and expertise to help me accomplish this research. To the support staff of the Chemistry Department, you have some of the most difficult jobs in the department and I appreciate you very much—especially Tim Free, Gary Wynn, Art Pratt, Sharon Marshall, and Bill Gurley. Thanks are also due to present and past Larese group members; you have made this experience unforgettable. Thank you Allyn and Paige for all the work that you have done in helping me with the AAO project. Andi, thanks for all your help. Lillian, Sami, Rick, and Pete, your help has been indispensable; thank you for every time you stopped what you were doing to monkey around with my isotherm station, field a late night phone call, answer a question, or just goof off. Thank you very much.

I must thank all the funding agencies that have made this work possible. Support was obtained from the Department of Energy Division of Materials Science, Office of Science, Basic Energy Sciences under contract DE-AC05-00OR22725. Financial support was also obtained from the National Science Foundation under contract DMR-0412231. In addition, Dr. Larese's start up funds from the University of Tennessee were used to maintain this project. Some travel support was also provided by the UT Chemical Physics Program.

Thanks must be given to Dr. David Joy who gave me extensive instruction and help in using the scanning electron microscope. Without his expertise, I would never have gained the skills needed to image my samples.

I would like to thank my committee members, Dr. T. Ffrancon Williams, Dr. George Kabalka, and Dr. Norman Mannella.

A special thanks goes to my research advisor and committee chairperson, Dr. John Larese, for taking a chance on a young student with as many faults as I have. You saw more potential in me than any other teacher/advisor that I have ever had and I thank you for showing it to me.

As customary, the most important person is saved for last—my beautiful and loving wife, Jenee. We have known each other for almost nine years, and each year is

better than the last. Your never-ending love and support is what helps me have the strength to face each day. Words cannot express how much I appreciate everything you have done for me. Thank you and I love you with all my heart.

Abstract

This work is divided into two parts: the adsorption of propane on the magnesium oxide (100) surface and the synthesis of anodized aluminum oxide. The adsorption properties of propane on the MgO (100) surface were investigated using high-resolution volumetric isotherm techniques and a computational study was accomplished using Materials Studio. From the adsorption work, the two-dimensional isothermal compressibility, the isosteric heat of adsorption, the differential enthalpy, and the differential entropy of adsorption can be calculated. Three distinct layers of propane were observed to form on the MgO (100) surface and it was determined that a phase transition occurs at 162 K. The simulation study showed that the propane molecule adsorbs on the surface, centered over magnesium, at a distance of 3.18 Angstroms. The molecule is oriented such that the carbon backbone is parallel to the surface and is rotated so that three hydrogen atoms are close to the surface. The calculated minimum energy of this system is 13.70 kcal/mol.

The second part of this study focuses on the synthesis and characterization of well defined, close packed, high aspect ratio cylindrical channels in an aluminum oxide matrix. These materials have been systematically produced using a two-step anodization process that provides the ability to tune the pore diameter (<10 nm to 100 nm) while retaining the long-range hexagonal pattern. The effect of varying the type and concentration of the electrolyte was investigated. The synthesized materials were

characterized using a scanning electron microscope, an atomic force microscope, and a high-resolution volumetric isotherm station to obtain adsorption and desorption measurements. It was found that these three techniques compliment each other nicely. The SEM results give a quick overview of the topography of the surface, AFM gives a more complete profile of the surface, and the isotherm measurements provide an overall pore distribution. These materials have the potential to be used in the study of gas storage, quantum confinement, and nanowire growth.

Table of Contents

Chapter 1 Surface Science 1

Chapter 2 Propane on Magnesium Oxide 6

2.1 A Brief History of Adsorption 6

2.2 Background…….. 17

2.2.1 Types of Adsorption 17

2.2.2 Surface Structure 19

2.2.3 Adsorption Phenomena and Related Thermodynamics 24

2.3 Experimental Setup 34

2.3.1 Magnesium Oxide Synthesis and Preparation 34

2.3.2 Gas Handling System 36

2.4 Thermodynamic Results 37

2.4.1 Isotherm Data 37

2.4.2 Monolayer Capacity and Molecular Area 40

2.4.3 Two-Dimensional Isothermal Compressibility 44

2.4.4 Two-Dimensional Thermal Expansion 49

2.4.5 Thermodynamic Quantities 51

2.5 Structural Simulation Results 54

2.5.1 Forcite Module 56

2.5.2 Setting up a Forcite Calculation 58

2.5.3 Geometry Optimization of Propane on MgO 58
2.5.4 Potential Energy Surface 67
2.6 Conclusion 77
Chapter 3 Anodizing Aluminum Oxide 79
3.1 History 79
3.2 Background 81
3.3 Experimental Set-up 95
3.3.1 Synthesis of Anodized Aluminum Oxide 96
3.3.2 Characterization 99
3.4 Results 102
3.4.1 Microscopy Results 102
3.4.2 Types of Acid 109
3.4.3 Concentration of Acid 120
3.4.4 Adsorption/Desorption 122
3.5 Concluding Remarks 124
References 128
Vita 139

List of Figures

Figure 2-1 A Freundlich Equation fit for the distribution of Acetic Acid between water and Blood Charcoal. 9

Figure 2-2 An example Langmuir isotherm with $\alpha = 1$. 11

Figure 2-3 Representative BET isotherms with various c values. 13

Figure 2-4 The Five Types of BET Isotherms. 15

Figure 2-5 Common Miller Indices for a simple cubic lattice. 20

Figure 2-6 An SEM image of MgO nanocubes showing the exposed (100) surface. 21

Figure 2-7 The three types of adsorption sites on the MgO (100) surface. 23

Figure 2-8 Various views of a propane molecule. 25

Figure 2-9 A representation of an adsorption isotherm, along with layer growth. 28

Figure 2-10 A representative set of propane on MgO isotherms. 39

Figure 2-11 Adsorption Isotherm and 1st Derivative of Propane on MgO at 137.67K. ... 41

Figure 2-12 Point B method to determine the molecular area of propane on MgO. 42

Figure 2-13 Molecular Area of Propane on MgO. 43

Figure 2-14 Isothermal Compressibility for Propane Adsorbed on MgO. 46

Figure 2-15 FWHM of the First Layer. 47

Figure 2-16 FWHM of the Second Layer. 48

Figure 2-17 Thermal Expansion of Propane on MgO at 143.5 K. 50

Figure 2-18 Clausius-Clapeyron Plot of Propane on MgO. 52

Figure 2-19 Isosteric Heat of propane adsorbed on MgO at 143.5 K. 55

Figure 2-20 The three initial orientations of propane on MgO. 60
Figure 2-21 Orientation of Propane on MgO with the initial starting position above the hollow site. 62
Figure 2-22 Orientation of Propane on MgO with the initial starting position above the bridge site. 63
Figure 2-23 Orientation of Propane on MgO with the initial starting position above the oxygen A-top site. 65
Figure 2-24 Orientation of Propane on MgO with the initial starting position above the magnesium A-top site. 66
Figure 2-25 Minimum energy configuration of propane on MgO (100). 68
Figure 2-26 Potential Energy of propane as a function of center of mass distance from the surface. 69
Figure 2-27 Energy as a function of displacement in the x-direction. 71
Figure 2-28 Energy as a function of displacement perpendicular to the carbon backbone. 72
Figure 2-29 Energy as a function of displacement parallel to the carbon backbone. 73
Figure 2-30 Rotation of propane about the z axis. 74
Figure 2-31 Rotation of Propane about the carbon backbone. 75
Figure 3-1 Path of the electron beam in an SEM column. 87
Figure 3-2 The four types of hysteresis loops. 93
Figure 3-3 Anode and cathode mounted in Lexan holder. 97
Figure 3-4 Summary of the synthetic steps to produce the anodized aluminum oxide. . 100

Figure 3-5 Steps involved in processing an SEM image. 104
Figure 3-6 SEM images of a sample of anodized aluminum oxide. 106
Figure 3-7 Pore distributions for the images in Figure 3-6. 107
Figure 3-8 AFM image of a sample of anodized aluminum oxide. 108
Figure 3-9 Depth analysis of an AFM image. 110
Figure 3-10 Cross sectional analysis of AAO. 111
Figure 3-11 The structure of the various acids used in the synthesis. 113
Figure 3-12 Anodized aluminum oxide synthesized in sulfuric acid. 115
Figure 3-13 Anodized aluminum oxide synthesized in oxalic acid. 116
Figure 3-14 Anodized aluminum oxide synthesized in malonic acid. 117
Figure 3-15 Anodized aluminum oxide synthesized in succinic acid. 118
Figure 3-16 Summary of all four acid types used in the synthesis. 119
Figure 3-17 The effect of concentration on the pore diameter. 121
Figure 3-18 Adsorption/Desorption Isotherm of anodized aluminum oxide. 123
Figure 3-19 Pore Size Distribution of the anodized aluminum oxide. 125

Chapter 1 **Surface Science**

Surface science is defined as the study of how matter interacts with a liquid or solid surface. Problems currently being investigated in all areas of natural science—including biology, chemistry, engineering, environmental science, medicine, and physics—have the potential to be solved using the techniques of surface science. For instance, atomic force microscopy can be used to investigate the mechanics and thermodynamics of a single DNA molecule (Hansma 2001). Other issues being tackled with surface science techniques include the study of artificial fertilizers, fuel cells, the depletion of the ozone layer, catalytic converters, corrosion, and semiconductors (Dabrowski 2001).

The Nobel committee recognized the importance of surface chemistry when they awarded the 2007 Chemistry prize to Gerhard Ertl "for his studies of chemical processes on solid surfaces." Ertl has spent his scientific career applying various experimental techniques to the study of surface science. He is best known for his work dealing with the Haber-Bosch process and the oxidation of carbon monoxide on platinum. The Haber-

Bosch mechanism (partially named after Fritz Haber who won the prize in 1918) explains how nitrogen and hydrogen will react over an iron substrate to produce ammonia. Another Nobel laureate, Irvin Langmuir (the first industrial scientist to win the prize), won the Chemistry prize in 1932 "for his discoveries and investigations in surface chemistry." He is most famous for his contributions in the areas of adsorption and single molecular layer thin films. Finally, Paul Sabatier must be included in this list. He was awarded the Nobel prize in 1912 for "his method of hydrogenating organic compounds in the presence of finely disintegrated metals whereby the progress of organic chemistry has been greatly advanced in recent years." This work laid the foundation for the most current Nobel laureate by helping advance the concept of a hydrogen molecule adsorbing onto a metal surface and dissociating into its constituent atoms (2008).

Other distinguished scientists throughout history have contributed to the field of surface science. In the area of thin films, Katharine Blodgett and Agnes Pockels played an important role in studying the science of monomolecular surface films on liquids. The mathematicians Marquis Pierre Simon Laplace and William Thomson (also known as Lord Kelvin) were pivotal in developing the theory of surface tension, as well as the renowned physicist and physician Thomas Young. While this is certainly not a comprehensive list, all of these scientists (chemists, physicists, mathematicians, and physicians) helped develop and make the field of surface science as diverse as it is today (Schramm 2004).

Nanotechnology is the next promising field where, building upon the foundation laid by the previously mentioned scientists, all current techniques of surface science are applied to the solution of new and interesting problems. The emergence of this new field has helped expand the number of practitioners of surface science. Historically, one of the major concerns of surface science has been the study of adsorption of thin films on a liquid or solid surface, with the pioneering scientist being Irvin Langmuir. Adsorbed molecules and atoms on metal and metal oxide surfaces are the main systems studied, including metal and metal oxide surfaces such as Pd (111), Si (111), Ni (100), and MgO (100) surfaces. While many surfaces have already been studied, we still do not have a complete understanding of how atoms and molecules interact with a multitude of interfaces. Nanotechnology is helping to develop better experimental techniques to investigate surface interactions, including state of the art spectrometers, attosecond lasers, high-resolution electron microscopes, and world-class computational centers.

From nanotechnology, surface science is branching into porous materials. A porous material is a compound that has pores or cavities that are interconnected throughout the material. Ubiquitous porous materials that we encounter in our everyday lives include filters, cement, foam, rocks, biological tissue (bones and skin), and ceramics. They have uses in a wide variety of industries, including medicine, energy, transportation, and technology. The porous media currently described in scientific and engineering literature at the forefront of nanotechnology include zeolites, mesoporous silica spheres, metal organic frameworks (MOFs), and anodized oxides such as

aluminum, titanium, and niobium. These materials have proven utility in filtration systems, drug delivery transport, hydrogen storage, and as templates for making various nanomaterials.

It is the hope of the author that this study will aid in the understanding of two specific areas in surface science: the adsorption of a thin film of propane on the magnesium oxide (100) surface, and a systematic study of the synthesis of porous aluminum oxide templates. The adsorption work is a small part of a larger study being conducted by the Larese group at the University of Tennessee. The group is able to make molar quantities of nearly defect free magnesium oxide (100) surface. Magnesium oxide is an ideal substrate for investigating thin films of alkanes; its simple cubic structure make it one of the simplest metal oxides and ensures that only the (100) surface is exposed.

A two-step anodization process is used to synthesize the porous aluminum oxide templates. This technique is ideal for making templates with tunable pore diameters. With these templates, the Larese group will be able to investigate adsorption phenomena of porous material, including the effects of confinement.

The remainder of this thesis is organized into two additional chapters. An overview of each chapter is given here.

- Chapter 2 deals with the study of propane on magnesium oxide. A history and background of adsorption is given. The experimental setup is described, and thermodynamic results of the study are tabulated. In addition, the results of a computer simulation of the adsorption of propane on the MgO (100) surface are discussed.

- Chapter 3 focuses on the anodization of aluminum oxide, gives a background of the anodization process, and describes a theory of the nature of pore growth in the aluminum oxide film. A discussion of Scanning Electron Microscopy (SEM) and Atomic Force Microscopy (AFM) is also given, along with a description of the experimental setup used to make aluminum oxide films. Finally, results of films grown in sulfuric acid and various dioic acids are discussed.

Chapter 2 **Propane on Magnesium Oxide**

As mentioned in the first chapter, the study of propane on magnesium oxide is a small part in a larger study of alkanes on the (100) surface of magnesium oxide. Previous studies by the Larese group include the adsorption of methane (Freitag and Larese 2000) and ethane (Arnold, Cook et al. 2005) on this surface, along with the homologous series of butane through octane (Arnold, Chanaa et al. 2006; Arnold, Cook et al. 2006; Yaron, Telling et al. 2006). This chapter begins with a brief history, followed by a more mathematical description of adsorption phenomena. Next, the substrate and adsorbate are discussed, and a description of the experimental setup is given. Finally, thermodynamic results, structural simulation results, and conclusions are given.

2.1 A Brief History of Adsorption

The term adsorption originated in the late 19th century and is a combination of the prefix ad- and the word absorb. Adsorption is the process by which a substrate material holds molecules of a gas, liquid, or solute as a thin film on external or internal surfaces of

the substrate. Du Bois-Reymond first proposed the term, but Kayser was the first to use it in literature in 1881 (Herzberg 1955). It might be surprising that the applications of adsorption using carbon have been around for almost 6000 years. Around 3750 BC, the Egyptians and Sumerians used charcoal to reduce copper, zinc, and tin in order to manufacture bronze. In 1550 BC, the Egyptians developed a few medical applications using charcoal; they found that charcoal could adsorb odorous vapors from the intestines and decaying wounds. Around 450 BC, Hippocrates and Pliny used charcoal to treat epilepsy, chlorosis, and anthrax, and the Phoenicians first used charcoal filters for purifying drinking water in their trading vessels (Dabrowski 2001).

Although adsorption was studied qualitatively in ancient times, Scheele and Fontana are credited with making the first quantitative measurements in the late 1700s (Dabrowski 2001). One of the more popular American scientists, Benjamin Franklin, also dabbled in the study of adsorption. He observed what many sea captains already knew; that a thin layer of oil could "calm the waters" (Lane 2003). In the early 1900s, scientists began to develop empirical equations to describe adsorption phenomena. The Freundlich equation,

$$\frac{x}{m} = Kp^{\frac{1}{n}}, \qquad 2.1.1$$

was the first empirical equation used to explain adsorption isotherms. In Equation 2.1.1, the variables are defined as follows: x is the mass of adsorbate, m is the mass of adsorbent, p is the equilibrium pressure of the adsorbate, and K and n are constants that

depend on the adsorbate and adsorbent at a particular temperature. Figure 2-1 shows adsorption data between acetic acid and blood charcoal (Bancroft 1921). The fitted line is determined using Equation 2.1.1, where the parameter K and n were determined to be 2.56 L/mol and 2.57, respectively. The Freundlich equation, along with the Langmuir, BET, and FHH equations are discussed in the following paragraphs. The derivations of these theories can be found in numerous review articles and books (Brunauer, Emmett et al. 1938; Brunauer 1943; Flood 1967; Aveyard and Haydon 1973; Adamson and Gast 1997; Dabrowski 2001). Although Freundlich was not the first to mathematically describe an isotherm (van Bemmelen first proposed an equation in 1888 and Boedecker used it in 1895), he is given credit for making it a standard and by showing its importance (Dabrowski 2001).

Soon after the Freundlich equation became popular, Langmuir and Polanyi, who extended the work of Eucken, proposed two independent descriptions of adsorption phenomena. The Eucken-Polanyi potential theory was based on the idea that the solid (adsorbent) and the already adsorbed molecules exerted attractive forces on the gas above the surface. Using his theory, Polanyi was able to describe the way the adsorption isotherm varied with temperature (Holmes and Levere 2000). Irving Langmuir at the General Electric Laboratory in Schenectady, New York, studied the adsorption of gases on mica surfaces and on water. From these studies, a general treatment of reaction kinetics on surfaces was formulated. By making the assumptions that there are a finite number of energetically equivalent adsorption sites and the bonding of the adsorbed

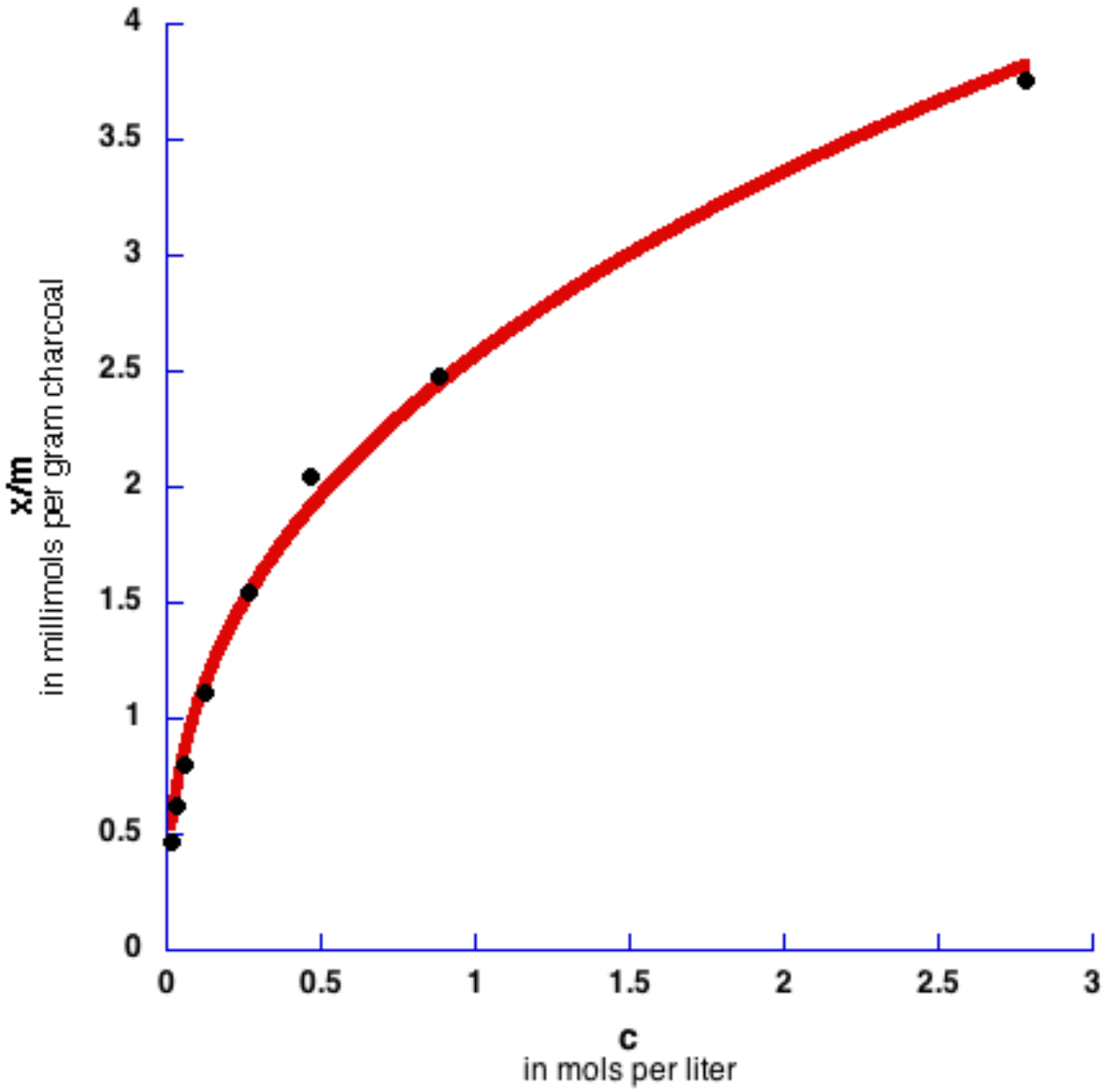


Figure 2-1 A Freundlich Equation fit for the distribution of Acetic Acid between water and Blood Charcoal.

molecules are strong enough to prevent movement along the surface, and ignoring lateral interactions between the adsorbed molecules, he was able to introduce for the first time the concept of monomolecular adsorption. He then proceeded to derive an equation that, unlike the Freundlich equation, had a theoretical foundation (Langmuir 1918; Weiser 1946; Holmes and Levere 2000; Dabrowski 2001).

The Langmuir equation,

$$\theta = \frac{\alpha \mathrm{P}}{1 + \alpha \mathrm{P}}, \qquad 2.1.2$$

where θ is the percentage of surface coverage, α is a constant relating the rate of condensation to the rate of evaporation, and P is the gas pressure, has attained a prominent status in surface science. While the Langmuir equation gives a better representation of the physical adsorption of gases on a variety of adsorbents than the Freundlich equation, it does have a couple of drawbacks. First, it predicts a monolayer saturation value that is independent of temperature. Second, it assumes that the adsorbed film is only a single molecular layer thick. Even with these drawbacks, the Langmuir equation inspired others to carry out more comprehensive theoretical investigations to describe experimental adsorption systems (Dabrowski 2001). Figure 2-2 shows an example Langmuir isotherm, where α =1. From this figure, we can see that at low pressures, the isotherm shows a linear increase in coverage with pressure (i.e. the Henry's Law region), while at higher pressures, the isotherm plateaus representing monolayer saturation.

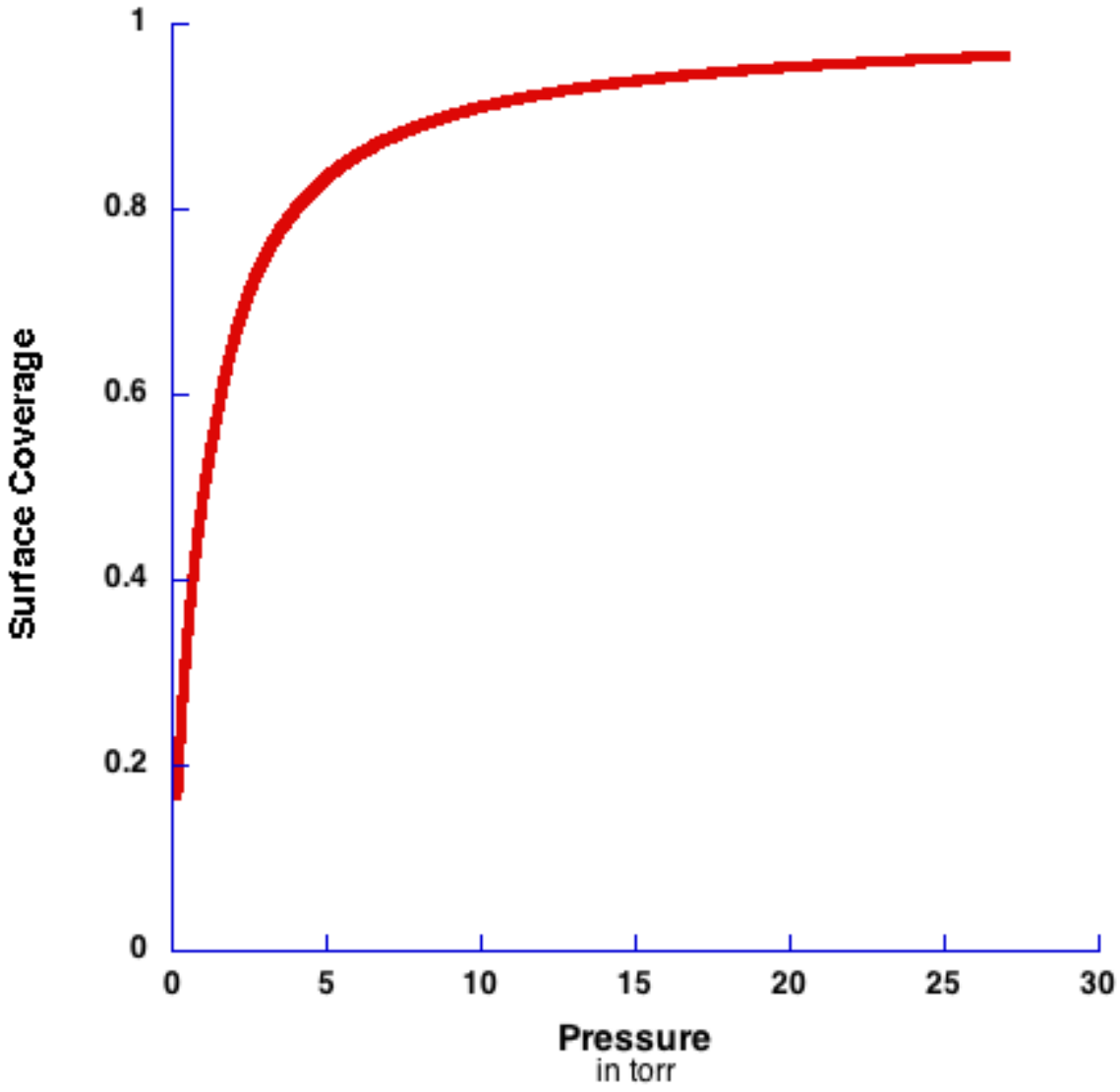


Figure 2-2 An example Langmuir isotherm with $\alpha = 1$.

In the mid to late 1930's, Stephan Brunauer, Paul Emmett, and Edward Teller developed an isotherm equation that incorporates multilayer adsorption (Brunauer, Emmett et al. 1938). Brunauer and Emmett were also the first to propose the point B method of determining the amount adsorbed in a monolayer. More details of the point B method are discussed later in the chapter. The Brunauer, Emmett, and Teller (BET) isotherm equation is

$$\frac{v}{v_m} = \frac{c\frac{P}{P^o}}{\left(1 - \frac{P}{P^o}\right)\left[1 + (c - 1)\frac{P}{P^o}\right]}. \qquad 2.1.3$$

The variables in Equation 2.1.3 are as follows: v is the volume of adsorbed gas, v_m is the volume of a monolayer of adsorbed gas, P and P^o are the equilibrium and saturated vapor pressures, respectively, and c is termed the BET constant and is dependent on the heats of adsorption for each layer. The standard method for determining surface area is to apply the BET equation to the analysis of a nitrogen isotherm, acquired at 77K. Unfortunately, the BET equation fails at low and high pressures, where it predicts too little and too much adsorption, respectively.

Figure 2-3 shows examples of BET isotherms obtained by varying the constant c. As can be seen in the figure, the BET isotherm resembles the Langmuir isotherm at large values of c (>500), where the heat of adsorption for the monolayer is much greater than for subsequent layers. At modest values of c (~100), a typical BET isotherm results.

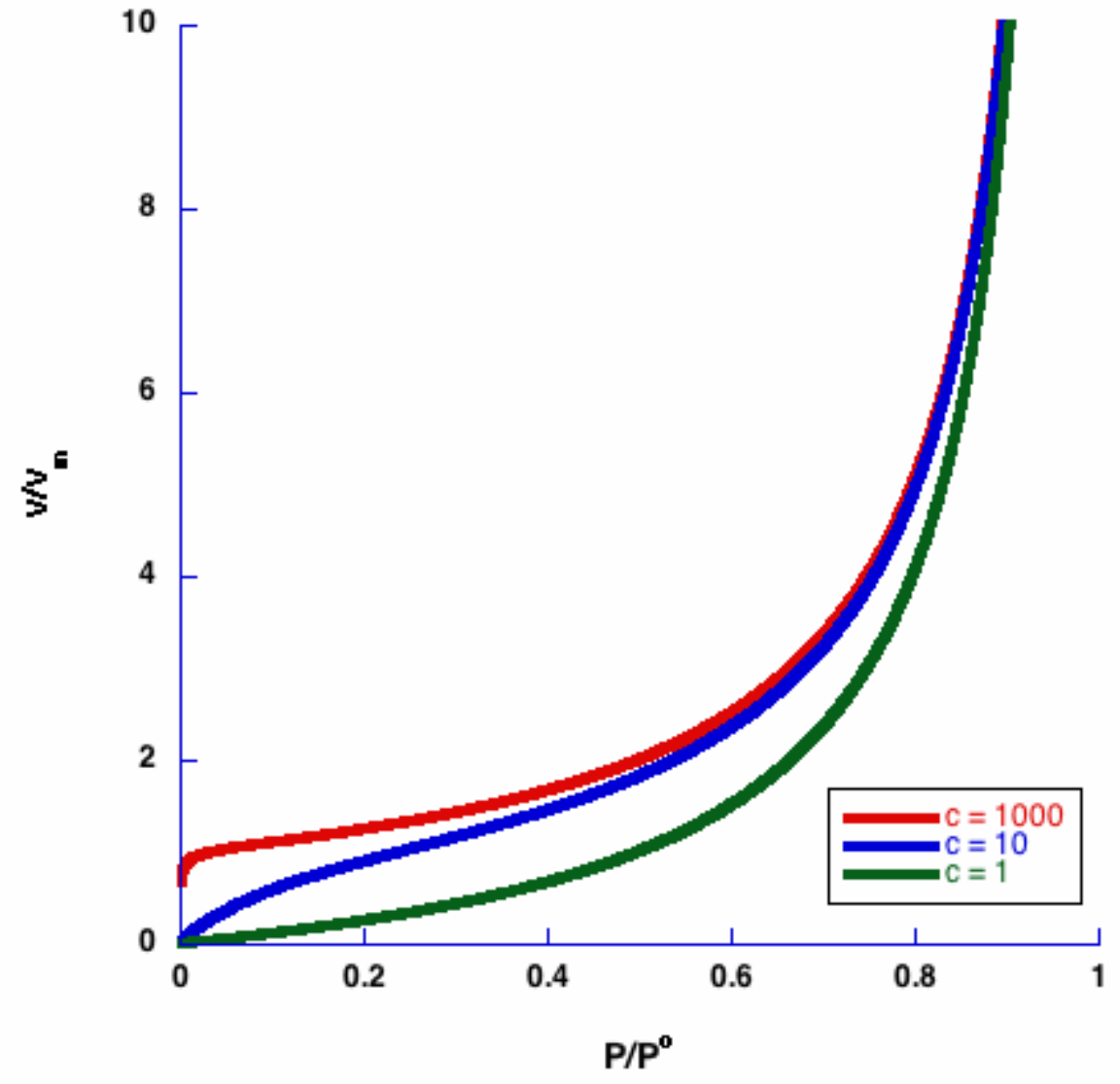


Figure 2-3 Representative BET isotherms with various c values.

However, at low values of c, the isotherm shape reflects weak interactions between the adsorbate and adsorbent. These isotherms represent three of the five types that Brunauer described in his book, "The Adsorption of Gases and Vapors." All five types can be seen in Figure 2-4 (Brunauer 1943). As previously mentioned, the Type I isotherm has a large c value and corresponds to the Langmuir isotherm (adsorbent is assumed to have a homogenous surface where all adsorption sites are energetically identical, only monolayer adsorption exists, and there are no interactions between the adsorbed molecules). The Type II isotherm is the typical BET isotherm. It shows multilayer adsorption beyond the monolayer and is the most common isotherm for non-porous materials. Type III isotherms are typical for materials with little or no attraction to the adsorbing species (e.g., water on a hydrophobic surface). The last two isotherms, Types IV and V, are representative of porous materials. The Type IV isotherm is similar to Type II, and Type V is similar to Type III. In both cases, the corresponding isotherms have very similar shapes at low relative pressure, but Types IV and V exhibit hysteresis at high relative pressure. Porous materials and pore condensation are discussed in more detail in Chapter 3 (Brunauer 1943; Adamson and Gast 1997).

The BET theory is able to describe the major portions of the adsorption isotherm. BET predicts the areas of monomolecular adsorption (similar to Langmuir's theory), polymolecular adsorption, and to a certain extent capillary condensation. Of course, capillary condensation is one of two places where the BET theory fails. The main

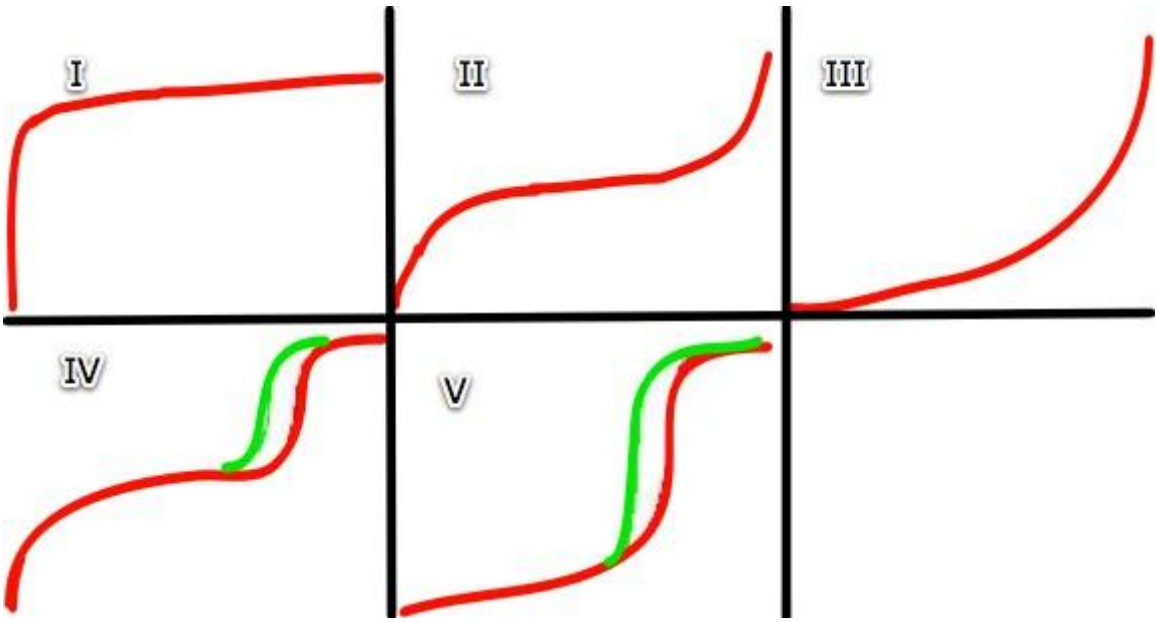


Figure 2-4 The Five Types of BET Isotherms.

assumption in the BET formalism is that the adsorbent presents an interface that has a geometrical and homogeneous surface at which mono- or multi-layer adsorption takes place, and thus has a measurable surface area. However, if the adsorbent is a heterogeneous material that is also porous with various capillary widths, the high-pressure portion of the isotherm is not well described. Another drawback to the BET theory is that it cannot be applied to adsorption at temperatures higher than the critical temperature of the adsorbate, because it is not possible to assume equality of heats of adsorption and condensation. Nevertheless, the BET method has been the standard procedure for determining the specific surface area of fine powders and porous materials for over half a century. The BET theory is the basis for many current adsorption models, described in detail in various review articles and textbooks (Adamson and Gast 1997; Dabrowski 2001).

To describe the high pressure portion of the adsorption isotherm, Frenkel, Halsey, and Hill (FHH) independently proposed a slab approximation. They assumed that the adsorbed films take on the characteristics of a slab of liquid when close to the saturated vapor pressure (SVP), and that this phenomenon would be best described by incorporating a van der Waals correction. Their proposed expression is referred to as the FHH equation, and has the form

$$\frac{P}{P^0} = e^{\frac{-U}{\theta^s}}, \qquad 2.1.4$$

where U takes into account the van der Waals interaction, θ is the surface coverage, and s is an empirical parameter. As with earlier adsorption models, the FHH expression also has a major shortcoming. While FHH predicts high coverage behavior accurately, the low coverage limit is poorly represented (Lowell, Shields et al. 2004).

2.2 Background

In the following sections, we discuss various topics from solid-state physics as they pertain to adsorption phenomena. A brief description of the two types of adsorption (chemisorption and physisorption) is included in this section. A short section on surface structure follows, including such topics as Miller indices, surface defects, and various adsorption sites of magnesium oxide. Finally, a concise discussion on the thermodynamics of adsorption is presented.

2.2.1 Types of Adsorption

Outside of a vacuum, all surfaces are exposed to the gases of the surrounding environment. These gases may adsorb or condense onto the surface. Depending on the environmental parameters (temperature and pressure), and the nature of the gas and exposed material, this adsorption could take the form of chemisorption or physisorption.

The stronger of the two types of interactions is chemisorption. As the name implies, it is of a chemical nature—meaning electron transfer occurs between the

substrate and adsorbate. This electron transfer has the potential of inducing a surface rearrangement or even the formation of a new compound (e.g. iron oxide "rust"). When chemisorption occurs, the adsorbate may be removed from the surface by heating to extremely high temperatures in cases where thermal decomposition is possible. Generally, the term chemisorption can be applied when the adsorption energy is comparable to chemical bond energies in the system (Adamson and Gast 1997). Experimentally, chemical adsorption increases with temperature until reaching a maximum, then gradually decreases as the temperature increases. When starting at low pressures, chemisorption increases with increasing pressure, but a saturation point is reached at which increasing the pressure does not change the amount adsorbed (i.e. a chemical transformation occurs).

Physical adsorption, or physisorption, occurs when the adsorption energy is much lower than the chemical bond energy. Generally, all gases below their critical temperature will physisorb onto a surface as a result of the van der Waals or weak intermolecular interactions between the adsorbate and the adsorbent. Unlike chemisorption, physical adsorption is a reversible process (via desorption). Typically, physisorption decreases rapidly and continuously with increasing temperature. Multiple layers may form by physisorption due to the relatively long range of interactions, unlike the chemisorption case, where generally only a monolayer is formed. As the pressure is increased, more and more molecules physisorb onto the surface, until the saturated vapor

pressure is obtained, at which point a bulk-like structure will form. The system discussed in this chapter, propane on magnesium oxide, is an example of physisorption.

2.2.2 Surface Structure

A crystal is constructed of an infinite array of atoms, molecules, or ions that have a regular, geometrically repeating pattern. The structure of a crystal is best represented by a basis, a set of vectors that define unit dimensions within the crystal lattice. All points in the lattice can be described by a linear combination of the basis vectors. In determining the structure of a crystal, the orientation of the various crystal planes is designated by Miller indices. These indices are a set of numbers that are related to the positions of the atoms in the lattice (Kittel 1996; Kolasinski 2002). Figure 2-5 describes the most common Miller indices for the simple cubic lattice. The metal oxide studied in this dissertation, magnesium oxide (MgO), has the predominate (100) surface exposed for adsorption. A Scanning Electron Microscopy (SEM) image of the synthesized cubic MgO particles with the exposed (100) surface is shown in Figure 2-6.

Our synthetic procedure for MgO produces substrate with very few surface defects (details of the synthesis will be provided in Section 2.3). However, it would be remiss not to elaborate on some common defects of MgO. The most readily identifiable would be the low coordinated Mg^{+2} and O^{-2} ions, located on the edges or corners of the

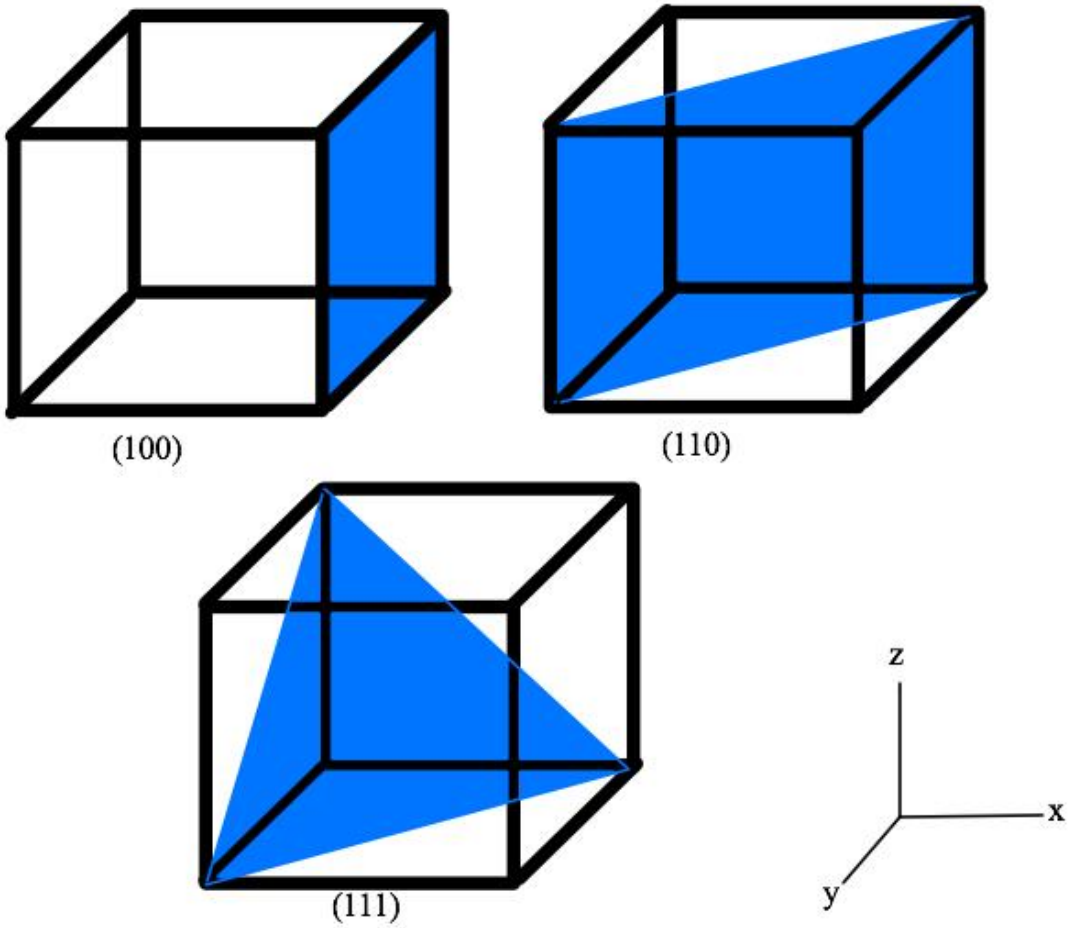


Figure 2-5 Common Miller Indices for a simple cubic lattice.

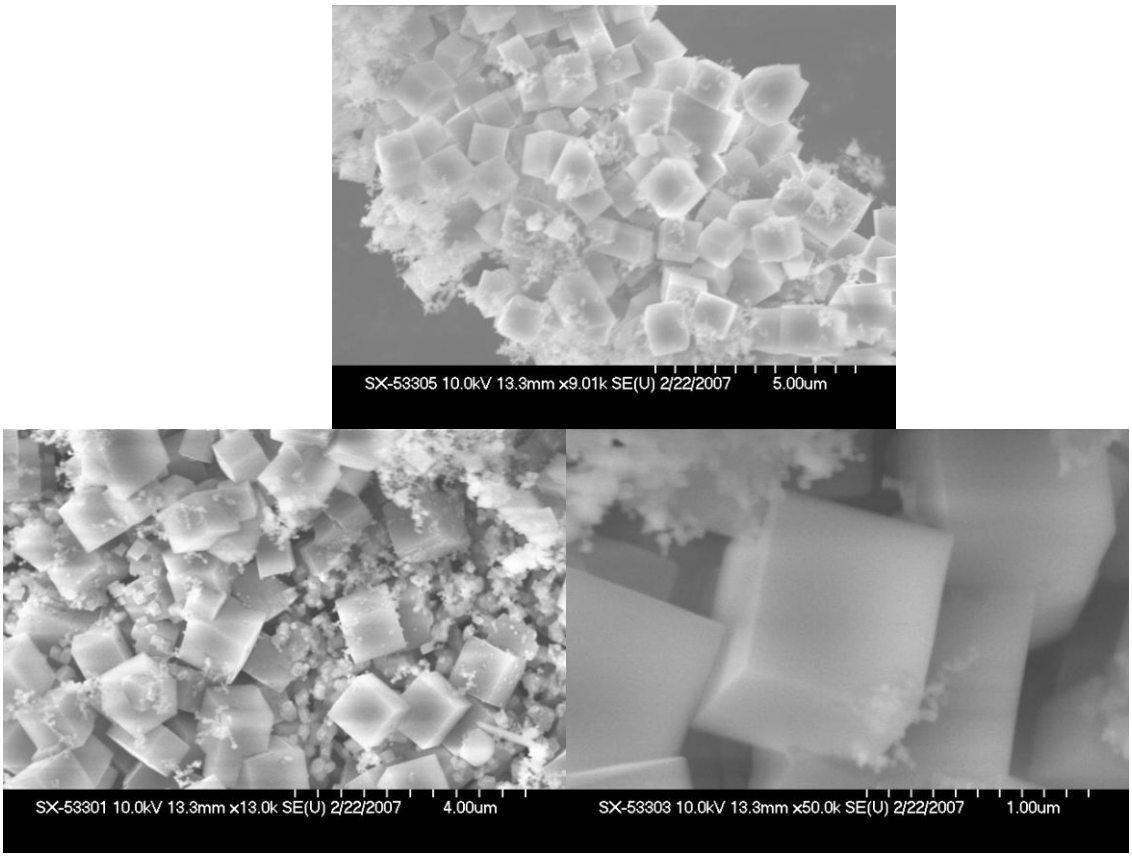


Figure 2-6 An SEM image of MgO nanocubes showing the exposed (100) surface.

MgO cube. Another common defect is the presence of surface hydroxyl groups, which can result from exposing the MgO to water or a high humidity environment (Cox and Hendrich 1994). It is also possible for MgO to have cation or anion vacancies, and transition metal impurities present (Pacchioni 2001). A majority, if not all, of these imperfections were minimized by the methods we employed in the substrate synthesis and preparation for adsorption measurements. More details are presented later in this chapter.

Before proceeding to a discussion on the thermodynamics of adsorption, we describe the possible adsorption sites. The potential energy of interaction between a molecule and a surface varies with the molecule's position relative to the surface. Due to thermal motion, molecules will vibrate and translate around the minimum of the potential well. The average position of a molecule during these vibrational and translational excursions is called the adsorption site (Aveyard and Haydon 1973). Figure 2-7 shows four possible high-symmetry adsorption sites on the MgO surface. First, the "A top" sites are located directly above the magnesium or oxygen ions. Second, the sites between the magnesium and oxygen ions are called the "bridge sites." And finally, the "hollow sites" are located in the center of the unit square formed by the ions. These are all highly probable locations for molecular adsorption; i.e. where the minimum potential energy will occur for an adsorbed molecule on the MgO surface.

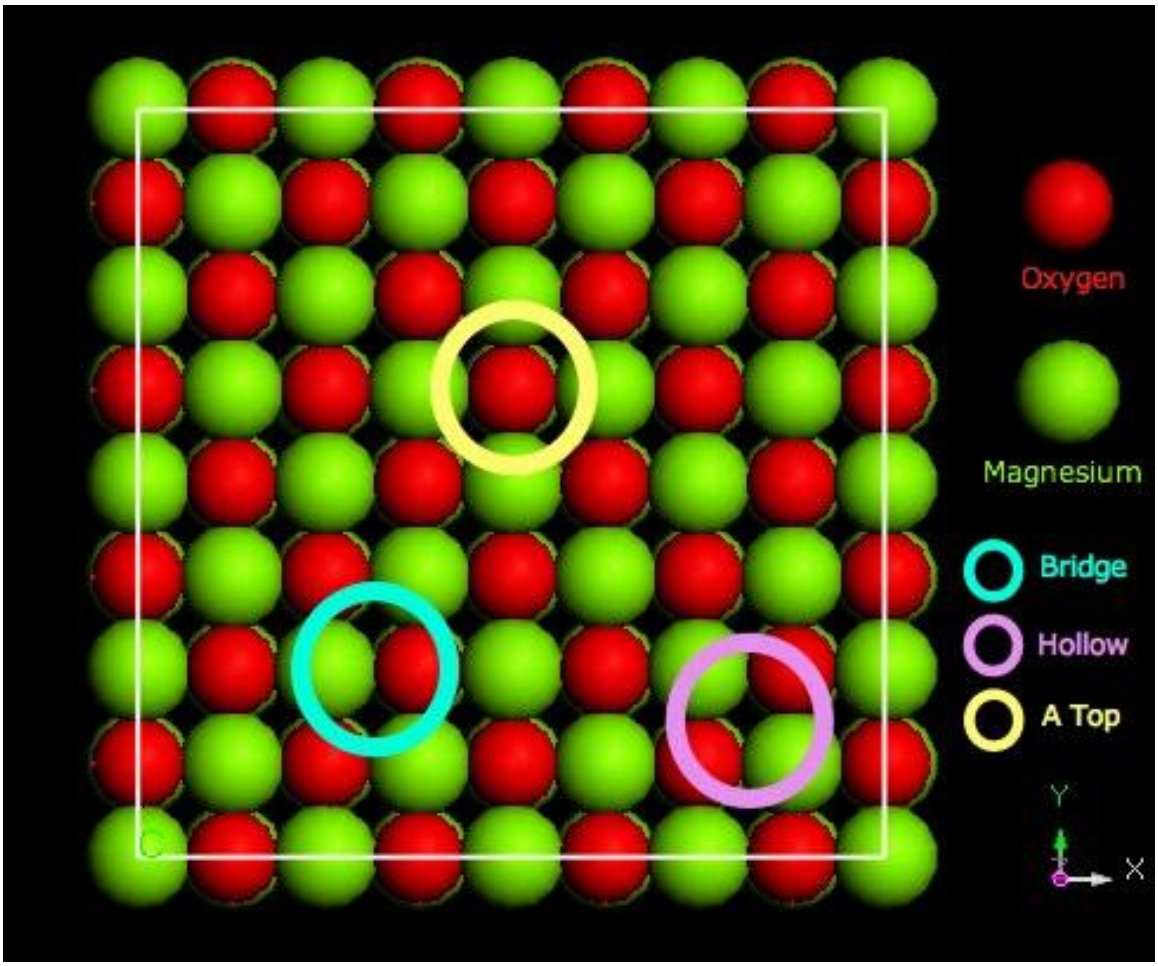


Figure 2-7 The three types of adsorption sites on the MgO (100) surface.

2.2.3 Adsorption Phenomena and Related Thermodynamics

Differential adsorption is a technique that has numerous applications in the field of separation chemistry. One widespread application involves separating the components in natural gas and other industrial gas streams. Several industrial processes for recovering propane from natural gas employ adsorption on a carbon molecular sieve (Grande, Silva et al. 2003). Other adsorbents have been investigated, both experimentally and computationally; these include numerous forms of graphite (Kiselev 1961; Ross, Saelens et al. 1962; Myers and Prausnitz 1965; Taylor and Atkins 1966; Hoory and Prausnitz 1967; Di Corcia and Samperi 1973; Lal and Spencer 1974), carbon molecular sieves (Nakahara, Hirata et al. 1974), zeolites (Mayorga and Peterson 1972), γ-alumina (Baumgarten, Weinstrauch et al. 1977), and a variety of metal surfaces (Hopkins and Shah 1972; Dawson 1977; Wittrig, Szuromi et al. 1982; Szuromi, Engstrom et al. 1985; Hamza, Steinruck et al. 1987; Sault and Goodman 1988; Beaglehole 1992).

Propane, the molecule of interest in this study, is a three carbon, nonpolar alkane (C_3H_8) shown in Figure 2-8. It is a byproduct of natural gas processing and petroleum refining. Propane is used as a household and industrial fuel for cooking and heating, and as an alternative fuel in motor vehicles. It is a main component of liquefied petroleum gas (LPG), an attractive fuel that, when burned, gives off a minimum amount of air pollution, has little solid residue, and does not dilute the lubricants commonly used in

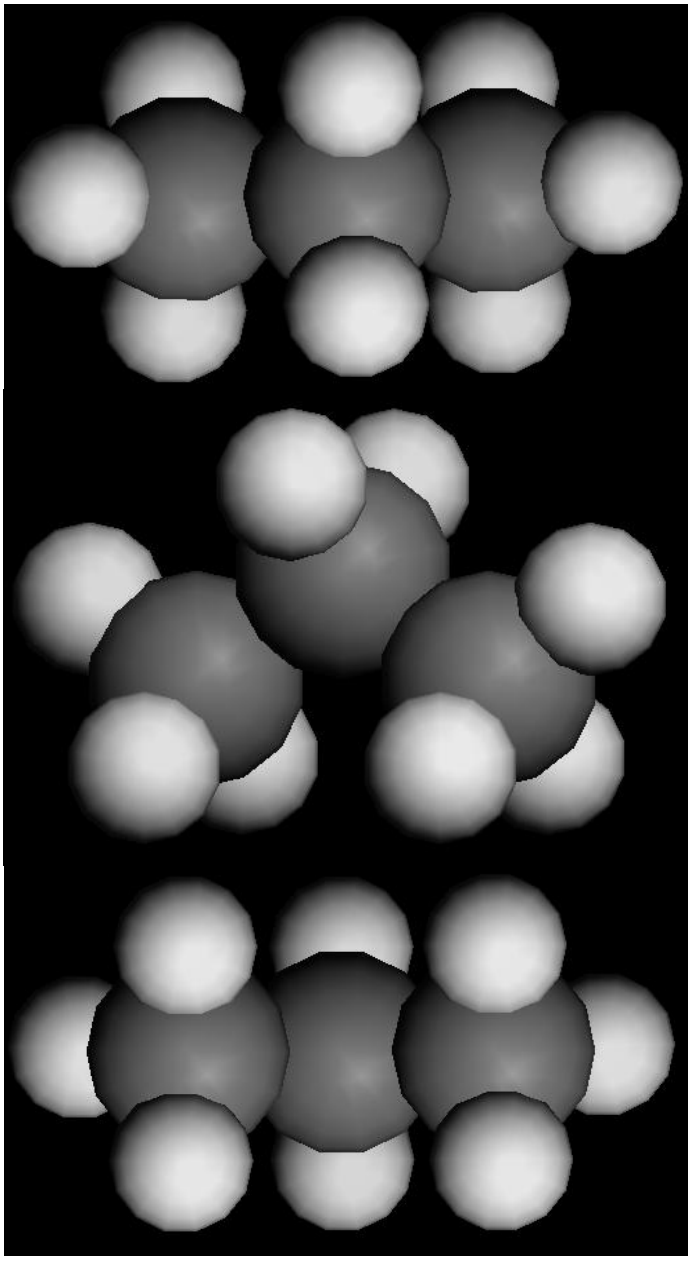


Figure 2-8 Various views of a propane molecule.

machinery. Propane is an important raw material in the manufacture of ethylene (C_2H_4) and in the petrochemical industry. Another popular use for propane is in gas absorption refrigerators, which have no moving parts, do not require electricity, and are highly efficient and long lasting. Propane also has been widely used as a propellant for aerosol sprays.

The remainder of this section presents background information relevant to the thermodynamic characterization of multilayer adsorption properties of propane on the (100) surface of magnesium oxide (MgO) by volumetric adsorption isotherms. As mentioned before, this study is one component in the systematic investigation of the behavior of short-chained alkanes and alkenes on MgO, with the ultimately goal of developing a comprehensive theoretical description of how these molecules interact with the MgO (100) surface (Freitag and Larese 2000; Arnold, Cook et al. 2005). Questions remain on how the surface corrugation, symmetry, and imperfections (vacancies and defects) affect the physical properties of the adsorbed molecular layer. Furthermore, even less is known about the role metal oxide surfaces play in mediating simple chemical reactions.

The adsorption isotherm is an ideal experimental technique to study how molecules interact with a surface. From the isotherm, the number of adsorbed molecules and surface area of the substrate can be determined. The two dimensional compressibility can also be calculated from the isotherm data, and may then be used to

determine if phase transitions occur during the adsorption process. The differential enthalpy and entropy, along with the heats of adsorption can be determined with the Clausius-Clapeyron equation.

Figure 2-9 shows a representative adsorption isotherm, along with an illustration of how molecules form layers on a surface. The ordinate is a measure of the number of adsorbed molecules on the surface, and, for this investigation, has the units of millimoles of adsorbate. Another unit commonly used for the ordinate is volume adsorbed, meaning the STP volume of adsorbate that is on the surface of the substrate. The abscissa is a measure of the vapor pressure of adsorbate at the temperature of the isotherm. Many times the abscissa represents the relative pressure with respect to the saturated vapor pressure (SVP), or it could alternatively represent the chemical potential of the adsorbate. Region A of the isotherm curve represents what happens at the start of the adsorption process. The introduction of gas to the system often results in all the molecules initially sticking to the surface, if at a sufficiently low temperature. Consequently, in region A, the pressure does not increase and a vertical rise is seen on the adsorption isotherm. Next, in region B, the isotherm begins to flatten out as a result of the formation of a monolayer. As will be observed in the sections that follow, a second layer could form as the pressure increases, illustrated in region C. A second layer forms only if the structure of the adsorbed film is different than its bulk structure. However, if the film takes on the character of the bulk phase, then an asymptotic (or even abrupt) approach to the saturated vapor pressure is observed, shown in region D.

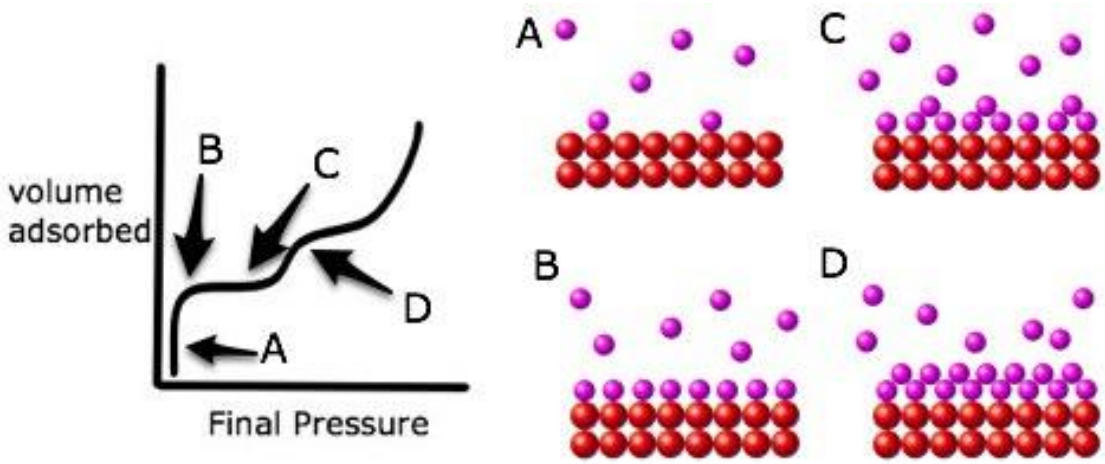


Figure 2-9 A representation of an adsorption isotherm, along with layer growth.

As mentioned previously, region B in Figure 2-9 is the point in the adsorption isotherm where a monolayer is completed. From this point, information about the surface area of the substrate or the area of the adsorbed molecule can be determined. Nitrogen gas is used in a "standard" isotherm to determine the surface area of a material; it is generally assumed that a single nitrogen molecule occupies 16.2 $Å^2$ on the surface (Adamson and Gast 1997). Since the molecular area of the nitrogen is assumed to be known and the number of molecules to complete a monolayer (point B) may be found by volumetric methods, the surface area of the substrate can be determined. The converse can also be assumed to be true—if the surface area of the substrate is known, then the area per molecule can be determined from a knowledge of the number of molecules in a monolayer. In the case of propane on MgO, the surface area of an MgO sample is determined using a methane isotherm. It has been experimentally determined by neutron diffraction that the area of a methane molecule on the MgO surface is 17.74 $Å^2$ (Larese 1998). Once the total surface area of the MgO powder is determined, the area of a propane molecule on the surface can be calculated from point B on the isotherm. Correspondingly, this method of analysis is termed the "Point B" method.

Because this dissertation involves the investigation of surface films, two-dimensional analogues of bulk thermodynamic expressions need to be employed. In many cases, it is sufficient to substitute a two-dimensional component for the three dimensional variable. One common bulk thermodynamic quantity that can be analogously derived for two dimensions is the two-dimensional isothermal

compressibility. The three-dimensional compressibility measures the volume change of a substance in response to a pressure. Hence, the three-dimensional compressibility is defined as

$$K_{3D} = -\frac{1}{V}\left(\frac{\delta V}{\delta P}\right)_T . \qquad 2.2.1$$

By substituting the pressure, P, with the spreading pressure of a film, ϕ, and the volume, V, with the molecular area of the film, σ, the two dimensional analogue to the isothermal compressibility becomes

$$K_{2D} = -\frac{1}{\sigma}\left(\frac{\delta \sigma}{\delta \phi}\right)_T . \qquad 2.2.2$$

The molecular area of the film is defined as

$$\sigma = \frac{A}{n}, \qquad 2.2.3$$

where n is the number of moles and A is the surface area of the substrate. The differential of Equation 2.2.3 equates to

$$\frac{\delta \sigma}{\delta n} = -\frac{A}{n^2} \qquad 2.2.4$$

By using the kinetic molecular theory of gases, we can define the chemical potential, μ, as

$$\mu = -k_B T \ln\left(\frac{k_B T}{\lambda^3 P}\right) \qquad 2.2.5$$

where k_B is the Boltzmann constant and λ is the de Broglie wavelength. Differentiating Equation 2.2.5, the following is obtained

$$\left(\frac{\delta\mu}{\delta P}\right)_T = \frac{k_B T}{P}. \qquad 2.2.6$$

Finally, by using the fundamental definition for the chemical potential,

$$d\mu = -SdT + \sigma d\phi, \qquad 2.2.7$$

and rearranging it to obtain

$$\left(\frac{\delta\phi}{\delta\mu}\right)_T = \frac{1}{\sigma}, \qquad 2.2.8$$

the two-dimensional isothermal compressibility becomes

$$K_{2D} = \frac{A \cdot P}{k_B T \cdot n^2 \cdot N_A}\left(\frac{dn}{dP}\right)_T \qquad 2.2.9$$

after substituting Equations 2.2.4, 2.2.6, and 2.2.8 into Equation 2.2.2. Avogadro's number, N_A, is included for dimensional agreement. By measuring the full width at half maximum (FWHM) of the two-dimensional isothermal compressibility as a function of temperature, Larher has argued that phase transitions in the adsorbed film can be observed (Larher 1992).

Similarly, the two-dimensional thermal expansion can be derived. The bulk definition of the thermal expansion is

$$\alpha_{3D} = \frac{1}{V}\left(\frac{\delta V}{\delta T}\right)_P. \qquad 2.2.10$$

Substituting the molecular area for volume and using Equations 2.2.3 and 2.2.4, the following is obtained

$$\alpha_{2D} = \frac{1}{\sigma}\left(\frac{\delta\sigma}{\delta T}\right)_P = \frac{1}{\sigma}\left(-\frac{A}{n^2}\right)\left(\frac{\delta n}{\delta T}\right)_P . \qquad 2.2.11$$

The partial derivative of Equation 2.2.5 with respect to temperature at constant pressure becomes

$$\left(\frac{\delta\mu}{\delta T}\right)_P = \frac{\mu}{T} - k . \qquad 2.2.12$$

By combining this equation with Equation 2.2.11 and the Gibbs definition for chemical potential,

$$\mu = kT \ln(P), \qquad 2.2.13$$

the final expression for the two-dimensional thermal expansion becomes

$$\alpha = -\frac{1}{n}\left(1 - \frac{1}{\ln\left(\frac{P}{P^0}\right)}\right)\left(\frac{\delta n}{\delta T}\right)_P . \qquad 2.2.14$$

In the final expression, pressure was converted to relative pressure to avoid the possibility of dividing by zero.

The differential enthalpy (ΔH) and entropy (ΔS) of the system are also easily calculated from the adsorption isotherms. When the system is in thermodynamic

equilibrium the Clausius – Clapeyron equation can be used to determine these quantities. The Clausius – Clapeyron equation is defined as

$$\ln\left(\frac{P}{P^0}\right) = -\frac{\Delta H}{RT}, \qquad 2.2.15$$

where P^0 is the saturated vapor pressure and R is the universal gas constant. From the observed isotherm data, plotting the natural log of final pressure versus inverse temperature for each completed layer will give a linear function,

$$\ln\left(P_f\right) = -\frac{A^n}{T} + B^n, \qquad 2.2.16$$

where n is the corresponding layer. The slope (A) of this line is proportional to the heat of adsorption, and the intercept (B) is proportional to the entropy of adsorption (Larher 1992; Freitag and Larese 2000). In each case, the proportionality constant is the universal gas constant. To obtain the differential heat and entropy, the difference from the bulk value is calculated as shown in the following equations:

$$\Delta H^n = -R\left(A^n - A^{bulk}\right) \qquad 2.2.17$$

$$\Delta S^n = -R\left(B^n - B^{bulk}\right). \qquad 2.2.18$$

In addition, the heat of adsorption (Q_{ads}) can be calculated from the slope using

$$Q_{ads} = R\, g\, A. \qquad 2.2.19$$

Finally, the isosteric heat of adsorption, Q_{st}, can be determined from a series of adsorption isotherms. This thermodynamic quantity represents the amount of energy that

is needed to remove an adsorbed molecule from the surface to the bulk vapor when the number of adsorbed molecules is held constant. At constant coverage, Q_{st} is defined as

$$Q_{st} = RT^2\left(\frac{\delta(\ln P)}{\delta T}\right)_{\theta}. \qquad 2.2.20$$

In practice, the partial derivative is approximated by taking the difference between two isotherms closely spaced in temperature; hence, the accuracy of the isosteric heat is dependent on the temperature difference between the two isotherms.

2.3 Experimental Setup

In this section, the experimental procedures used to perform the thermodynamic study of propane on MgO are discussed. A detailed discussion of the synthesis of MgO will begin the section. A description of the gas handling system and its components is also given.

2.3.1 Magnesium Oxide Synthesis and Preparation

The synthesis of MgO is fully detailed in the Kunnmann and Larese patent (Kunnmann and Larese 2001). Here, a brief description of the process is presented. Magnesium metal (*Alfa Aesar 99.9% purity*) is cut into small pieces and cleaned with dilute hydrochloric acid to remove any surface impurities. The principal impurity in the magnesium metal is manganese metal at the 4 ppm level. The cleaned magnesium is

mixed with high purity graphite and placed in a graphite crucible. The crucible is placed in an induction furnace, which is then purged with high purity argon. Once the atmosphere in the furnace is displaced multiple times, the magnesium metal is heated inductively until the magnesium vapor reacts with the graphite, forming highly reactive magnesium carbide. The magnesium carbide is thermally decomposed into carbon and magnesium vapors and subsequently reacted with oxygen, which is introduced into the growth chamber, resulting in the formation of highly pure, nanometer scale cubes of magnesium oxide.

This synthesis routine produces large quantities (~20 g) of MgO powder that have a relatively narrow size distribution (250 ± 30 nm) as determined by SEM and TEM (see Figure 2-6). The surface area of the particles is approximately 10 m^2g^{-1} as measured by a methane adsorption isotherm. It is has been found that exposure to the atmosphere for a significant amount of time degrades the adsorption properties of the sample. Exposure to air (especially moist air) is kept to a minimum throughout the production and sample preparation process. Immediately after synthesis, MgO samples are placed in a sealed desiccator, where they are stored until use. To prepare a sample for an adsorption study, the MgO is heated in a stepwise fashion to 950 °C under high vacuum (10^{-7} torr) for a minimum of 36 hours. In addition to removing any atmospheric molecules physisorbed on the surface during and shortly after preparation, this heat treatment homogenizes the MgO (100) surface exposure (Cox and Hendrich 1994). Approximately 0.25 g of MgO is

then loaded into an oxygen-free, high-conductivity (OFHC) copper cell under a dry argon atmosphere and sealed with indium wire.

2.3.2 Gas Handling System

High-resolution volumetric adsorption isotherms are measured using an automated gas handling system (Mursic, Lee et al. 1996). Propane (National Specialty Gases, CP Grade 99.0%) is added to a calibrated volume, where an initial pressure is measured. This gas is then expanded into the sample cell where it is adsorbed onto the MgO. When equilibrium is reached, a final pressure is recorded. The difference in pressures is calculated, and the amount of propane adsorbed is determined. This algorithm is repeated until the saturated vapor pressure is reached. The process is automated using LabVIEW. The pressure is measured using an MKS 690A Baratron® High Accuracy Absolute Pressure Sensor, with a range of 10 or 100 torr (depending on the transducer used) and a resolution of 0.12%. The sample is cooled using an APD DE-202 expander connected to a compressor. The temperature of the sample was controlled within ±2 mK using a Tristan Technologies LTC-10 temperature controller, combined with a silicon diode thermometer located close to the sample position. However, the actual temperature for a given isotherm was calculated by measuring the saturated vapor pressure (SVP) at each temperature set point and using the semi-empirical Antoine equation given below, where pressure is in kilopascal and temperature is in kelvin:

$$\log_{10}(P) = A - \frac{B}{T+C}. \qquad 2.3.1$$

The coefficients used in this calculation are A = 6.757, B = 1045.3 K, C = -7.15 K in the temperature range of 125 K – 165 K with an error of ±0.1 K. For measurements in the range of 165 K – 190 K, the coefficients used were A = 5.92888, B = 803.81 K, C = -26.16 K with a corresponding error of ±1.0 K (Stevenson and Malanowski 1987). The SVP is determined by adsorbing ~ 40 – 50 layers.

2.4 Thermodynamic Results

The thermodynamic results of the adsorption isotherm study are discussed in this section. A description of the isotherm data is given, followed by the results of the monolayer capacity and molecular area of propane on MgO. Finally, the two-dimensional isothermal compressibility is discussed, along with the differential heat and entropy of adsorption.

2.4.1 Isotherm Data

More than forty isotherms were collected, each containing approximately a hundred data points. A temperature range of 130 – 190 K was studied. Measurements at temperatures below 130 K could not be performed because the saturated vapor pressure of propane at these temperatures is too low to be resolved using a 10 torr pressure transducer. The experimental setup enables measurement of the final pressure of the gas

aliquot after equilibrating with the sample. By keeping a running total of the amount of gas admitted into the sample and the final pressure, the propane isotherm can be determined. However, to make an accurate determination of the number of moles adsorbed on the sample, a "dead space" correction must be performed. The "dead space" is the unoccupied volume between the actual sample and the valve that introduces the gas to the sample. Hence, the amount of gas adsorbed to the surface is calculated using the ideal gas law and the following equation,

$$n_{adsorbed} = \frac{(\Sigma\Delta P)V_{cal}}{RT_{room}} - \frac{P_f V_{DS}}{RT_{sample}} . \qquad 2.4.1$$

In the previous equation, $n_{adsorbed}$ is the total number of moles adsorbed, $\sum\Delta P$ is the running total of the pressure of the gas introduced to the sample, V_{DS} and V_{cal} are the "dead space" volume calculated at room temperature and calibrated volume of the gas handling system, respectively.

Figure 2-10 is a representative subset of the complete series of isotherms recorded for propane adsorbed on MgO. The temperatures of the isotherms increase from left to right in the figure. A few key features of this graph should be noted. First, the number of steps observed. Each step represents a distinct layer of propane adsorbed to the surface of MgO; the first step nominally signifies the completion of a monolayer and the second step represents completion of the second layer. In general, very distinct steps in the volumetric isotherms are observed at low temperatures. As the temperature is increased, the layers normally decrease in number and the steps become less well defined. As

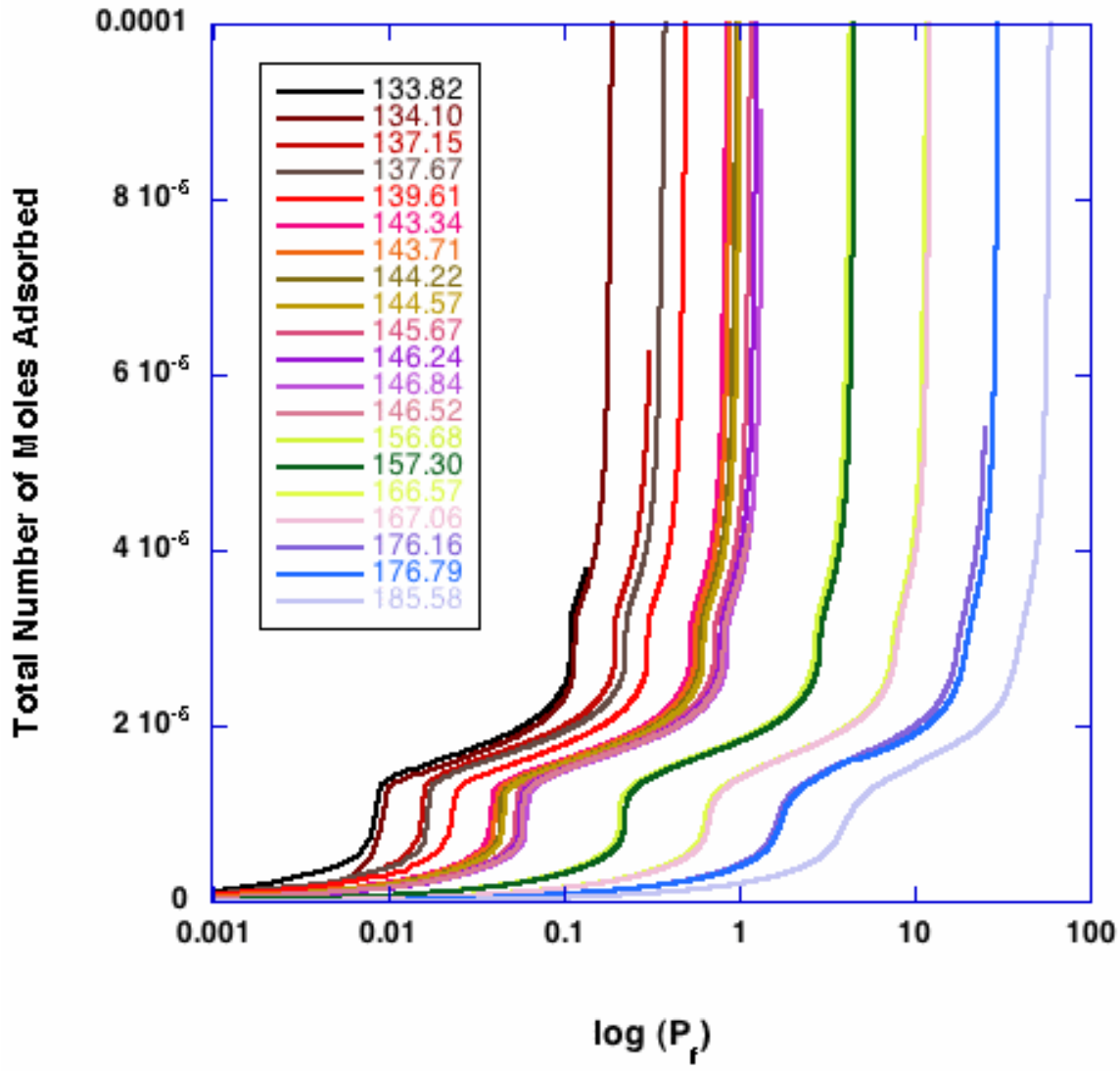


Figure 2-10 A representative set of propane on MgO isotherms.

shown in Figure 2-11, the third layer of propane can only be observed by taking the numerical first derivative of the isotherm, and becomes indistinguishable from the noise at approximately 150K. This observation is attributed to increased thermal motion (e.g., translation and vibration) causing more disorder in layering as temperature is increased; the layers are less distinct at higher temperatures and therefore less easily resolved.

2.4.2 Monolayer Capacity and Molecular Area

It has been noted that the molecular area of propane can be determined from an adsorption isotherm by using the "Point B" method. Figure 2-12 shows a sample isotherm and illustrates how the "Point B" method is used to determine the molecular area. First, a straight line is fitted to the vertical portion of the monolayer step. Next, a linear fit is made to the horizontal portion of the step. Data points on the plateau region of the step were included in the linear fit, with the boundaries of the fit established by visual inspection. Once these lines are determined, the point of intersection is calculated, and the number of moles of propane that nominally occupy the first layer is established. The surface area of the MgO sample is determined using the methane isotherm technique described earlier. With knowledge of the number of moles of propane in a monolayer and the total surface area of the substrate, the molecular area of propane on MgO can be calculated. Figure 2-13 presents the results from a sample of isotherms collected for this study, showing the molecular area of propane measured at various temperatures. Initial observations from this figure show that the molecular area is nearly constant in the region

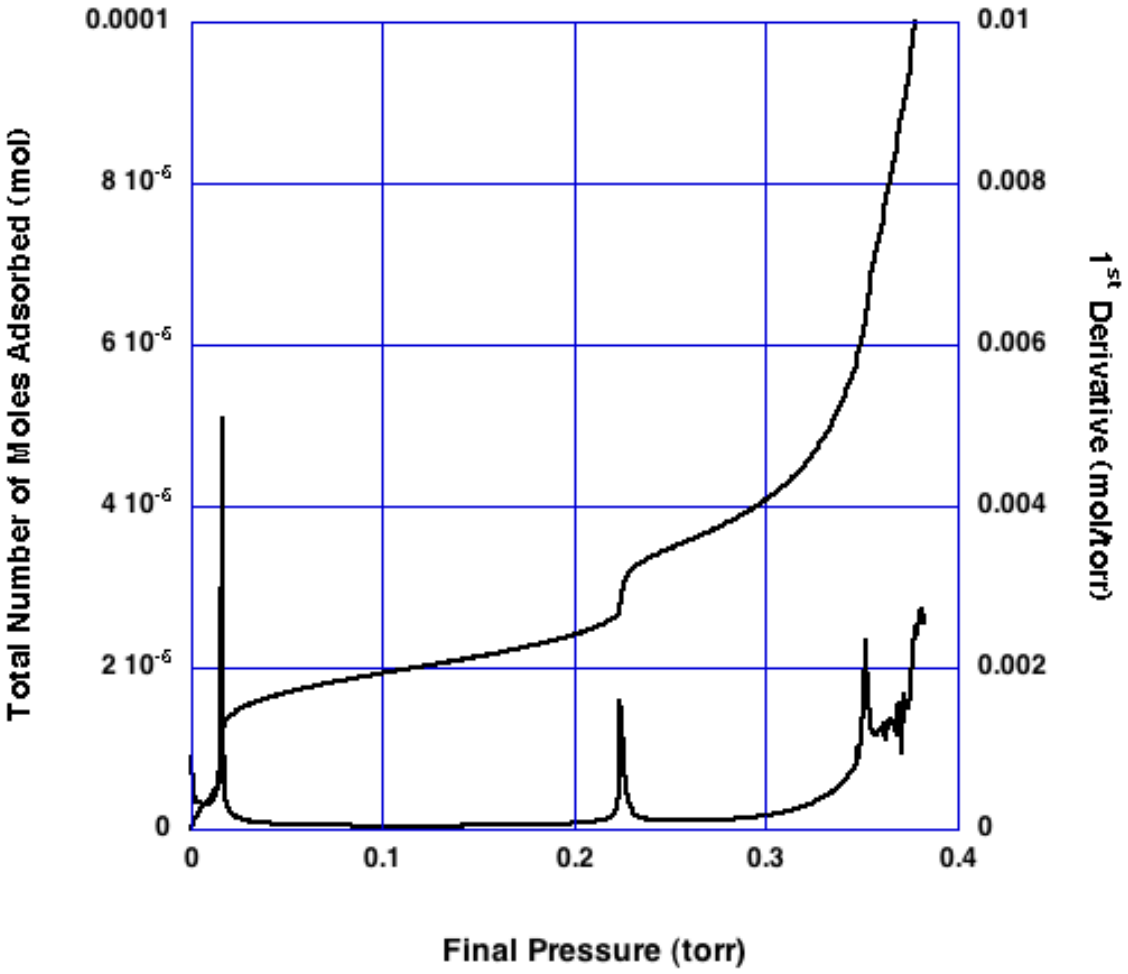


Figure 2-11 Adsorption Isotherm and 1st Derivative of Propane on MgO at 137.67K.

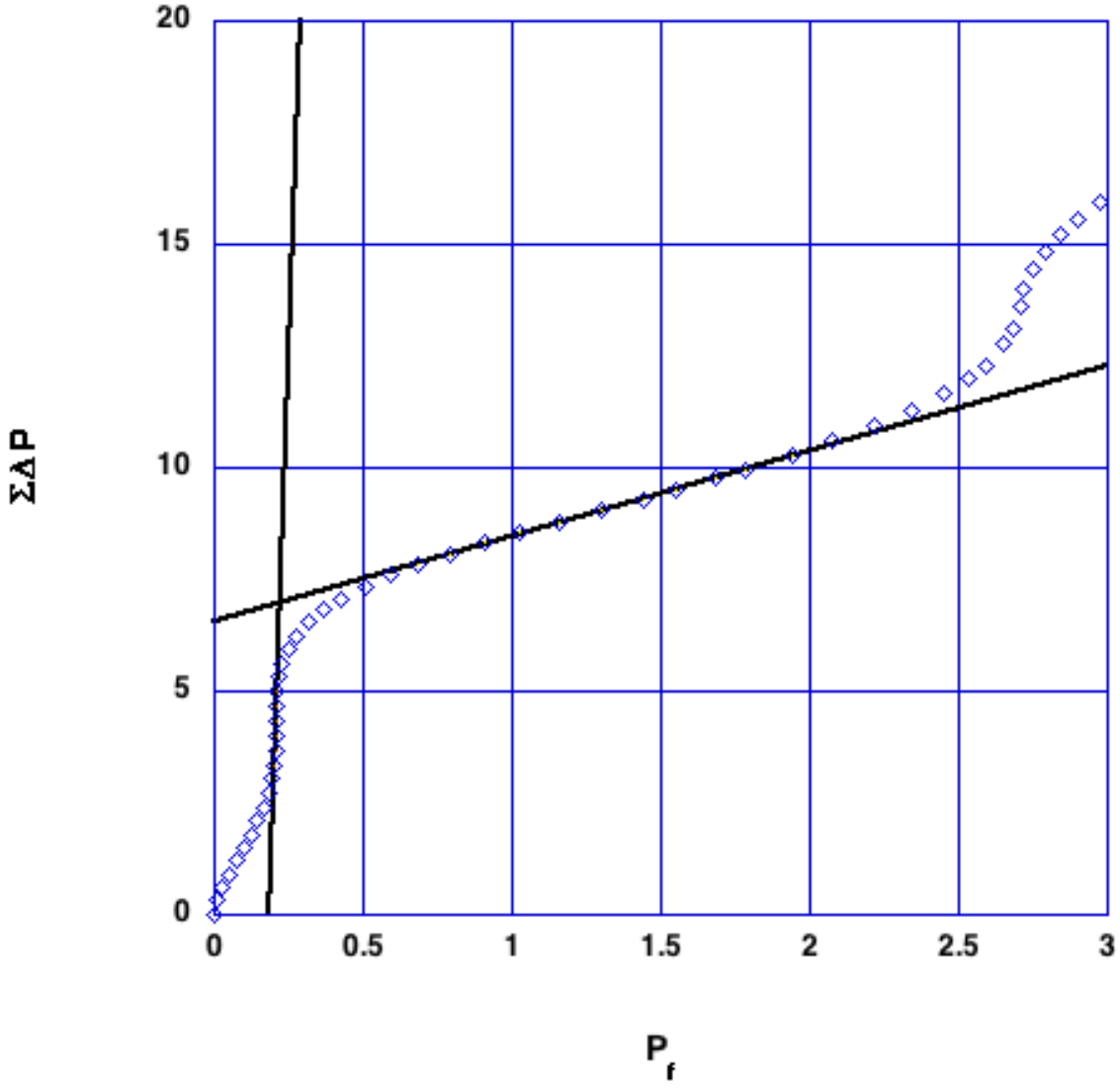


Figure 2-12 Point B method to determine the molecular area of propane on MgO.

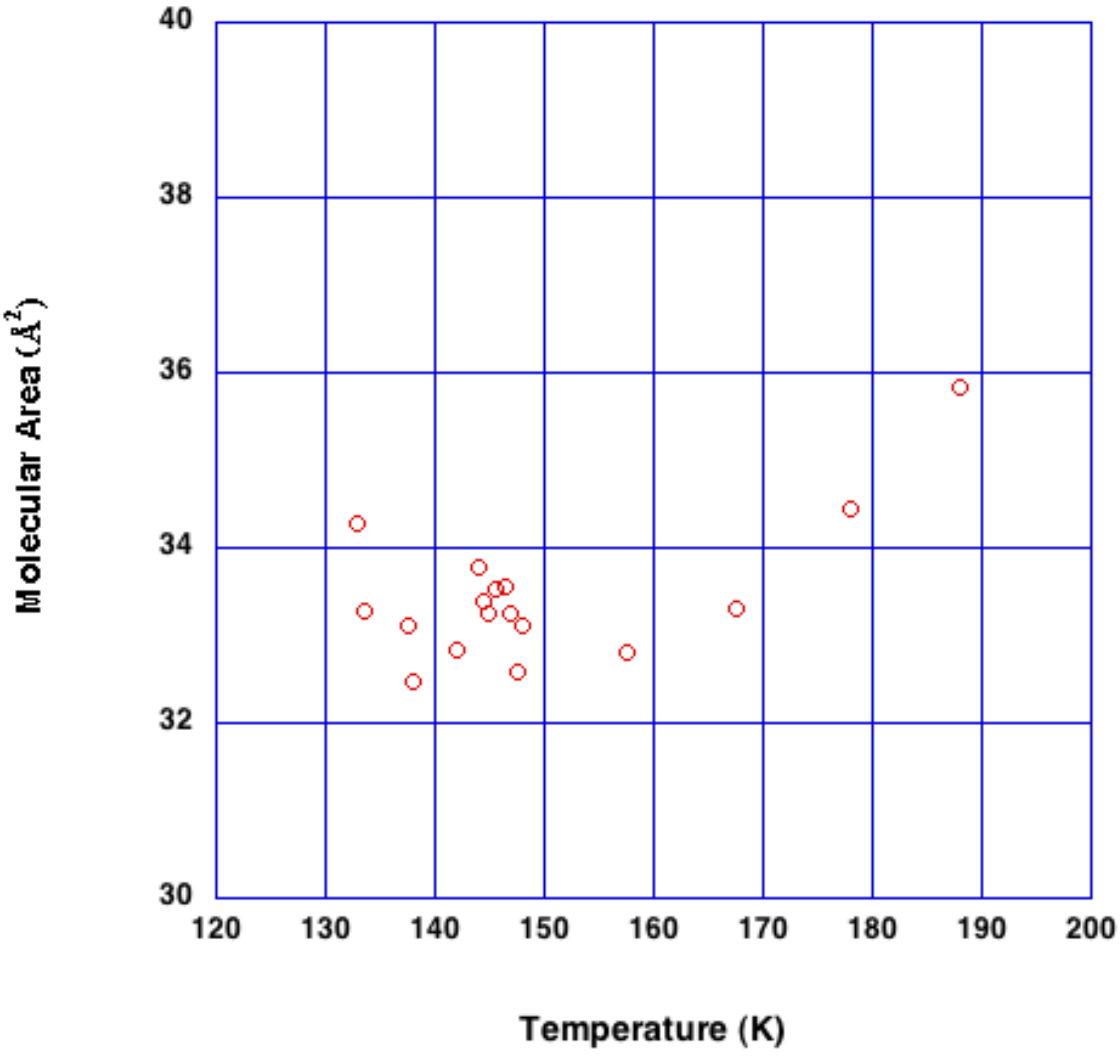


Figure 2-13 Molecular Area of Propane on MgO.

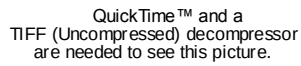
of 33 $Å^2$ at temperatures below approximately 160 K. From further analysis (discussed in the next section), a phase transition is also observed near 160 K. Above this temperature, it seems that the molecular area is gradually increasing, however this observation must be made with some reservation. This method of determining the molecular area has a significant amount of associated error. From a regression analysis of the data, an estimate of the error is ±5 $Å^2$ for each data point. The linear fits to the isotherm data, especially the vertical riser, are not perfect. This is mostly because there are only four to six points in the vertical portion of the isotherm, especially at the higher temperatures. In addition, it might be noticed that the "horizontal" portion of the isotherm after the first step has a distinct positive slope. This is likely due to the promotion of molecules into the second layer and thus a broadened interface. Hence, we observe that the behavior of real isotherms is far from the simple ideal we described earlier, and so too our determination of the number of moles in the first layer using the "Point B" method will have some associated error.

2.4.3 Two-Dimensional Isothermal Compressibility

The two dimensional isothermal compressibility, K_{2D}, is a measure of the spreading pressure as molecules adsorb onto a surface. As more and more molecules adsorb and a condensed layer forms, the spreading pressure increases; a peak appears in the compressibility as the layer completes. The process repeats (compressibility decreases and increases again) as the next layer forms. This cycle of discrete layering

may continue until the saturated vapor pressure is reached. Figure 2-14 depicts the K_{2D} for propane adsorbed on MgO as a function of chemical potential. The figure gives a representative sampling of all the adsorption isotherms taken for this system, showing a temperature range from 155 K to 178 K. As might be expected, the first layer K_{2D} peaks are sharp and well defined. In the first layer, the adsorbate–substrate interaction is large and the motion of the adsorbed molecules is impeded by their strong attraction to the surface; hence, K_{2D} for the first layer is much larger than for the other layers. The second layer K_{2D} peaks are also shown in the figure. The magnitude of these second layer peaks is much smaller than the first layer K_{2D}, again due to the adsorbate-substrate interaction. Both the first and second layer peaks show a general trend of being displaced to higher chemical potential as the temperature is decreased. The third layer K_{2D} peaks are difficult to observe due to the approach of the features to the saturated vapor pressure.

One useful experimental result that can be obtained from the K_{2D} is the temperature location of any phase transitions that may take place in the system. Larher demonstrated that by monitoring the Full Width at Half Maximum (FWHM) of the K_{2D} peaks as a function of temperature, the location of possible phase transitions can be found (Larher 1992). Plotting the FWHM of K_{2D} peaks versus temperature, the transition temperature is determined by locating the change in the slope of the graph. Figure 2-15 and Figure 2-16 show possible phase transition temperatures determined using first and second layer K_{2D} peaks, respectively. To determine the transition temperature and an estimate of the associated error, two lines were fitted to the more vertical portion of the



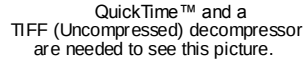


Figure 2-14 Isothermal Compressibility for Propane Adsorbed on MgO.

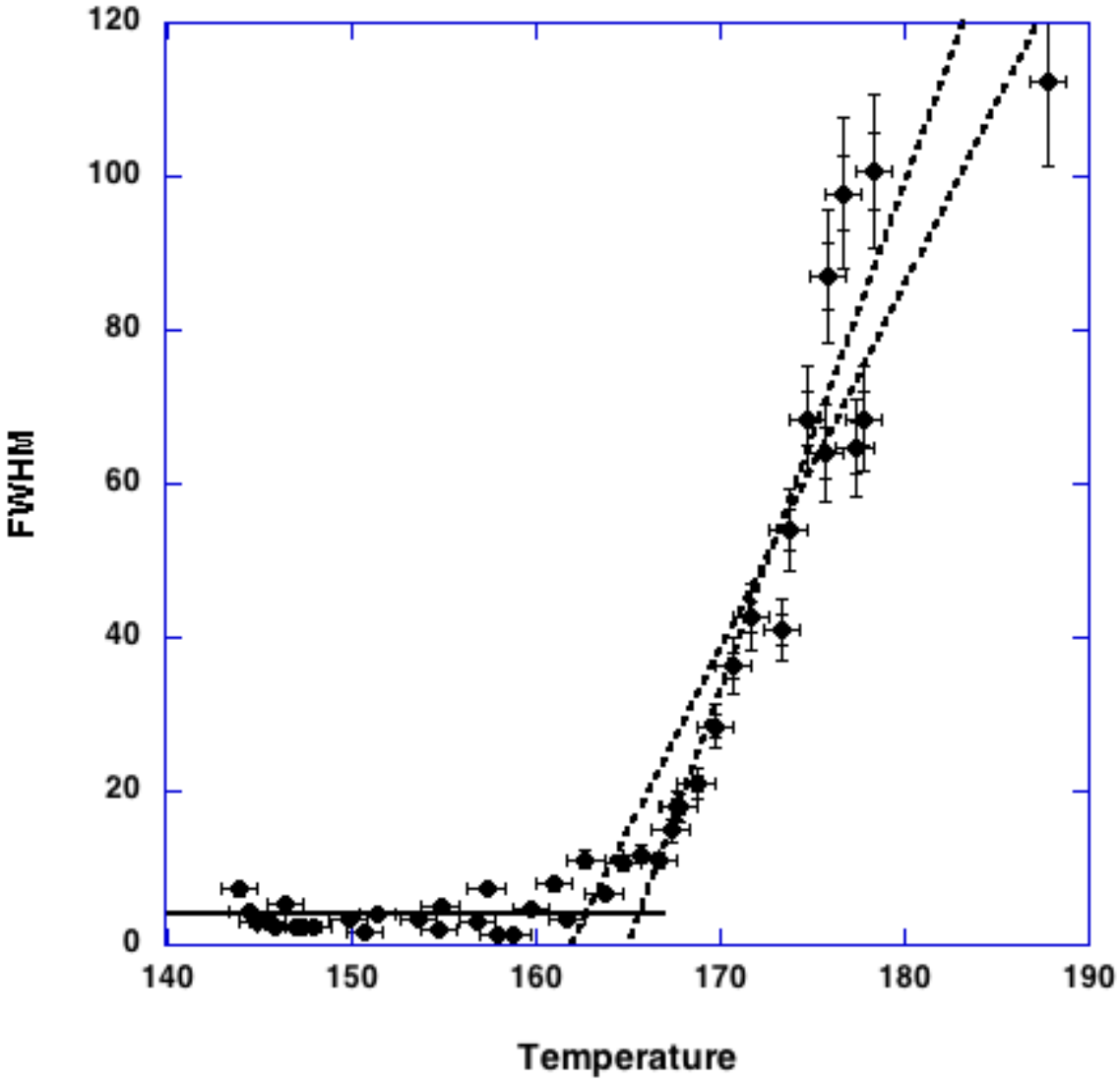


Figure 2-15 FWHM of the First Layer.

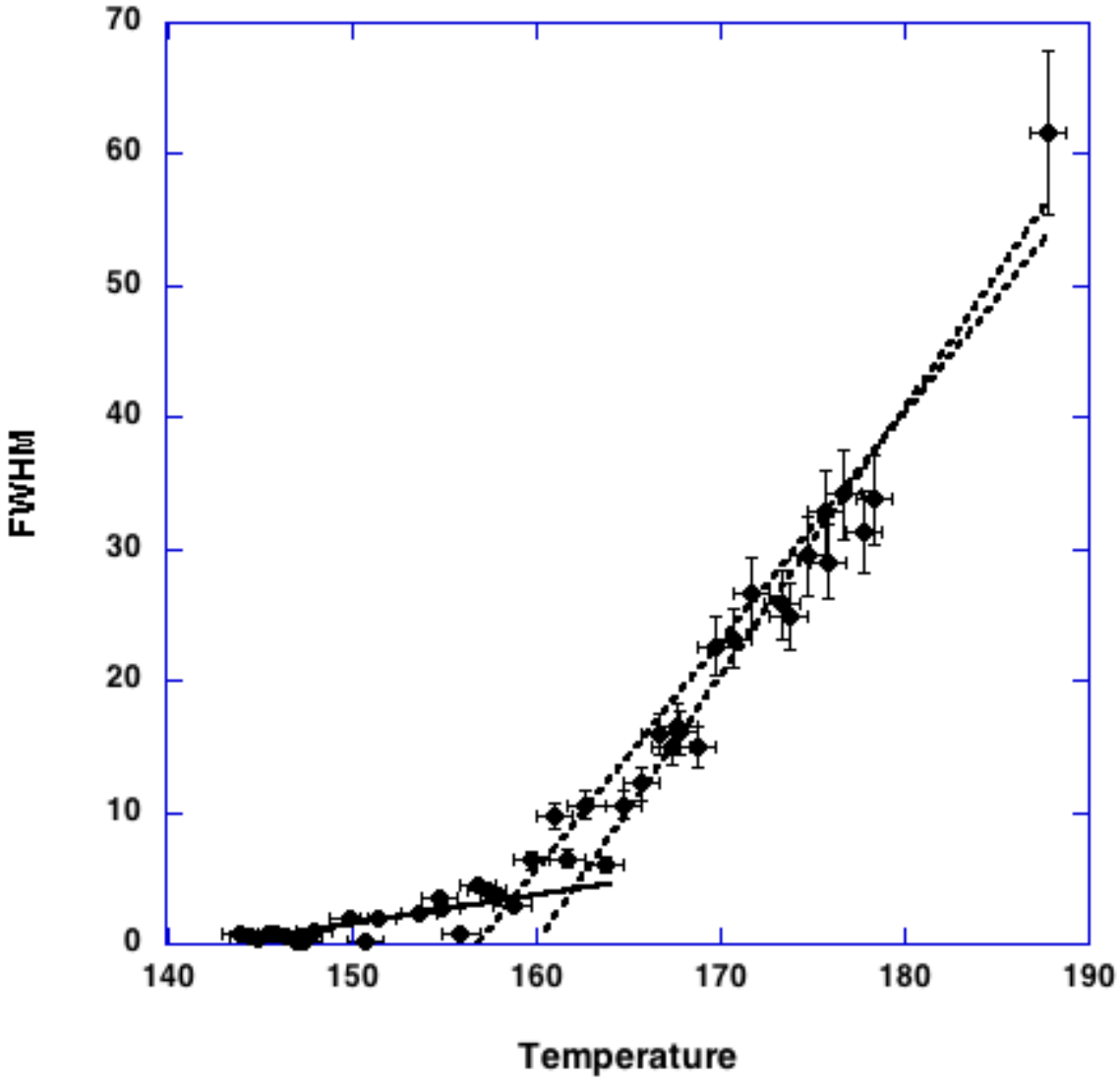


Figure 2-16 FWHM of the Second Layer.

graph (dotted lines), representing the two extremes to the linear fit. The intersections of these two lines with the horizontal fit establish the boundaries of a temperature range for the break in slope and, hence, the possible phase transition temperatures. For the first layer data, the transition temperature is within the range 162 – 166 K, yielding an experimental value of 164 ± 2 K. Fitting the second layer data shows a transition in the range of 158 – 163 K, giving an experimental transition temperature of 160.5 ± 2.5 K. There was insufficient data to calculate a phase transition temperature from third layer K_{2D} peaks.

2.4.4 Two-Dimensional Thermal Expansion

Figure 2-17 represents the coefficient of thermal expansion of propane adsorbed on MgO at 143.5K. The thermal expansion of a material is a measure of how much a material expands with a change in temperature. In this case, the figure shows that at layer completion, propane is slightly susceptible to changes in temperature. To determine the curve in Figure 2-17, two isotherms close in temperature were compared. The data was corrected for "dead space," as previously described. Equation 2.2.14 was used to determine the thermal expansion, with the partial derivative, $(\delta n/\delta T)_P$, approximated by taking the difference between the two isotherms. Isotherm data was interpolated where necessary for direct comparison using the interpolation function provided in KaleidaGraph™.

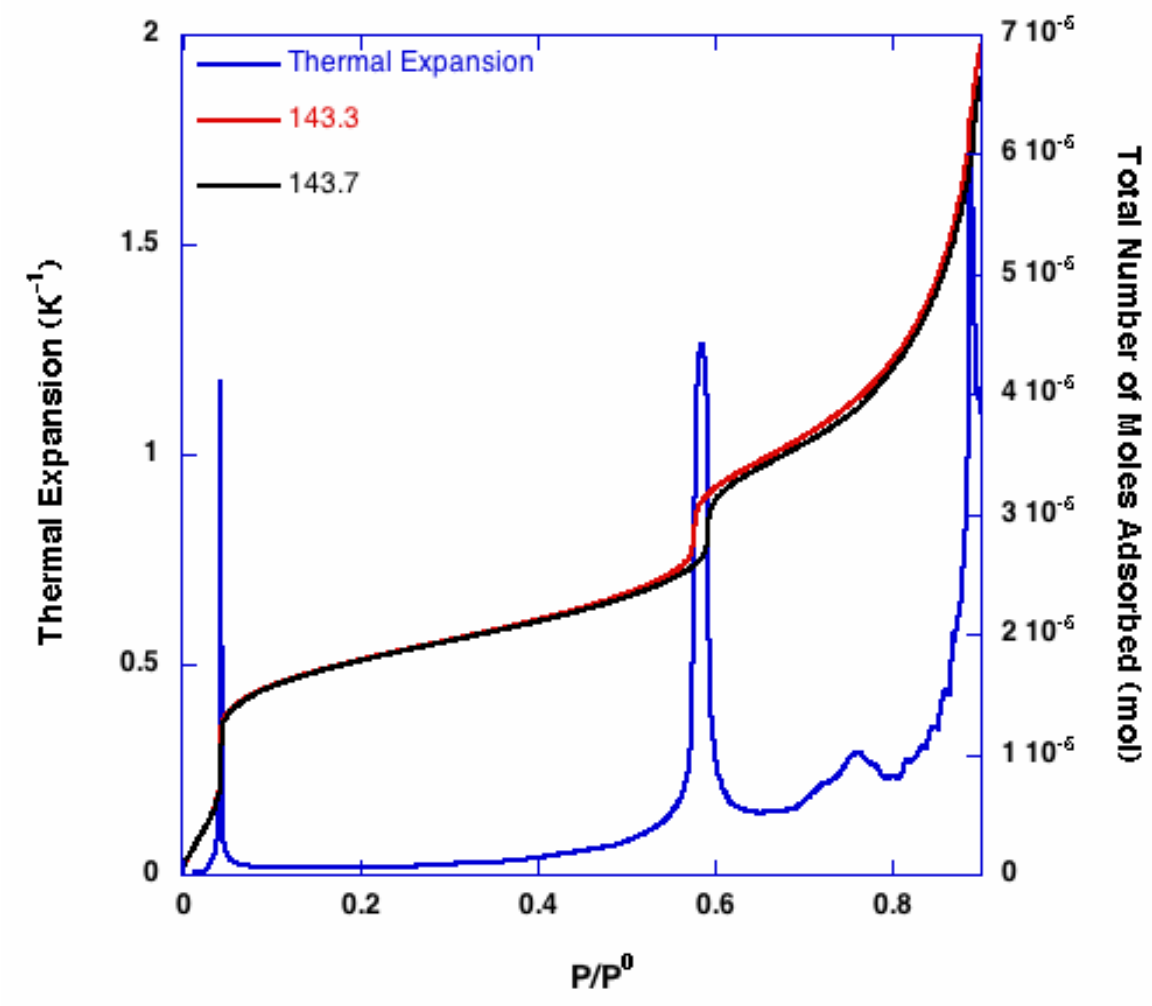


Figure 2-17 Thermal Expansion of Propane on MgO at 143.5 K.

2.4.5 Thermodynamic Quantities

Other thermodynamic quantities that can be calculated are the differential enthalpy (ΔH), differential entropy (ΔS), and heat of adsorption (Q_{ads}) of the system. When the system is in thermodynamic equilibrium, the Clausius – Clapeyron equation in reduced form (Equation 2.2.16) can be used to determine these quantities. From the observed isotherm data, a plot of the natural log of the final pressure at layer completion with respect to the inverse temperature will give a linear function, as shown in Figure 2-18. To determine the final pressure of layer completion, the numerical first derivative of the isotherm is taken. From the slope and y-intercept, ΔH and ΔS can be calculated by using Equation 2.2.17 and Equation 2.2.18. The average heat of adsorption is calculated from Equation 2.2.19. The differential enthalpy, entropy, and heat of adsorption, along with the linear regression analysis are tabulated in Table 2.1.

A few qualitative and quantitative remarks can be made concerning the values in Table 2.1. The most obvious observation is the trend of the heats and entropies approaching zero as the number of layers increase; this is expected, since these differential quantities are calculated relative to the bulk value. Hence, as the number of layers increase, the values approach zero, as the adsorbed layers become more "bulk-like." The differential entropy for each layer is positive, suggesting that the formation of each subsequent layer is less entropically favored as compared to the bulk. Individual layers are more ordered and have less entropy than the bulk structure, but as more layers

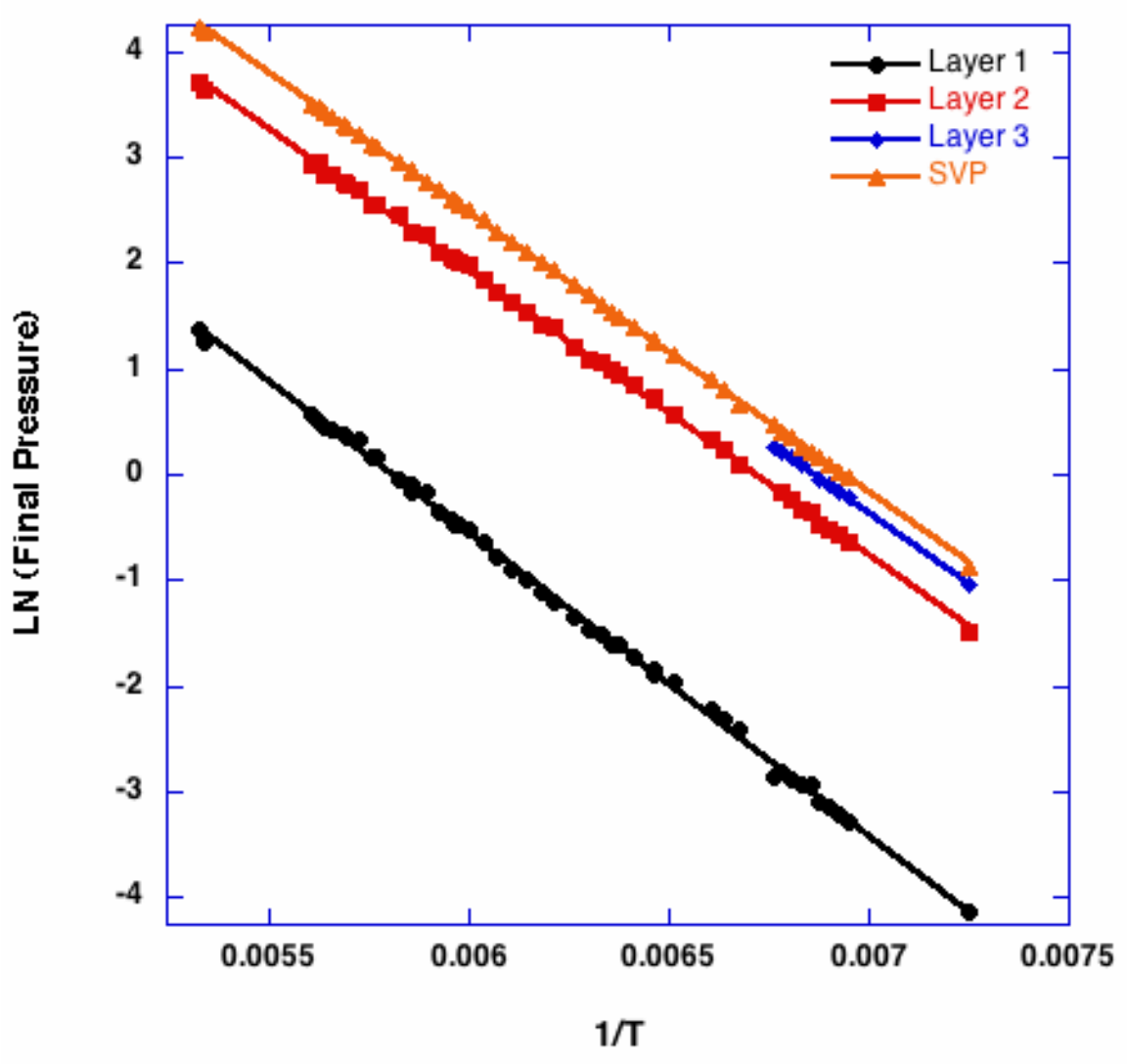


Figure 2-18 Clausius-Clapeyron Plot of Propane on MgO.

Table 2.1 Clausius-Clapeyron Parameters.

	Slope (A)	y-intercept (B)	Q_{ads} kJ/mol	ΔH kJ/mol	ΔS J/Kmol
1st Layer	2864.6 ± 13.5	16.639 ± 0.084	23.804 ± 0.113	-1.865 ± 0.136	13.977 ± 0.849
2nd Layer	2683.7 ± 9.6	18.028 ± 0.059	22.302 ± 0.079	-0.361 ± 0.110	2.435 ± 0.688
3rd Layer	2663.2 ± 24.9	18.28 ± 0.17	22.131 ± 0.207	-0.191 ± 0.221	0.341 ± 1.509
SVP	2640.2 ± 9.1	18.321 ± 0.058	18.321 ± 0.058		

are added they are successively less ordered and more like the bulk structure; hence, the differential entropy decreases with additional layers. Finally, the numerical values fall in line with other small alkanes adsorbed on MgO (Freitag and Larese 2000; Arnold 2005; Yaron, Telling et al. 2006; Chanaa 2008; Cook submitted 2008).

The isosteric heat of adsorption (Q_{st}) is the amount of energy needed to remove an adsorbed molecule from the surface; hence, it is a positive quantity. As mentioned in Section 2.2.3, this thermodynamic value is calculated at constant coverage (isostere) using Equation 2.2.20. Figure 2-19 is an example of the Q_{st} for propane on MgO at 143.5 K. The isosteric heat peaks right before the first and second layer completion (dotted lines), signifying that it takes more energy to bring a molecule onto the surface just as the layer completely forms. The peak symbolizing the third layer is buried in the noise, since it is so close to the saturated vapor pressure. The Q_{st} levels off at the bulk value for the heat of vaporization, 22 kJ/mol. The literature value according to Svoboda is 23.00 kJ/mol; a four percent difference, which is within the experimental error (Majer and Svoboda 1985).

2.5 Structural Simulation Results

Computer modeling simulations were performed to complement the thermodynamic study of propane on MgO and shed some light on the microscopic structure and dynamics of the propane adsorbate on the substrate. The following section

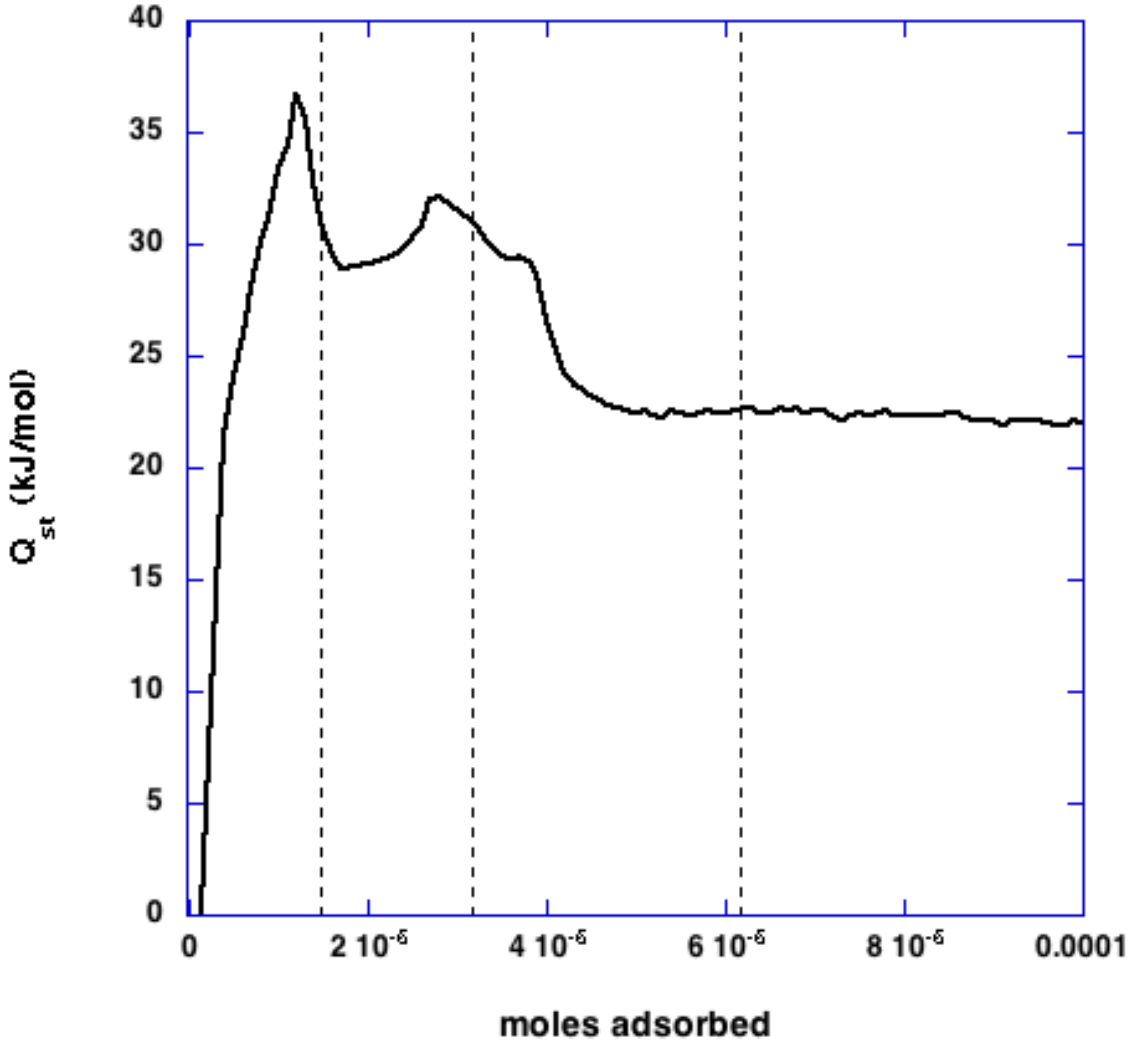


Figure 2-19 Isosteric Heat of propane adsorbed on MgO at 143.5 K.

describes the preliminary work that was performed to begin such a study. The molecular simulation package Materials Studio® by Accelrys was used to carry out the study. Materials Studio is designed to model and simulate the structural properties of numerous materials. In this section, a brief explanation of Materials Studio's Forcite module is given, along with the corresponding results.

2.5.1 Forcite Module[1]

The Materials Studio program is an excellent software package to model a crystalline system. The Forcite module uses molecular mechanics to produce geometry optimizations and single point energy calculations of a single propane molecule adsorbed on the MgO surface. It approximates the potential energy surface of the system by using a classical force field. A force field is a set of functions or parameterized data that is derived from experimental or high-level computation work and can be used to determine many experimental parameters.

There are many advantages to using a force field based simulation; most relevant for the propane on MgO study is that the simulation can handle large systems. While propane is comprised of only eleven atoms, the MgO crystal modeled in this study was

---

[1] The training manual for Materials Studio was used extensively as a reference for this section. Sections of the manual that were consulted include "About Forcite" and

made up of 486 atoms in a 9×9×6 lattice, with 81 atoms on the adsorption surface. Another advantage is that the results of the simulation can be broken up into individual energy contributions. Finally, constraints can be imposed, such as keeping the atomic coordinates of an atom constant. This is in agreement with our experimental observations that the MgO crystal structure and surface do not show reconstruction upon adsorption of alkanes.

The specific force field used in the simulation is the COMPASS force field. COMPASS stands for Condensed-phase Optimized Molecular Potentials for Atomistic Simulation Studies and is a newer version of the force field PCFF, a polymer consistent force field. COMPASS is an *ab initio* force field that has been parameterized and validated using condensed-phase properties, in addition to various *ab initio* and empirical data for molecules in isolation. Accordingly, this force field gives an accurate prediction of the structural, conformational, vibrational, and thermophysical properties for a broad range of molecules, including the alkanes (Sun 1998).

While the Forcite module in Materials Studio can be used to perform molecular dynamics simulations, the only tasks of interest here are the single-point energy calculation and the geometry optimization. The single-point energy calculation gives the non-bonding energies, specifically the van der Waals energy, of a propane molecule on the surface of MgO. A geometry optimization is performed to obtain the optimal orientation of the propane molecule on the surface. The Smart algorithm is used to

determine the geometry with the minimum energy. This algorithm utilizes three different subroutines: steepest descent, ABNR (Adjusted Basis set Newton-Raphson), and quasi-Newton.

2.5.2 Setting up a Forcite Calculation

To begin a Forcite calculation, the MgO surface needs to be constructed from the pure crystal, followed by the construction and optimization of the propane molecule. To construct the MgO (100) surface, the pure MgO crystal structure was imported from Materials Studio's built-in structure library. A geometry optimization was then performed on this structure to optimize both the cell and the atomic positions. When optimizing a crystal structure, Forcite automatically imposes symmetry constraints by preserving the space group of the crystal. Next, the optimized structure was cleaved so only the (100) surface was exposed. The geometry optimization was performed again, but this time the middle layers were constrained so that only the surface was optimized. Finally, a vacuum space was built around the MgO. The propane molecule was also built, and its geometry was separately optimized.

2.5.3 Geometry Optimization of Propane on MgO

The main purpose of performing these Forcite calculations was to determine the position and orientation of an isolated propane molecule on the MgO (100) surface. In

order to limit the number of possible starting positions, the initial location of propane on the surface was restricted to the four high symmetry adsorption sites described in Section 2.2.2 and depicted in Figure 2-7. Figure 2-7 shows only three of these adsorption sites; naturally there are two A-top sites, one above the O^{2-} (shown) and the other above the Mg^{2+} ions (not shown). The following sections will discuss the results of Forcite simulations with propane initially placed over the hollow, bridge, and each of two A-top sites. The calculated energies have an associated error of 0.0003 kcal/mol.

2.5.3.1 Hollow site

There are three likely orientations of the propane molecule in relation to each adsorption site on the MgO (100) surface. The first has the molecule situated with two hydrogen atoms equidistant from the surface. Two other orientations are with three and four hydrogen atoms toward the surface, respectively. While a fourth orientation would have the molecular axis perpendicular to the MgO (100) plane, it is readily recognized that this is not a likely orientation that represents a minimum in the adsorption energy—it was verified by several quick tests that the molecule rapidly moves so that the molecular plane is parallel to the surface. Figure 2-20 shows the three initial orientations of the propane molecule over the hollow site. From these initial orientations, the propane molecule was systematically rotated around the three major axes and placed at distances of 2, 4, 6, and 10 Å above the surface, resulting in 191 unique starting positions. Taking

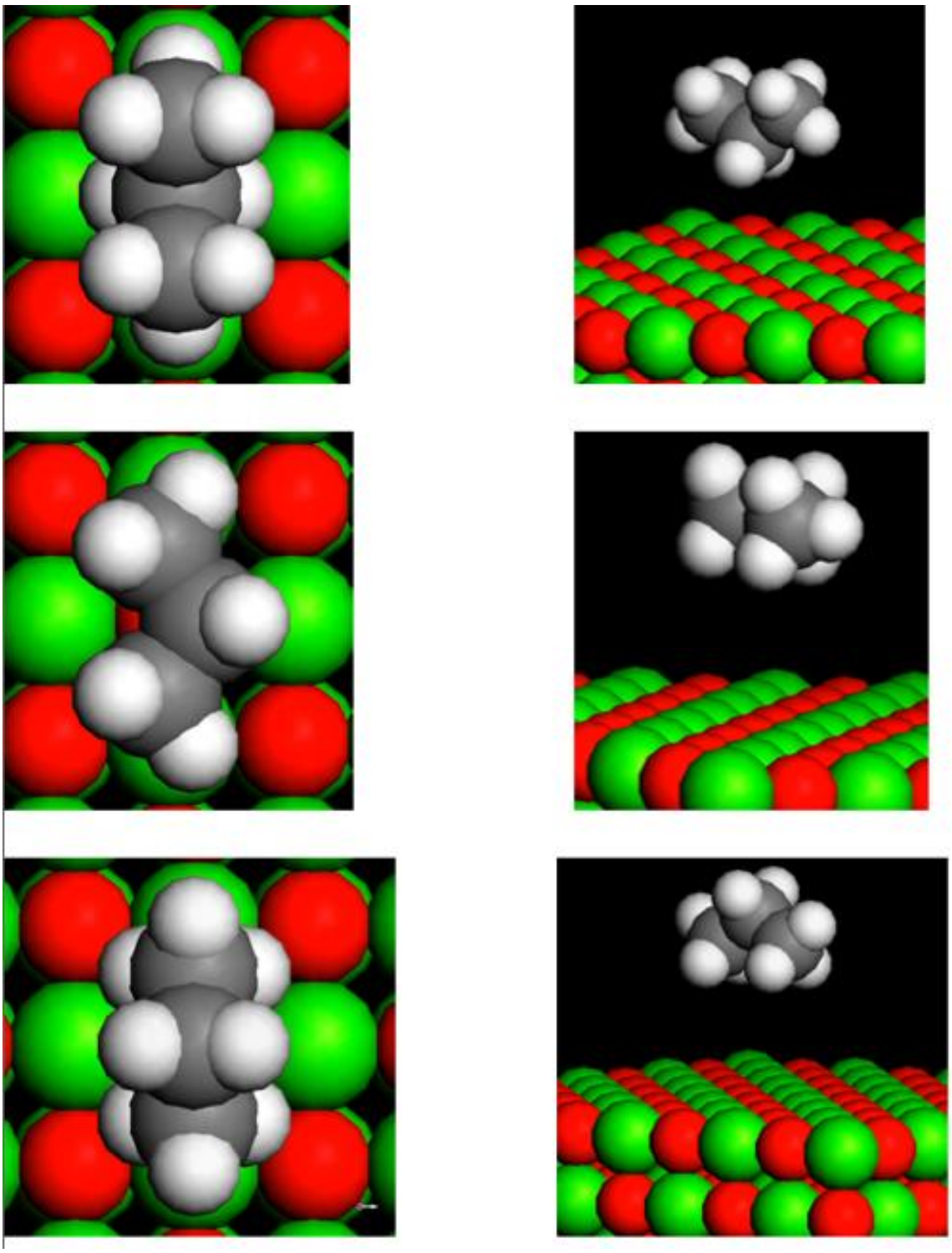
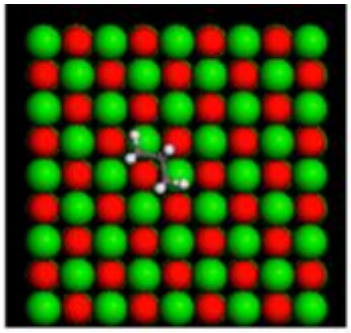


Figure 2-20 The three initial orientations of propane on MgO.

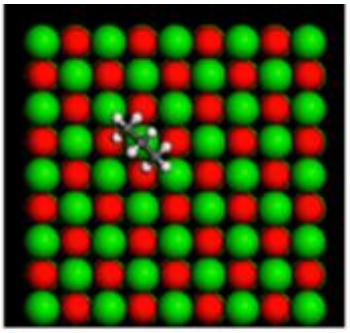
into account the four-fold surface symmetry, this is an excellent sampling of all possible orientations of propane with respect to the surface. The geometry minimizations resulted in seven favored orientations for propane on the MgO surface, shown in Figure 2-21. The energy and distance of the propane's center of mass above the surface are also given in Figure 2-21 for each orientation. As seen in this figure, the global minimum occurs at -13.703 kcal/mol, where the propane molecule could be thought of as "hugging" an oxygen atom. The carbon backbone is parallel to the magnesium ions, similar to the starting orientation with three hydrogen atoms toward the surface.

2.5.3.2 Bridge Site

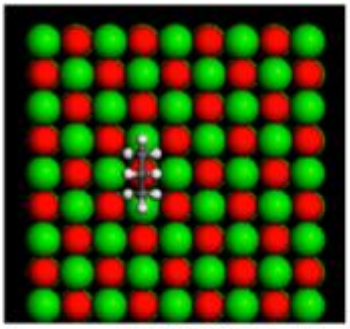
As mentioned previously, the bridge site is the position between nearest neighbor magnesium and oxygen ions. The starting orientations of the propane molecule at the bridge site were similar to those in the hollow site simulations. Because of the different symmetry seen on the surface at the bridge site, 168 unique positions were generated. With propane initially being placed above the bridge site, the geometry minimizations yielded seven favorable orientations. Figure 2-22 shows these structures, along with the calculated energies and center of mass distances for each structure. As seen in this figure, the global minimum occurs at -13.703 kcal/mol, and the propane molecule can be thought of as "hugging" a magnesium ion. The carbon backbone is parallel to the magnesium ions, with three hydrogen atoms toward the surface.



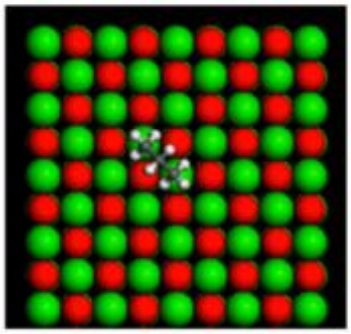
Energy = -13.702550 kcal/mol
CoM = 3.17949 A



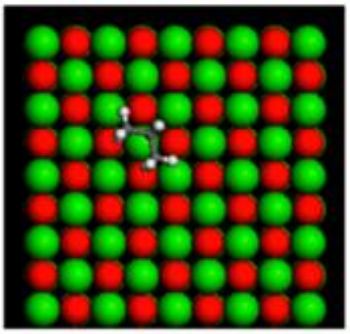
Energy = -13.687635 kcal/mol
CoM = 3.18757 A



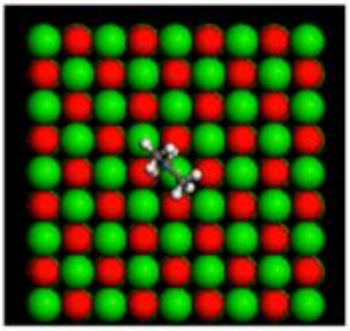
Energy = -13.596796 kcal/mol
CoM = 3.3606 A



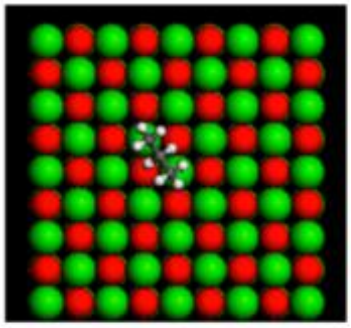
Energy = -13.142436 kcal/mol
CoM = 3.31376 A



Energy = -13.119574 kcal/mol
CoM = 3.3396 A

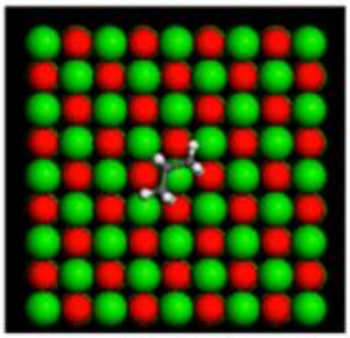


Energy = -12.530321 kcal/mol
CoM = 3.53198 A

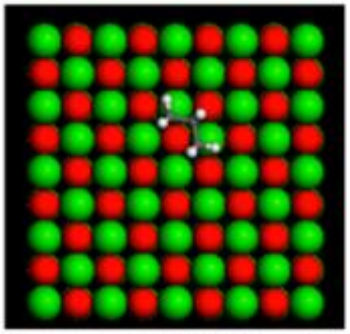


Energy = -12.064562 kcal/mol
CoM = 3.57328 A

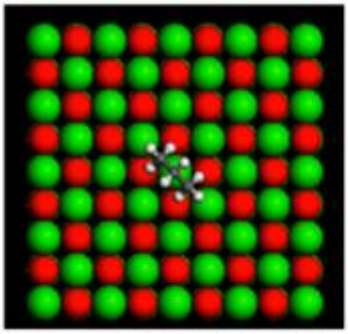
Figure 2-21 Orientation of Propane on MgO with the initial starting position above the hollow site.



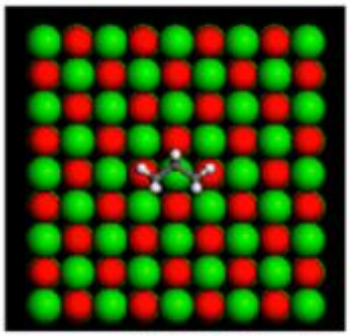
Energy = -13.702715 kcal/mol
CoM = 3.17953 A



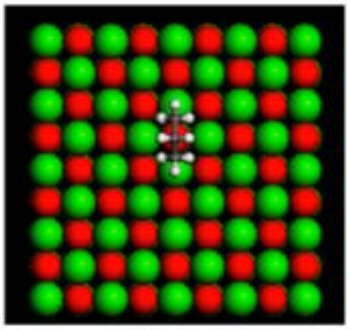
Energy = -13.687634 kcal/mol
CoM = 3.18754 A



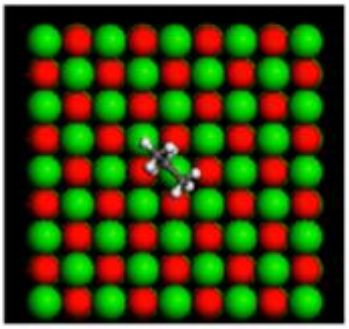
Energy = -13.596796 kcal/mol
CoM = 3.36059 A



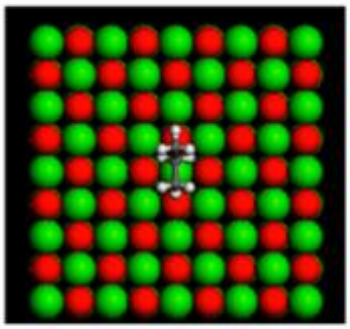
Energy = -13.508519 kcal/mol
CoM = 3.19534 A



Energy = -13.142436 kcal/mol
CoM = 3.31376 A



Energy = -12.530321 kcal/mol
CoM = 3.53202 A



Energy = -12.450613 kcal/mol
CoM = 3.48983 A

Figure 2-22 Orientation of Propane on MgO with the initial starting position above the bridge site.

2.5.3.3 Magnesium and Oxygen A-Top Sites

In the same manner as before, 256 unique positions (128 each for the Mg and O A-top sites) were generated due to the symmetry seen on the surface at each A-top site. The geometry minimizations resulted in ten different orientations for propane initially placed over an oxygen ion, and ten different orientations for propane initially positioned above magnesium. Figure 2-23 and Figure 2-24 show these structures, along with their corresponding energies. As seen in the figures, the global minimum for each scenario occurs at -13.703 kcal/mol and -13.702 kcal/mol for the oxygen and magnesium A-top positions, respectively. In both instances, the propane molecule could be thought of as "hugging" a magnesium atom, with the carbon backbone parallel to the magnesium ions (similar to the starting orientation with three hydrogen atoms toward the surface).

2.5.3.4 Concluding Remarks

Three general structural motifs are observed for the minimum energy geometries. In relation to the carbon backbone, the first two motifs have the propane molecule either lying with the carbons on top of the hollow sites (lowest energy), or lying on top of the ions. The third motif only has two of the carbon atoms close to the surface, with the third slanted upwards away from the surface; this structural pattern results in a much higher energy than the other two. The energies of individual structures within each motif are for all practical purposes degenerate; this will be discussed in more detail in the following section. Finally, the approximate center of mass distance for the propane molecule is 3.2,

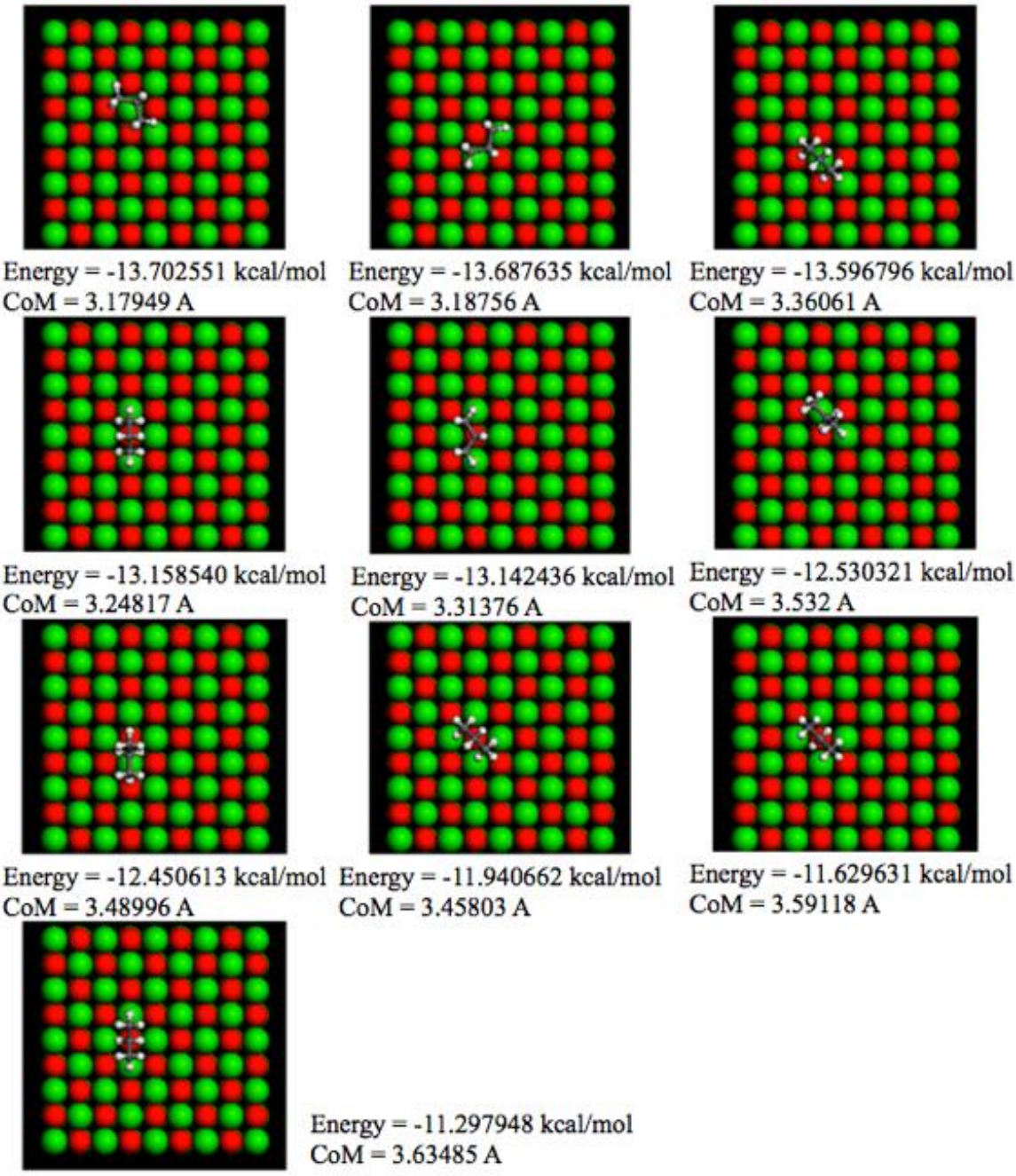


Figure 2-23 Orientation of Propane on MgO with the initial starting position above the oxygen A-top site.

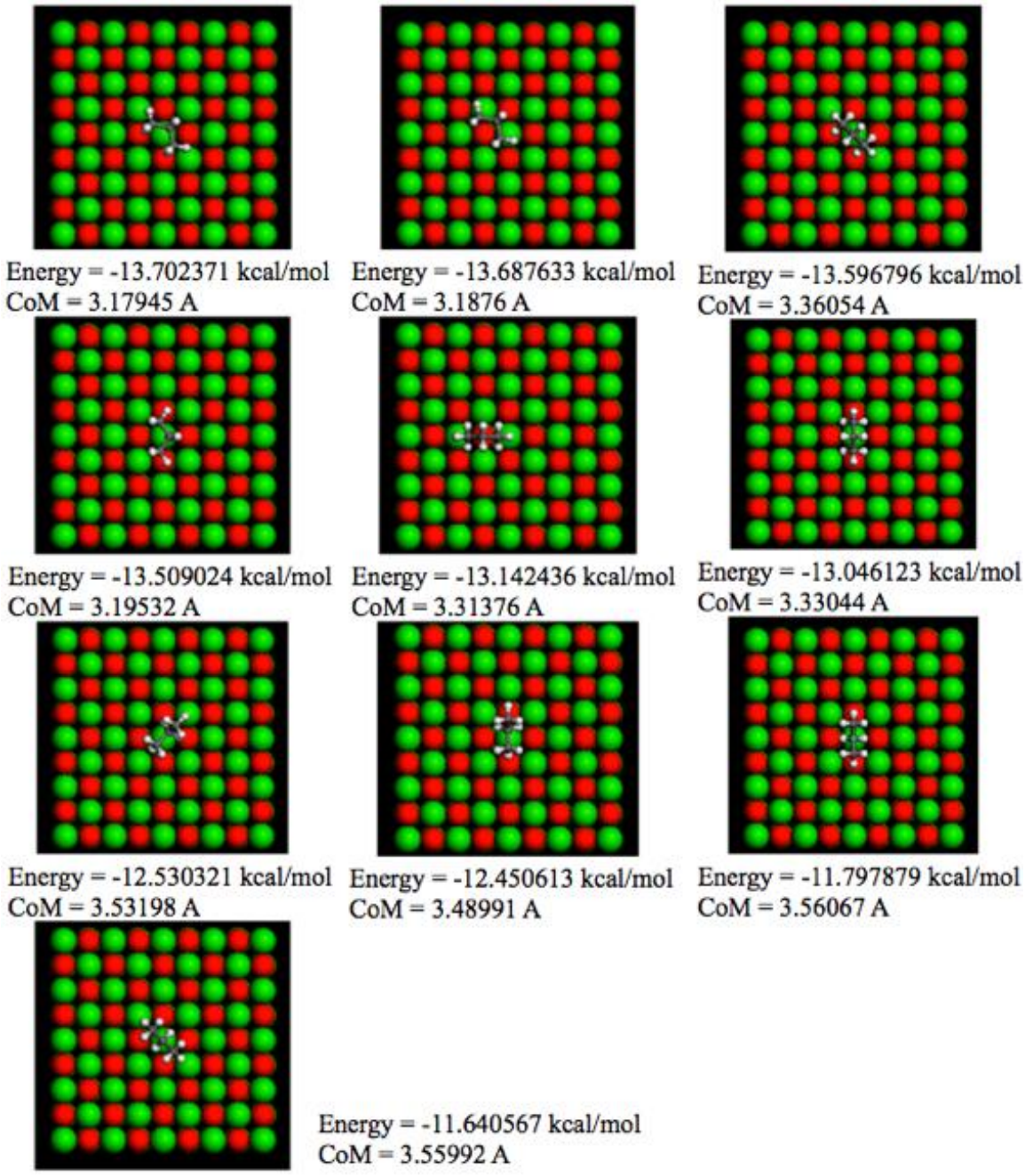


Figure 2-24 Orientation of Propane on MgO with the initial starting position above the magnesium A-top site.

3.3, or 3.5 Å depending on how the molecule is lying on the surface.

2.5.4 Potential Energy Surface

Using the global minimum energy that was determined in the previous section, areas of the potential energy surface were calculated. Figure 2-25 shows the starting configuration for the propane molecule on the MgO surface. With the carbon backbone parallel to the magnesium ions, the propane center of mass is positioned slightly off-center from the magnesium ion, and three hydrogen atoms are close to the surface. This configuration corresponds to the minimum energy calculated with the starting position at the bridge site (see Figure 2-22). The calculated total energy of the system for this particular configuration is equal to -13.703 kcal/mol. Since only the interaction of propane with the MgO (100) surface is of interest, the energy of an isolated propane molecule (-5.146 kcal/mol) must be subtracted from all the calculated energies.

To begin sampling the potential energy surface, the distance was varied between the center of mass of the propane molecule and the MgO surface. Figure 2-26 shows the results of this variation. As shown on this figure, the minimum energy occurs at a distance of 3.18 Å. Another point to note is that as the propane molecule approaches the surface, a large repulsion is observed (as expected). Finally (for completeness sake), the energy goes to zero as the propane molecule approaches infinity. 6-12 Lennard Jones and 10-4 potential fits were attempted for the potential energy surface, but neither

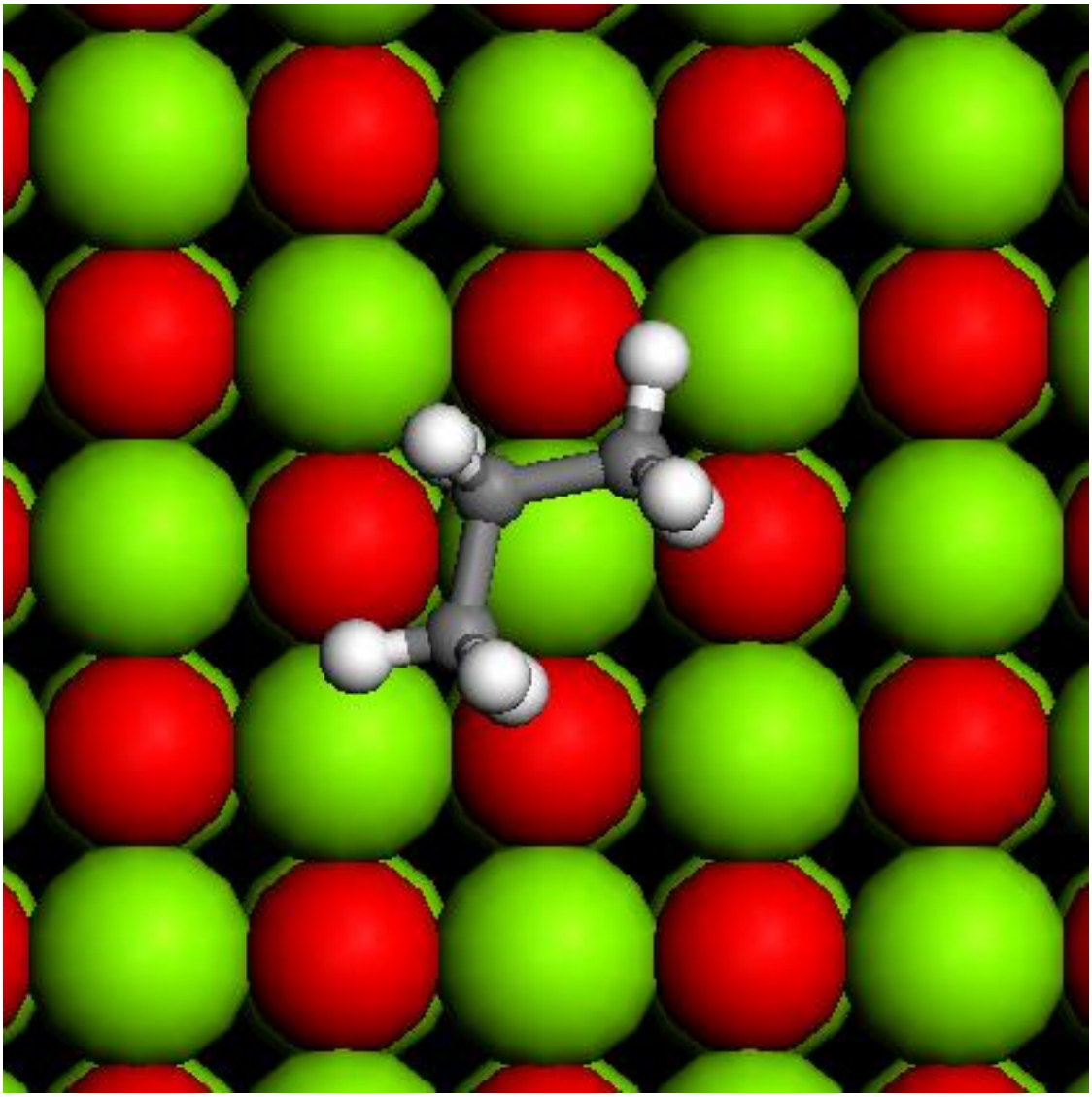


Figure 2-25 Minimum energy configuration of propane on MgO (100).

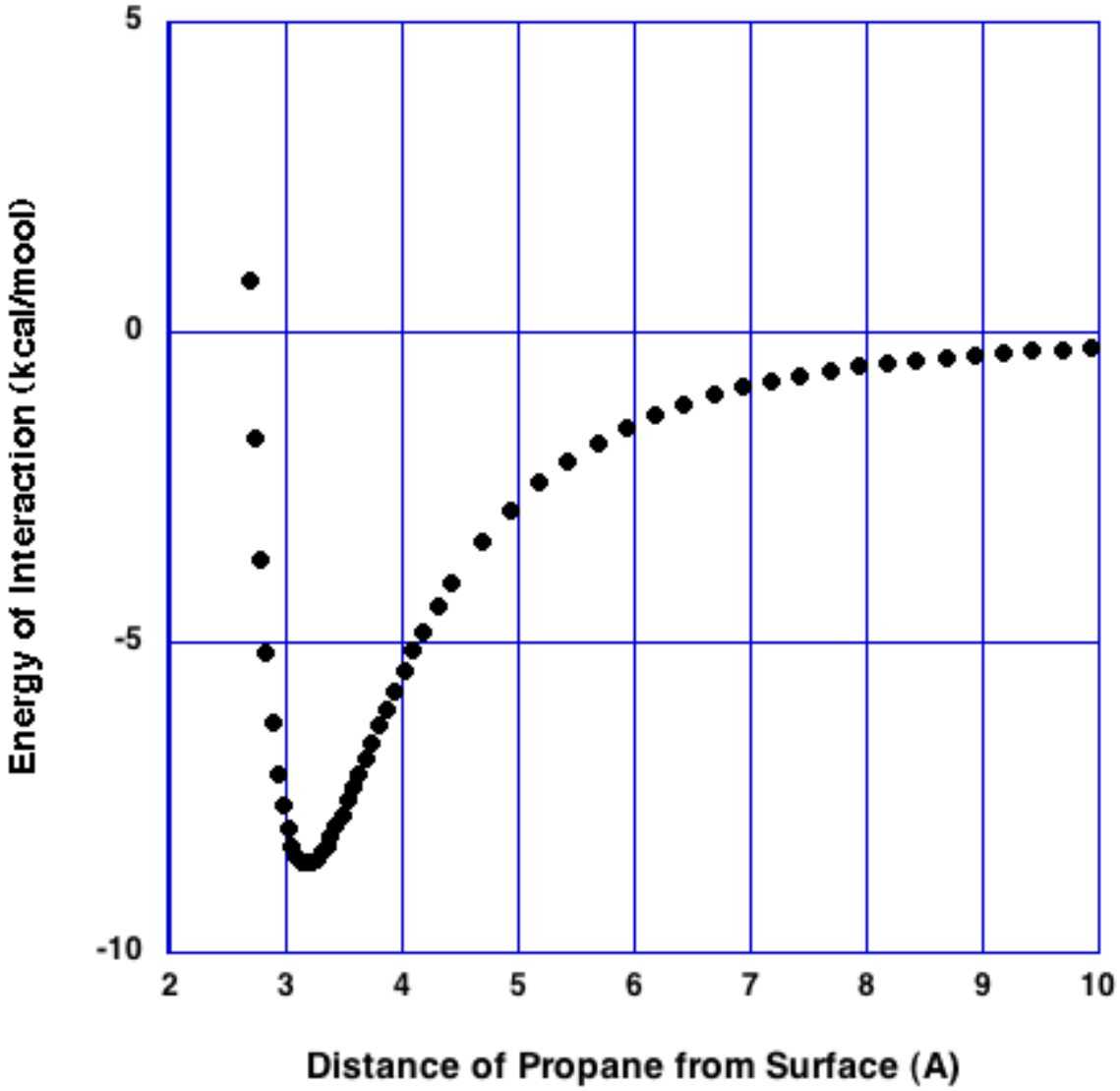


Figure 2-26 Potential Energy of propane as a function of center of mass distance from the surface.

function could satisfactorily reproduce the turnover in the potential energy curve.

The next three figures show the energy change as the propane molecule moves along the surface (i.e. relative to the corrugation caused by the magnesium and oxygen ions). Figure 2-27 is the result of moving the molecule in the x direction. This initially places the propane molecule over a magnesium ion followed by an oxygen ion. The slight shoulder seen in the graph corresponds to the molecule passing over a bridge site. The maximum energy is observed when the molecule is directly over an oxygen ion. Figure 2-28 is the result of moving the molecule along the row of magnesium ions that are perpendicular to the carbon backbone. The maximum shown on this figure occurs when the center of mass is just past the hollow adsorption site and the two hydrogen atoms bonded to the middle carbon are directly above a magnesium ion. Figure 2-29 shows the results of moving the propane molecule along the row of magnesium ions that are parallel to the carbon backbone. As expected, the maximum occurs when the center of mass is over the hollow adsorption site and the hydrogen atoms bonded to the middle carbon are directly over the oxygen ion.

Finally, Figure 2-30 and Figure 2-31 give the potential energy of the system as a function of rotation. Figure 2-30 rotates the propane molecule about the z-axis and Figure 2-31 rotates the molecule about the carbon backbone. Figure 2-30 shows two local minima (90° and 150°) for rotation about the z-axis, with 180 degree symmetry as expected from the surface structure. Unlike the z rotation, the energy as a function of

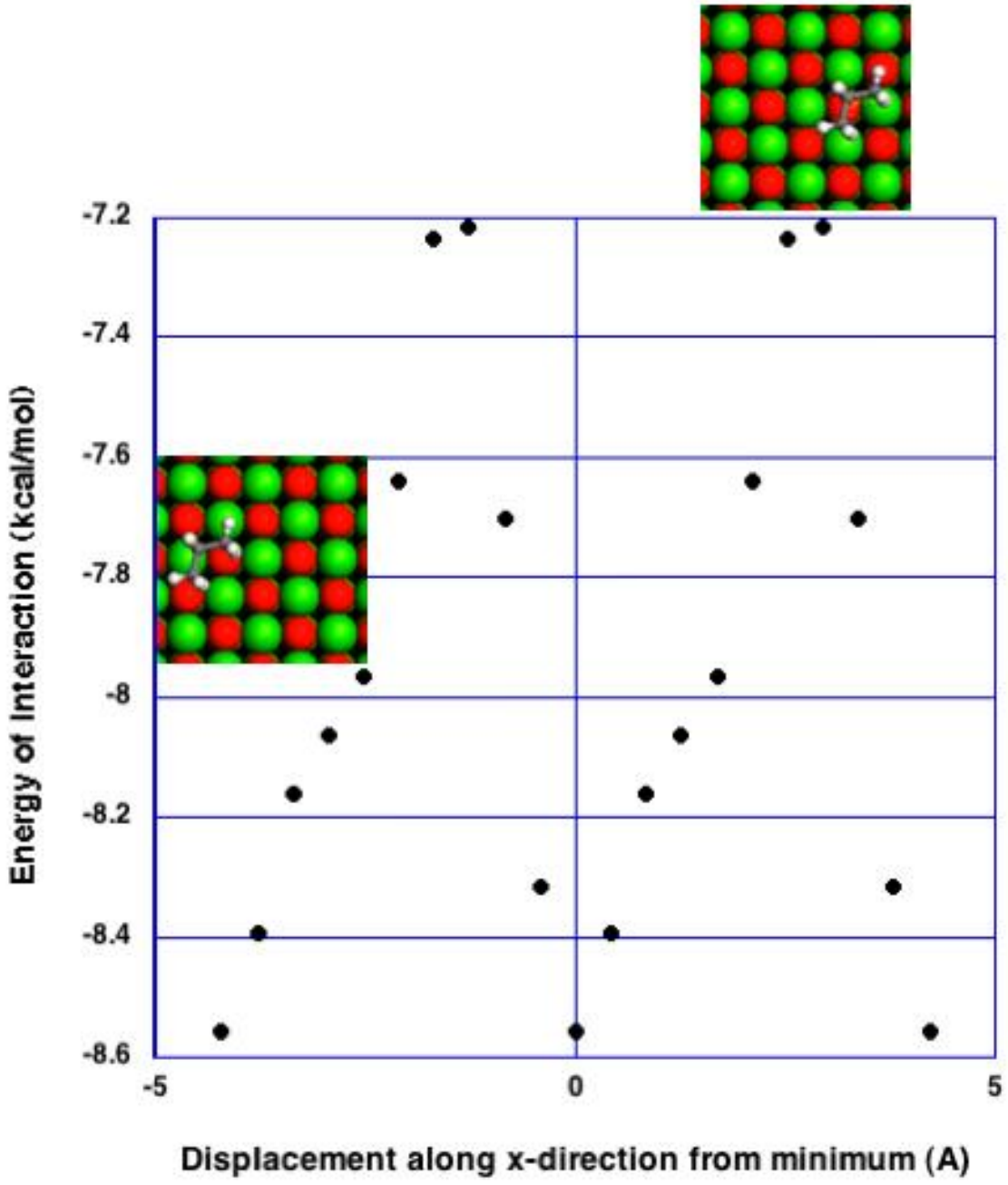


Figure 2-27 Energy as a function of displacement in the x-direction.

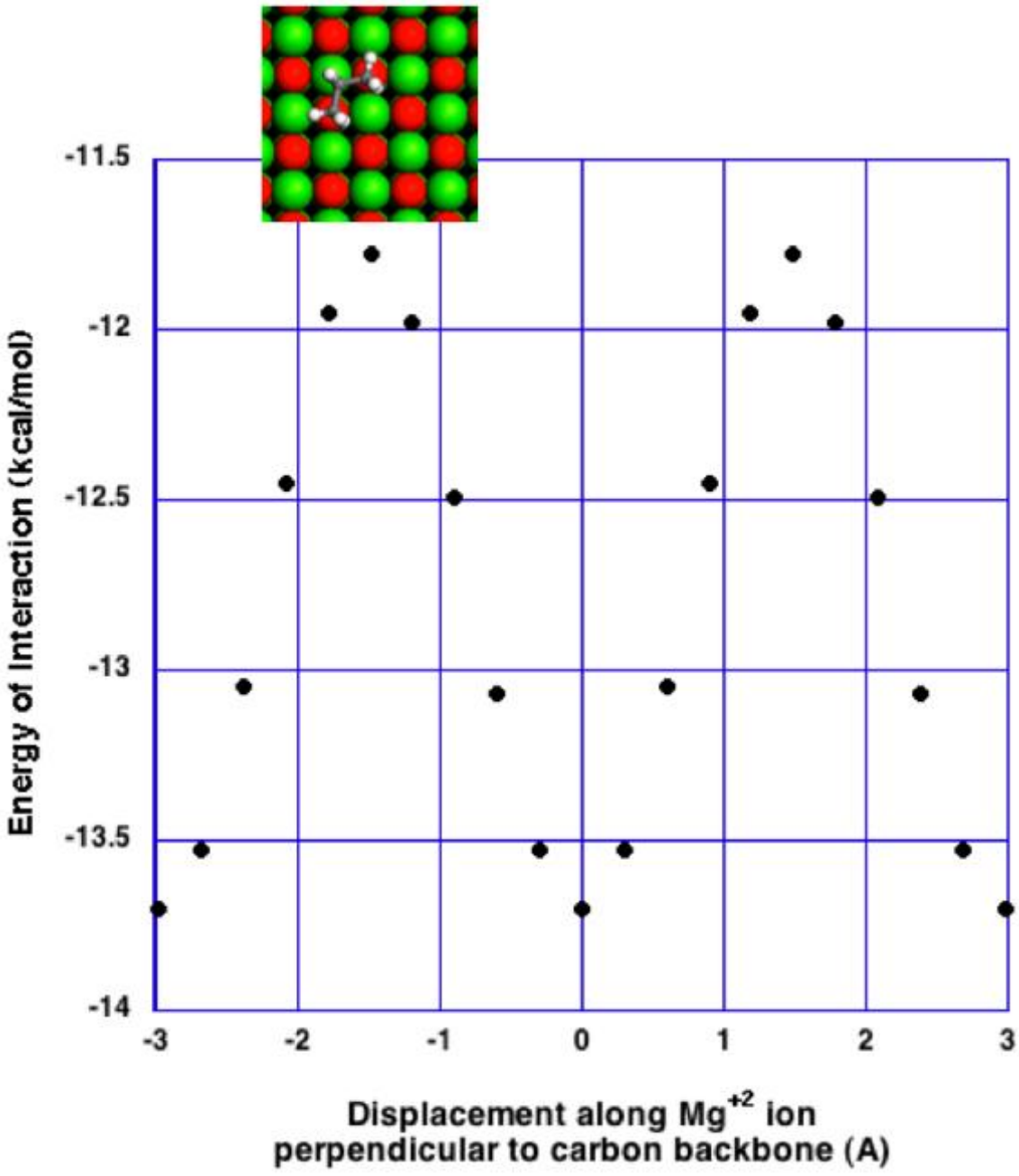


Figure 2-28 Energy as a function of displacement perpendicular to the carbon backbone.

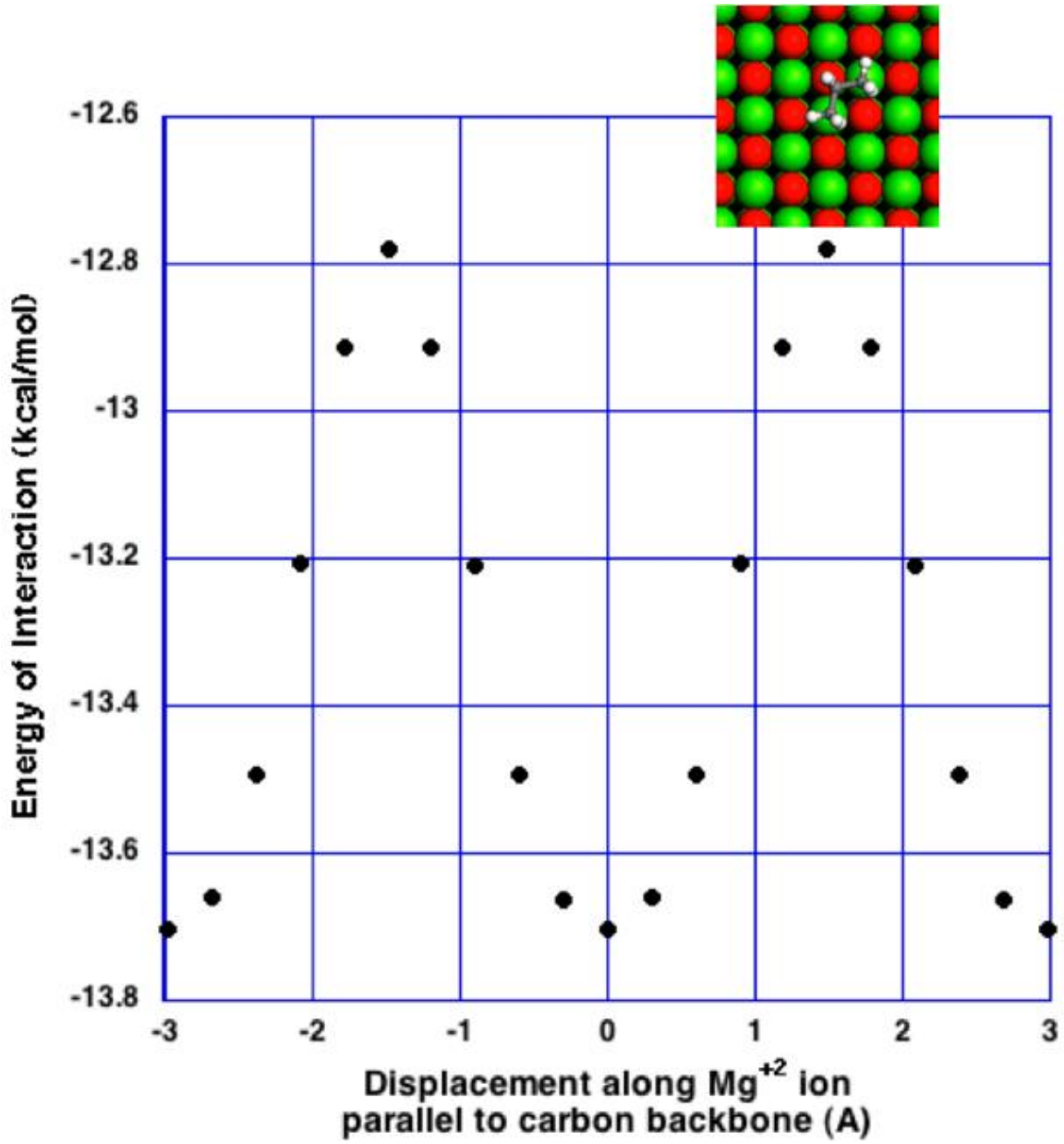


Figure 2-29 Energy as a function of displacement parallel to the carbon backbone.

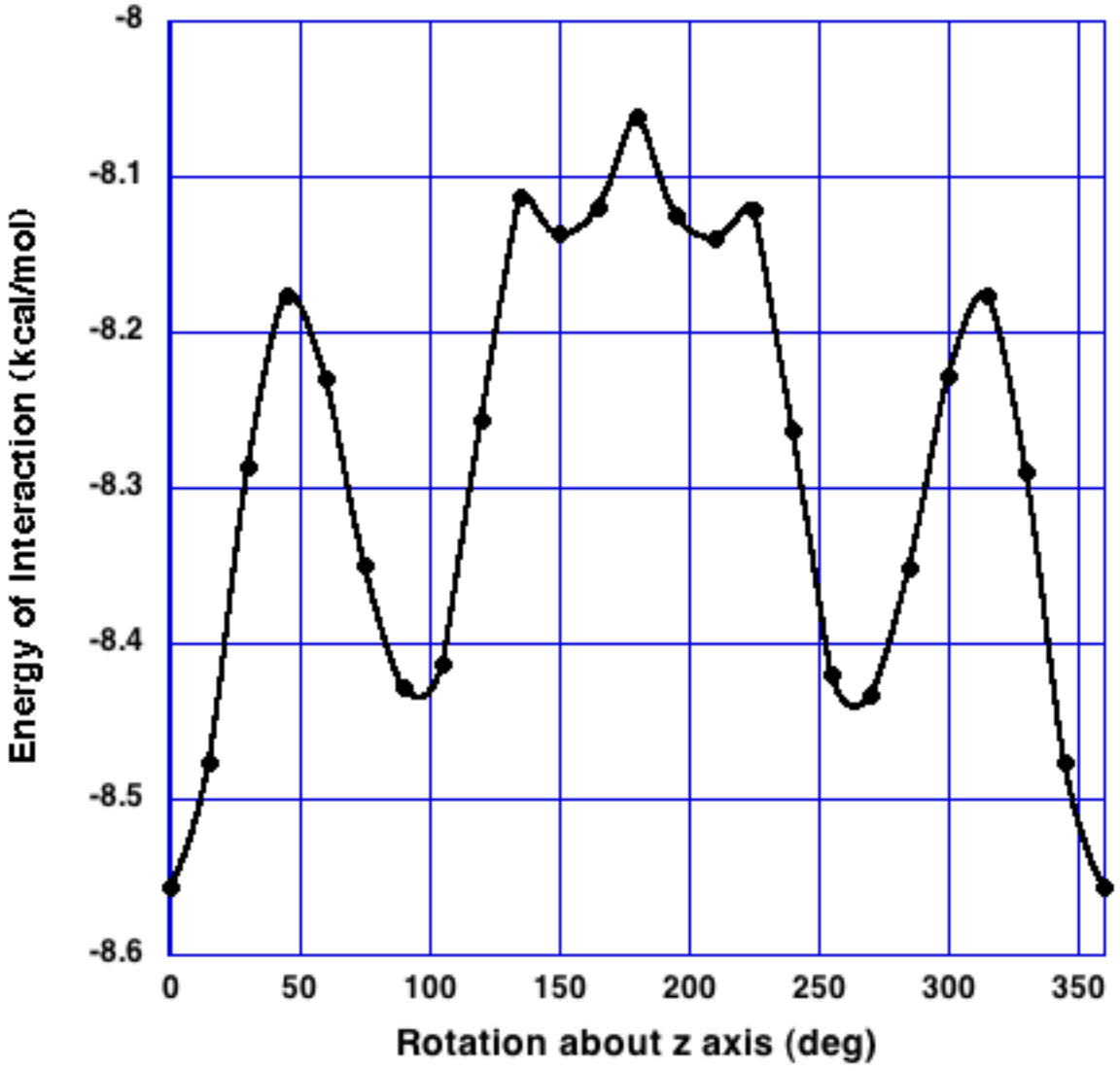


Figure 2-30 Rotation of propane about the z axis.

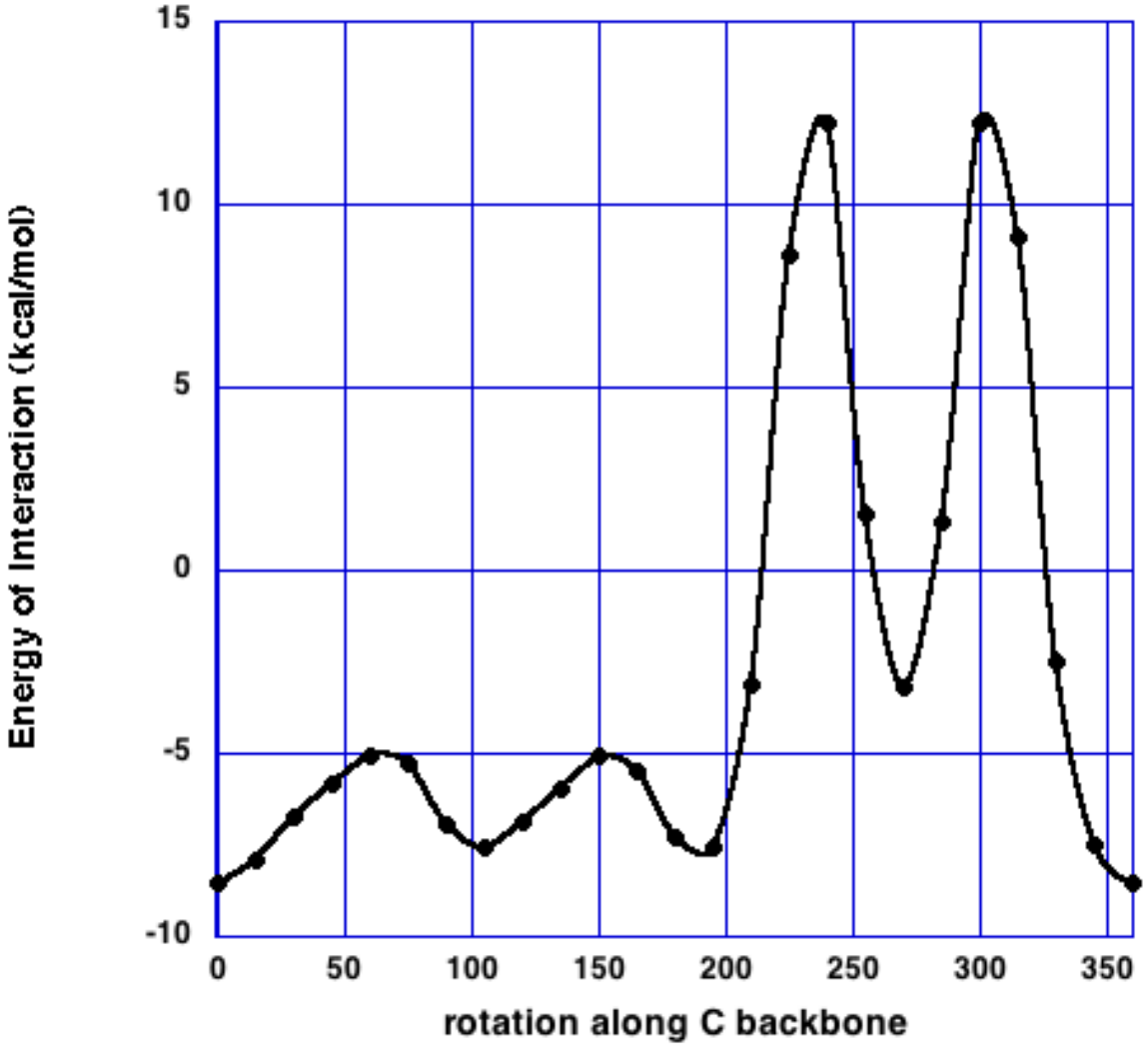


Figure 2-31 Rotation of Propane about the carbon backbone.

rotation around the carbon backbone does not show any symmetry, due to the hydrogen atoms bonded to the middle carbon. As the rotation passes 180°, these two hydrogens become closer to the magnesium ion that the propane is centered above, and dramatically increase the potential energy, as observed in Figure 2-31.

The previous curves show the amount of energy needed for a single propane molecule to propagate along the surface. In essence, it shows how the corrugation of the MgO (100) surface plays a role in the binding energy for propane. The maximum values in the graphs correspond to an energy barrier that the molecule needs to overcome to traverse the surface. As shown in Figure 2-29, the most probable translation of the propane molecule is along the Mg^{+2} ions with the molecule navigating in the direction parallel to its carbon backbone. For the propane molecule to negotiate this route on the surface, it would need to overcome an energy of 0.923 kcal/mol (40.0 meV). The maximum barriers that need to be overcome in the other directions are 1.94 kcal/mol (84.1 meV) for moving along the Mg^{+2} ions perpendicular to the carbon backbone (see Figure 2-28) and 1.35 kcal/mol (58.5 meV) for moving the propane molecule across the bridge sites (see Figure 2-27). As for the rotation of the molecule, a high energy barrier of 3.61 kcal/mol (157 meV) has the potential of preventing the molecule from rotating with respect to the carbon backbone. However, only 0.493 kcal/mol (21.4 meV) of energy is needed to rotate the molecule along the z direction.

2.6 Conclusion

In this chapter, both an experimental study and a simple computer modeling study of the adsorption of propane on the magnesium oxide (100) surface were discussed. Through high-resolution adsorption isotherms, it was determined that up to three distinct layers of propane form on the surface depending on the temperature. Evidence of a third discrete layer of propane was not distinguishable above 150 K. Two adsorption steps were observed over the entire temperature range (130 – 190 K). From the adsorption data, the molecular area of a propane molecule was calculated to be 33 ± 5 Å by using the Point B method.

From the two dimensional compressibility, a possible phase transition was observed in the temperature range studied. The transition temperature determined by plotting the FWHM as a function of temperature for the first layer is within the range 162 – 166 K, yielding an experimental value of 164 ± 2 K. Fitting the second layer data shows a transition in the range of 158 – 163 K, giving an experimental transition temperature of 160.5 ± 2.5 K. There was insufficient data to calculate a phase transition temperature from third layer K_{2D} peaks. By using previous work of the alkanes adsorbed on MgO (100) as a guide, the type of phase transition is most likely from a liquid phase to a gas/hypercritical liquid phase (Arnold, Cook et al. 2006).

The simulation study using the Materials Studio modeling package made it possible to determine the final geometry of an isolated propane molecule on the MgO (100) surface. From this study, it was determined that propane most likely lies on its "side" with three hydrogen atoms toward the surface and its carbon backbone parallel to the direction of the magnesium ions. The molecule can be thought of as "hugging" a magnesium ion (see Figure 2-25). By plotting the change in energy as a function of the perpendicular distance from the propane molecule's center of mass to the surface, it was determined that propane's center of mass is 3.18 Å from the surface.

The corrugation of the MgO (100) surface was also investigated to see how it affects the diffusion of the propane molecule. The path of least resistance (with the lowest energy barrier) for the propane molecule was determined to coincide with the molecule moving along the magnesium ions in the direction parallel to the carbon backbone. The energy barrier against rotation was also calculated. It was determined that a large barrier is experienced for a rotation about the carbon backbone; however, rotating the molecule with respect to the z-axis had a much smaller barrier.

Chapter 3 **Anodizing Aluminum Oxide**

This chapter discusses the synthesis and characterization of porous aluminum oxide. A process termed anodization was used to make the aluminum oxide. Discovered about a hundred years ago, this technique is used extensively in industrial and engineering processes. The beginning of this chapter includes a brief history of anodization, followed by key background concepts, including the nature of pore growth, a brief description of the microscopy techniques used, and a discussion of adsorption and desorption curves. Finally, the experimental apparatus used and the corresponding results are presented.

3.1 History

As mentioned, anodization is used extensively in industrial processes. The main purpose of anodization is to coat a metal with an oxide layer. While there is a natural oxide layer on the surface of most metals, anodization increases the thickness of this layer and thereby provides an enhanced level of protection against destruction by the

environment. Another popular application involving anodization allows for absorption of dyes in the oxide layer. Furthermore, depending on the experimental conditions, anodization can have the same effect as polishing. This particular application is used to clean and polish metal surfaces, and has multiple safety applications. When anodizing in acidic conditions, the oxide layer produced is generally porous in nature. The resulting porous materials have the potential to be used as templates for the synthesis of nanowires, to study confinement, or for gas storage.

Anodization was first used on an industrial scale in 1923 to protect seaplane parts from corrosion. The Bengough-Stuart process was used, which has a complicated voltage cycle using chromic acid. Anodization in this process took place in a 3% chromic acid solution at approximately 40 °C. The voltage was raised by small steps from zero to 40 V in 15 minutes, then held constant for 35 minutes. The voltage was raised again to 50 V in 5 minutes, and maintained for an additional five minutes. The total operating time for this process equals one hour (Bovey 1943). In 1927, Gower and O'Brien patented a simpler method using sulfuric acid, which became the electrolyte of choice in commercial applications (Sheasby and Pinner 2001).

While exposure to air results in the formation of an oxide layer for many metals, aluminum is especially susceptible to the formation of an amorphous oxide layer. Generally, this layer is less than ~15 nm thick, depending on the purity of the aluminum and the type of aluminum alloy (Sheasby and Pinner 2001). While the experimental

details will be explained more thoroughly in a later section, controlled anodization is performed by inserting aluminum into an electrolytic solution and then passing a direct current between the aluminum and a cathode. The aluminum serves as the anode (positive electrode), while the cathode (negative electrode) is often a platinum plate. As a prerequisite to intentionally forming a porous aluminum structure, the electrolytic solution must be acidic. Some popular solutions consist of chromic acid, sulfuric acid, phosphoric acid, and oxalic acid. The voltage (and subsequent current) needed for the anodization process depends upon the electrolytic solution used. Generally, the voltage varies between one and three hundred volts, commonly ranging between fifteen and thirty volts. The pores created in the anodized aluminum materials prepared in this study range from ten to greater than one hundred nanometers in diameter, as controlled by the experimental conditions. These conditions include the type of electrolytic solution used, the temperature of the electrolytic solution, electrolyte concentration, and the voltage between the anode and cathode. Besides aluminum, anodization characteristics of titanium, magnesium, zinc, niobium, and tantalum have also been investigated (Sheasby and Pinner 2001).

3.2 Background

For quite some time, anodization of aluminum has been known throughout industry and the scientific community (Bovey 1943; Keller, Hunter et al. 1953; Chu and Ruckenstein 1976). Very recent studies have been aimed at using the porous nature of

the oxide film for applications in the aerospace, nanoscience, and electronic industries. Depending on the exact experimental conditions, most notably the electrolyte, the nature of the oxide film formed on the metal surface can be adjusted and manipulated. One popular application involves using porous aluminum oxide film as a template for synthesizing numerous types of nanowires (Chi, Yao et al. 2002; Ohgai, Gravier et al. 2005; Gapin, Ye et al. 2006).

A nonporous barrier film forms when the electrolyte solution does not exhibit solvent action. To create a porous film, the electrolyte must be capable of dissolving the oxide layer. Porous films are created in various acidic media; with oxalic acid, sulfuric acid, and phosphoric acid being the most popular electrolytes. The size and nature (topology) of the pores created is a direct function of the experimental conditions employed, including the type of electrolyte used, the temperature of the electrolytic cell, and the voltage or current applied across (or passed through) the anode and cathode.

The microscopic mechanism of anodic oxidation and pore formation is a complex process that is not completely understood, although there are groups currently working on this problem (Verwey 1935; Keller, Hunter et al. 1953; Hoar and Mott 1959; Bandyopadhyay, Miller et al. 1996; Li, Zhang et al. 1998). The study done by Li in 1998, proposed the following mechanism to explain the formation of pores in anodized aluminum oxide:

1) Ions form at the metal/oxide interface and migrate into the oxide layer,

$$Al_{(s)} \rightarrow Al^{3+}_{oxide} + 3e^{-}.$$

2) At the oxide/electrolyte interface the water-splitting reaction occurs,

$$H_2O_{(l)} \rightarrow 2\,H^{+}_{(aq)} + O^{2-}_{oxide}.$$

Due to the electric field, the oxide ions formed from this reaction migrate within the oxide layer, from the oxide/solution interface toward the metal/oxide interface, to form Al_2O_3.

3) Simultaneously, the protons can locally dissolve the oxide, or migrate toward the cathode forming hydrogen gas and therefore complete the electrolysis cell:

$$Al_2O_{3(s)} + 6\,H^{+}_{(aq)} \rightarrow 2\,Al^{3+}_{(aq)} + 3\,H_2O_{(l)},$$

$$3\,H^{+}_{(aq)} + 3\,e^{-} \rightarrow \frac{3}{2}\,H_{2(g)}.$$

While this description attempts to describe the chemical activity, the anodized films often possess pore structures in the form of regular hexagonal arrays. To rationalize the hexagonal pore structure, Keller, Hunter, and Robinson theoretically derived the basic close-packed structure by considering a simultaneous dissolution of and formation of the oxide layer. Their explanation first considers a unit cell that begins to

dissolve at a single point, creating a point defect in the surface layer. At this point in the lattice, the thickness of the oxide layer is reduced, resulting in an increase in current at this spot. Consequently, the temperature of the electrolyte in this location increases, which results in a more rapid local dissolution of the oxide. Hence, a pore is formed (Keller, Hunter et al. 1953).

As the current continues to flow through the single pore, an oxide cell will form based on the electric field lines. Since the electric field lines are constricted by the pore (passing perpendicularly through the pore wall, but then curving to travel roughly parallel to the axis of the pore), the oxide layer that forms will be cylindrical in nature, having a roughly hemispherical end, and a central "test tube shaped" pore. Now consider the formation of adjacent cylinders; it is obvious that a pillar of metal will still be present between the oxide cylinders as they are forming. Since experiment shows a continuous layer of oxide, this pillar of metal must be converted to oxide anodically. The current passing through the three adjacent cylinders easily accomplishes this. The result is a continuous oxide layer with the cells forming a close-packed array (Keller, Hunter et al. 1953).

Details of the synthetic procedure are discussed in the following section. Briefly, the pure aluminum is subjected to a pretreatment of ultrasonication in water and ethanol. The cleaned aluminum is then anodized in an acidic medium. Next, the sample is submerged in a phosphoric/chromic acid bath to remove the oxide layer that was formed.

This results in a sample that has a textured concave surface. The sample is then anodized a second time, producing a symmetrical distribution of pores that exhibit a uniform, hexagonally close-packed structure.

We now discuss the techniques used to characterize our anodized aluminum materials. Scanning Electron Microscopy (SEM) is one of the techniques used to investigate the anodized aluminum oxide films. Many review articles exist giving a general overview and history of SEM, and illustrate its usefulness as a tool in materials science and biology (Murat 1975; Peters 1981; Oatley 1982; Seiler 1983; Oatley, McMullan et al. 1985; Cooke 1996; Hawkes 1997; Joy 1997; Newbury and Williams 2000; McMullan 2004). The following will be a brief introduction to SEM.

SEM utilizes electrons rather than light. It uses a high-energy beam of electrons to image a sample in a raster-like fashion. Depending on the available detectors and the design of the instrument, an SEM can produce images based on secondary electrons, back scattered electrons, characteristic x-rays, specimen current, and transmitted electrons. The first work in developing the theory and experiment behind SEM was done by Max Knoll in 1935 (Knoll 1935). In the 1940s, C. W. Oatley and his students developed it to its present form. Since then, SEM has been an exceptional tool in surface imaging and realizing the topography of numerous materials.

The design of an SEM is based on the premise that a metallic filament produces a beam of electrons that follows a vertical path through the column of the microscope as displayed in Figure 3-1 (University 2006). The electrons make their way through a series of electromagnetic lenses that condense and focus the beam, and the focused beam is directed at the sample. Once the beam strikes the sample, backscattered or secondary electrons are produced; ejected electrons are collected by detectors, and converted into a signal. The signal is sent to a viewing screen, producing an image. The magnification of an SEM ranges from 25 to 250,000 times.

Atomic Force Micrcoscopy (AFM) is another imaging technique used to study anodized aluminum oxide. Unlike SEM, an AFM system images the surface by "feeling" it with a cantilever. There are many review articles and textbooks discussing the basics and history of AFM (Frommer 1992; Jahanmir, Haggar et al. 1992; Louder and Parkinson 1994; Derose and Leblanc 1995; Cooke 1998; Friedbacher and Fuchs 1999; Wiesendanger 1999; Dedkov 2000; Ho 2002; Jalili and Laxminarayana 2004; Yeung and Yao 2004; Butt, Berger et al. 2007; Bonaccurso, Kappl et al. 2008). The following will be a brief overview of the technique as it is used in this study.

In 1986, the Nobel committee awarded half of the Physics prize to Gerd Binnig and Heinrich Rohrer "for their design of the scanning tunneling microscope." This was the precursor to the AFM, which was invented by Gerd Binnig, Calvin Quate, and Christoph Gerber in the same year. The AFM uses a cantilever with a sharp tip or probe

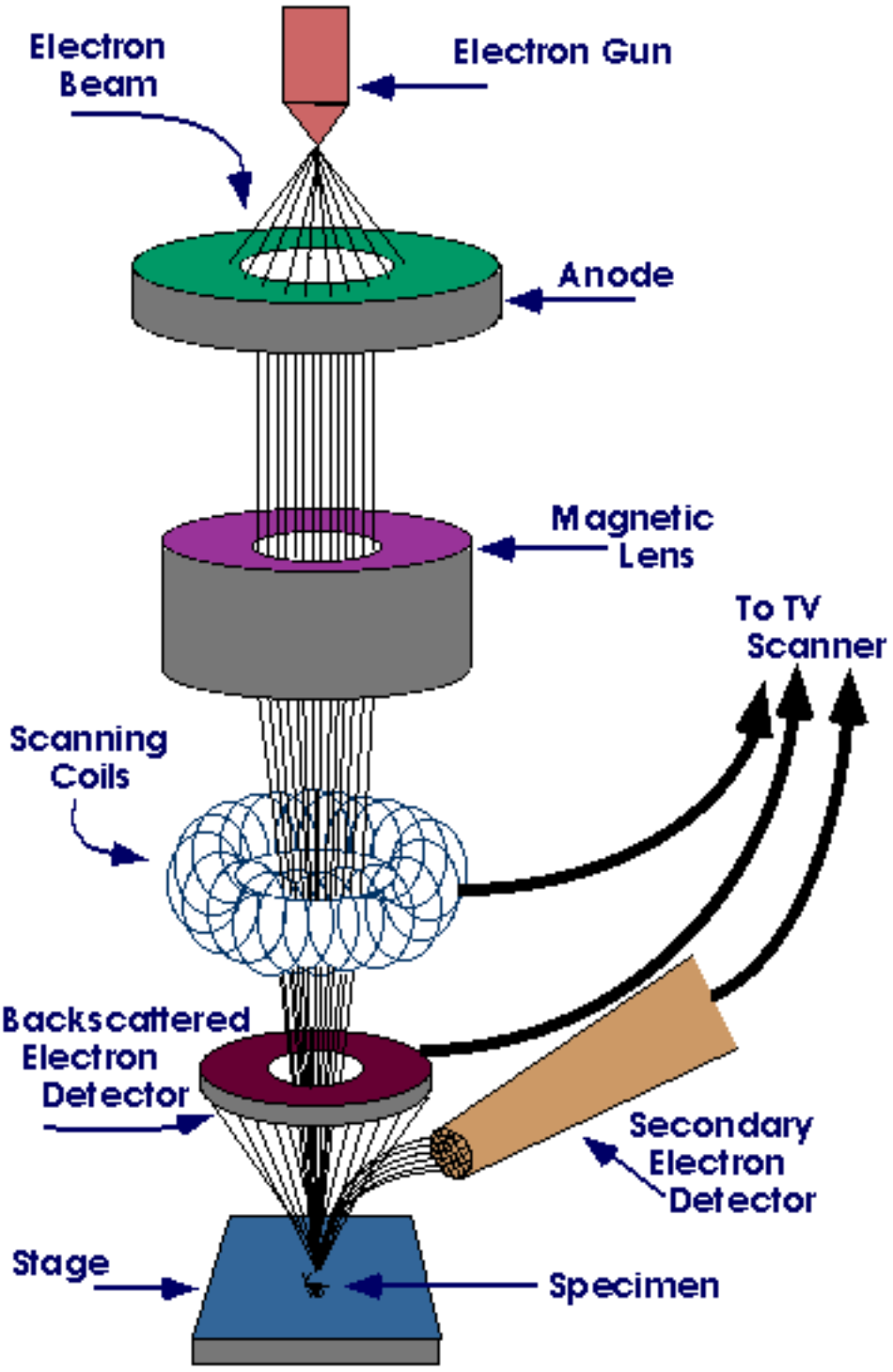


Figure 3-1 Path of the electron beam in an SEM column.

to scan the surface of the material of interest (2008).

The basic premise behind the AFM is measuring the force between the tip of the cantilever and the surface. As the tip is brought close to the surface, the forces between the tip and the surface cause a deflection in the cantilever. This deflection is measured using the deflection of a laser beam reflected off the top of the cantilever onto a photodiode detector. During a scan, the sample is moved under the cantilever arm by an x-y-z piezoelectric platform, and deflection of the laser is held constant by moving the platform in the z direction. Movement of the platform in the z direction maintains a constant force between the tip and sample, and keeps the tip from crashing into the surface under investigation.

The AFM may be operated in either contact mode or tapping mode. For this study, the AFM was operated primarily in tapping mode. In tapping mode, the cantilever is driven by a piezoelectric element to oscillate near its resonance frequency. Due to the various forces acting on the cantilever, the amplitude of oscillation decreases when the tip approaches the surface. By adjusting the height of the cantilever in relation to the surface so that the oscillation is constant, a topography of the surface can be mapped.

One of the main advantages that AFM has over SEM, is that AFM is able to provide a true three-dimensional surface profile. SEM can only provide a two-dimensional projection of the surface, but AFM is able to give a depth profile as well, by

mechanically dragging/tapping a tip over the surface. Other general advantages of AFM over SEM are the ease in sample preparation and lack of a vacuum environment. While AFM has much greater resolution than SEM, the correspondingly small field of view could be a disadvantage for some applications. SEM produces images on the order of square millimeters, while AFM images are on the order of square microns. Another disadvantage is the speed of the scan; with SEM, the image is captured in almost real time, while a typical image capture by AFM can take a few minutes.

The third method used to characterize the pore size of the anodized aluminum oxide membranes is adsorption/desorption isotherms. As mentioned in Section 2.1, porous materials will exhibit some hysteresis due to capillary condensation. In general terms, hysteresis is the failure of a dependent variable to retrace its values from the forward process when the direction of the independent variable is reversed (see Type IV and V isotherms in Figure 2-4). When hysteresis was first observed in adsorption/desorption isotherms, it took many years of detailed investigations before it was considered not to be an experimental artifact. It was initially believed that the hysteresis was due to either impurities in the substrate, failure to allow for equilibration, or some other experimental error. Hysteresis was finally explained theoretically by capillary condensation and other accompanying theories (Flood 1967).

The Kelvin equation serves as the quantitative basis for describing the hysteresis phenomenon of capillary condensation, and an overview of this equation is necessary for

a discussion of capillary condensation theory. The Kelvin equation relates the vapor pressure over a curved meniscus (in this case a droplet formed due to condensation in a pore), to the surface tension and curvature of the meniscus. The Kelvin equation is defined as

$$\ln\left(\frac{P}{P^0}\right) = -\frac{2\gamma\cos\theta}{(RT)r_m\Delta\rho}, \qquad 3.2.1$$

where γ is the surface tension of the condensed liquid, θ is the contact angle, r_m is the mean radius of the curvature of the liquid, and $\Delta\rho$ is the change in density between the orthobaric liquid and the bulk gas (Zsigmondy 1911). In the case of nitrogen adsorption/desorption at 77 K, Equation 3.2.1 simplifies to

$$r_k = \frac{4.15}{\log\left(\frac{P^0}{P}\right)}, \qquad 3.2.2$$

where r_k is the Kelvin radius. Since Equation 3.2.2 does not take into account the existence of an adsorbed multilayer film before pore condensation, the modified Kelvin equation for cylindrical pores can be used. It is defined as

$$\ln\left(\frac{P}{P^0}\right) = -\frac{2\gamma\cos\theta}{RT\,\Delta\rho\,(r_p - t_c)}. \qquad 3.2.3$$

Here r_p is the pore radius and t_c is the critical thickness of the adsorbed multilayer film (L.H. 1938). To obtain the pore size distribution, the adsorbed volume is plotted as a function of the radius and then the numerical first derivative is taken.

To discuss the microscopic mechanisms of hysteresis, one must consider the effects of pore size and shape on adsorption and desorption processes. Key concepts behind adsorption/desorption hysteresis are brought to light by the delayed meniscus and ink bottle theories, an overview of which are given here. First, consider that the surface of a porous adsorbent contains a network of pores into which adsorbate vapor diffuses. As layers of adsorbate build up on pore walls, the vapor pressure increases until the adsorbed material becomes more bulk-like; effects of surface tension are then important to the progress of condensation and evaporation in the pores. Delayed meniscus theory says that, for an open ended cylindrical pore, condensation within the pore or evaporation from the pore will not occur unless the local vapor pressure is such that formation or break down of the corresponding meniscus type is allowed according to the Kelvin equation given above. For open cylindrical pores of radius r, the vapor pressure for pore filling will correspond to twice the pore radius, since a cylindrical meniscus with radius of curvature 2*r is formed during condensation. However, once the pore is completely filled, a roughly hemispherical meniscus with radius of curvature equal to r is present at the pore mouth. Since evaporation must begin at the pore mouth, emptying of the pore will be delayed until the pressure drops below that corresponding to the pore radius, causing a hysteresis loop (Flood 1967; Thomas 1996).

Considering that many porous substrates are composed of a maze of interconnected, variously sized pores, it is easily recognized that a large amount of adsorbate could be contained in "ink bottle" structures, composed of one or more narrow

passages leading to a larger enclosure (similar to the shape of an ink bottle). Ink bottle theory postulates that adsorbate contained within "ink bottles" leads to significant hysteresis, as evaporation and desorption from these ink bottles undergo delayed meniscus effects. Similar effects are seen in closed cylindrical pores with a slight narrowing of the neck (Flood 1967; Thomas 1996).

Upon consideration of the above theories, it can be seen that the size, shape, and arrangement of channels in the porous adsorbent will greatly impact the adsorption/desorption hysteresis. Also important to note is that, for capillary condensation, the lower closure point of the adsorption/desorption hysteresis is largely determined by the adsorbate, not the adsorbent. The surface tension effects described by capillary condensation only occur once the adsorbed film becomes capable of sustaining a surface tension, so this type of hysteresis is generally not seen when the number of moles adsorbed is less than that needed for a monolayer. Likewise, there is some minimum pore size for which hysteresis will occur, as the pore must be large enough to accommodate cylindrical meniscus formation (Flood 1967; Thomas 1996).

Four common types of hysteresis are displayed in Figure 3-2. The Type A loop can be attributed, by the mechanisms described above, to either ink-bottle shaped pores or long, open capillaries with any of a range of cross sectional shapes (Thomas 1996). To produce a Type A loop, the pores should be fairly homogenous in size. A relatively steep rise in the adsorption curve occurs at the relative pressure corresponding by the Kelvin

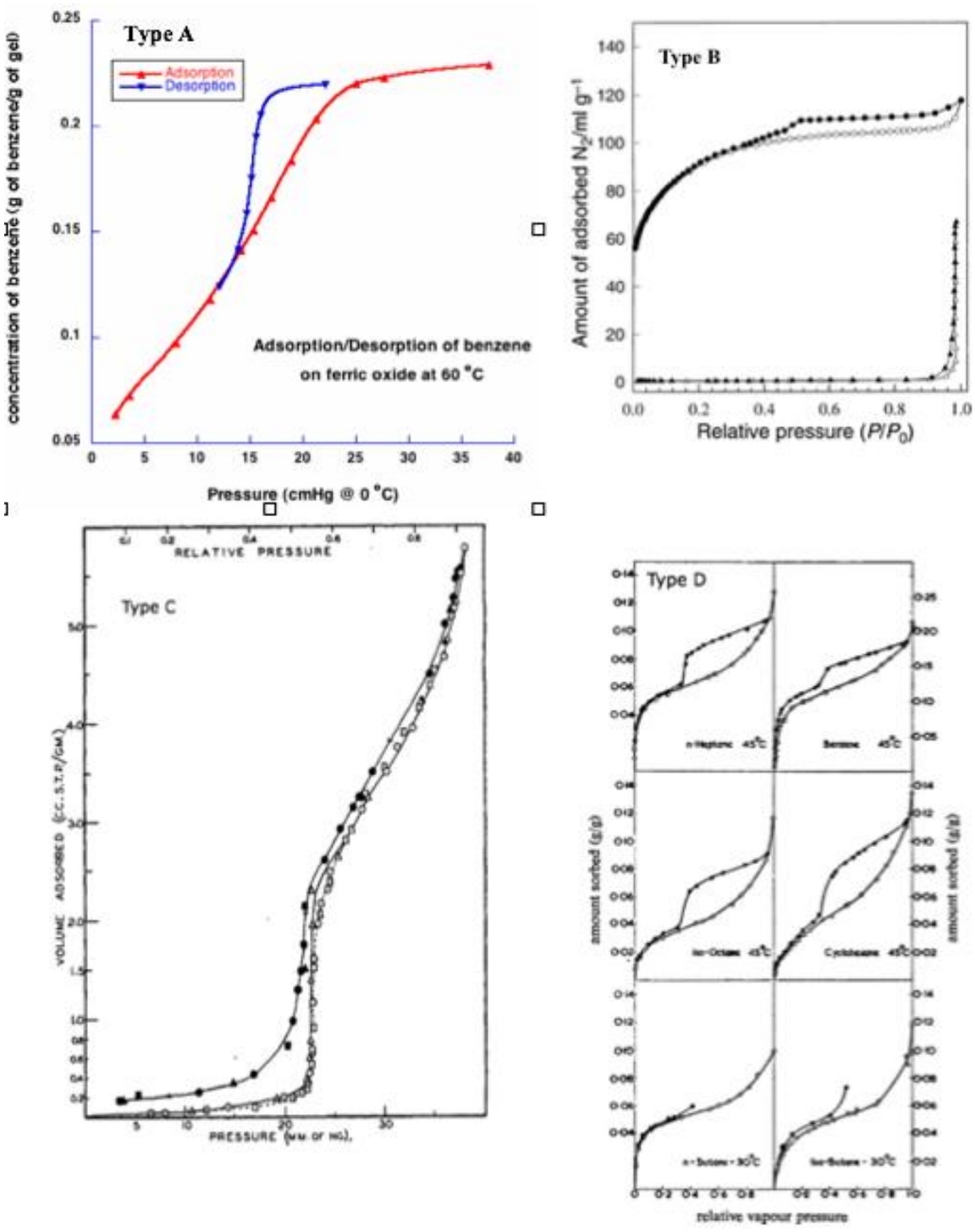


Figure 3-2 The four types of hysteresis loops.

equation to the radius of the ink bottle *body*. At this pressure, rapid filling of the pores occur. The Kelvin equation dictates that evaporation from the pore will be delayed until the vapor pressure is lowered to correspond with the radius of the pore *neck*. Emptying of the bottles happens quickly and the desorption curve falls sharply, forming a relatively tall and narrow hysteresis loop over an intermediate pressure range (Flood 1967; Thomas 1996). The experimental study depicted as Type A in Figure 3-2 is benzene on a ferric oxide gel (Lambert and Clark 1929).

The loop shown in Type B could be caused by narrow, slit-shaped cavities with parallel walls or to ink bottles with a large body radius. Meniscus formation and pore filling is delayed to near the saturated vapor pressure because of the large slit length (or large bottle radius), causing a steep rise as p/p^0 approaches one. Emptying occurs at much lower pressure, corresponding to the small slit width (or small neck radius) (Thomas 1996). The curve representing Type B in Figure 3-2 shows the nitrogen adsorption-desorption isotherms of layered cesium titanate (triangles) and TiO_2-pillared layered titanate (circles) (Choy, Lee et al. 2001).

Ammonia on carbon black typifies a Type C hysteresis loop (Holmes and Beebe 1957). This type of hysteresis could be caused by a heterogeneous assortment of ink bottles with a range of body and neck radii, or long, open pores in a range of sizes (Thomas 1996). Because the pores have a wide range of body radii, the pores will begin to fill over a wide range of vapor pressures, and the adsorption curve will be relatively

gently sloped. Since the pores have a wide range of neck radii, emptying also occurs over a wide range of vapor pressures, and the desorption curve is relatively gently sloped. Generally, the vertical separation between the adsorption and desorption curves is smaller for Type C, as compared with Types A or B, but the loop extends over a wider pressure range (with the hysteresis sometimes covering the entire pressure range) (Flood 1967; Thomas 1996).

The final type, Type D, is represented by various hydrocarbons adsorbed on methylammonium montmorillonite (Holmes and Beebe 1957). Type D hysteresis could be caused by ink bottles with roughly the same sized small-radius necks, but a variety of body radii (Thomas 1996). Type D loops combine features of Types B and C. Because the body radii are varied, the adsorption curve is gently sloped, as in Type C. Since the neck radii are roughly the same, the desorption curve falls sharply at the vapor pressure corresponding to the neck radius, as in Type B. However, the desorption curve does not reach the adsorption path, but drastically shifts and runs nearly parallel to it, rejoining it at zero pressure. This is attributed to a residual amount of adsorbate remaining trapped in the substrate. Flood reports that outgasing and "annealing" at high temperature is sometimes required before the original adsorption curve can be retraced. (Flood 1967)

3.3 Experimental Set-up

In this section, a detailed discussion of the route used to synthesize the anodized

aluminum oxide (AAO) is presented. This includes a description of the apparatus used to manufacture the samples, along with details of the two-step anodization process. Finally, the experimental parameters used in imaging and adsorption/desorption characterization are described.

3.3.1 Synthesis of Anodized Aluminum Oxide

The AAO membranes were synthesized using a two-step process. It has been shown that this two-step synthetic route produces homogenous, hexagonally oriented pores (Masuda, Yamada et al. 1997; Li, Muller et al. 1998; Li, Zhang et al. 1998). In the present studies, pure aluminum foil sheets, 0.25 mm thick, were obtained from Alfa Aesar (99.9995% purity). Before anodizing, the aluminum was cleaned by ultrasonication in deionized water, acetone, and ethanol for 15 minutes. While some researchers pretreat the aluminum by annealing and electropolishing, this did not seem to offer any advantage, except producing a shiny surface, and pretreating in this way did not affect pore growth.

The aluminum was placed in a specially designed Lexan holder (see Figure 3-3), along with a piece of pure platinum (Alfa Aesar 99.997% purity). By placing the metals in this holder, the distance between the anode (aluminum) and the cathode (platinum) could be set to a constant value (e.g at 13.8 mm in most cases). The holder was immersed in an electrolyte solution, which contained sulfuric acid and various other dioic

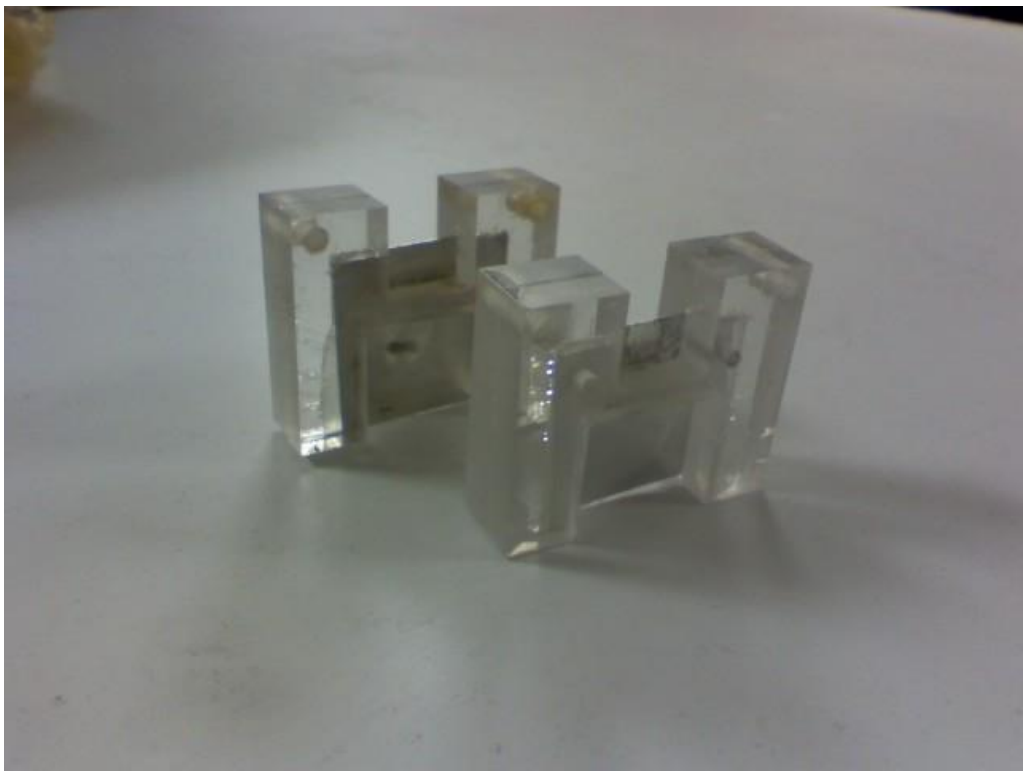


Figure 3-3 Anode and cathode mounted in Lexan holder.

acids. An Agilent E3612A DC Power Supply was used to set up the voltage difference between the anode and cathode; this model has a range of 0-60 V at 0-.5 A or 0-120 V at 0-.25 A. Throughout the experiments, the electrolytic solution was stirred with a homemade stirrer, consisting of a glass propeller attached to a glass rod and mounted on a variable speed DC motor. In addition, the temperature was held constant at 2.0 °C with a Thermo Electron Corporation Digital Plus refrigerated bath.

In the first anodization step, the aluminum was kept in the anodization bath for time intervals that varied between 2 and 48 hours. Upon completion of this step, the aluminum foil was rinsed with deionized water and submerged in a mixture of chromic acid (1.8% w/w) and phosphoric acid (6% w/w) for approximately 5 hours. The acid treatment dissolves off the layer of aluminum oxide that formed during the first anodization step. This procedure produces a dimpled surface on the underlying aluminum metal, and presumably helps to promote ordered pore growth during the second anodization step. Once the oxide layer is dissolved away chemically, the aluminum foil is anodized a second time in the same electrolytic solution as the first anodization step. All the parameters (voltage, temperature, stirring rate, acid concentration) during the second treatment are set identically to the first anodization step. When the second anodization step is completed, the AAO foil is removed from the electrolyte and rinsed a final time with deionized water. This results in an aluminum foil that is coated with a surface layer of porous aluminum oxide (thickness ranging from approximately 5 to 50 microns). The diameter of the pores in the oxide layer range from

less than 10 to 75 nm and form a hexagonal network. Figure 3-4 is a cartoon summary of each of the steps mentioned in the synthesis of the anodized aluminum oxide.

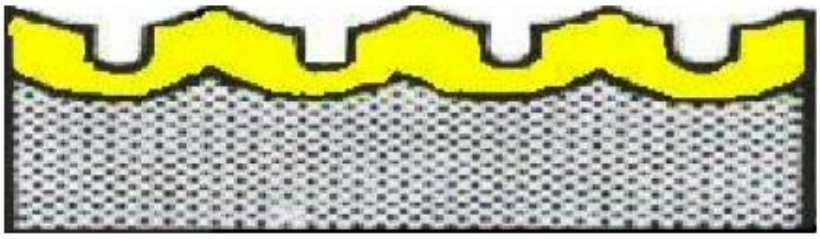
3.3.2 Characterization

To characterize the AAO films, scanning electon microscopy, atomic force microscopy, and adsorption/desorption isotherms were used. These techniques compliment each other by providing redundant quantitative measures of pore size and a qualitative appreciation of the topography of the surface and cross section of the sample.

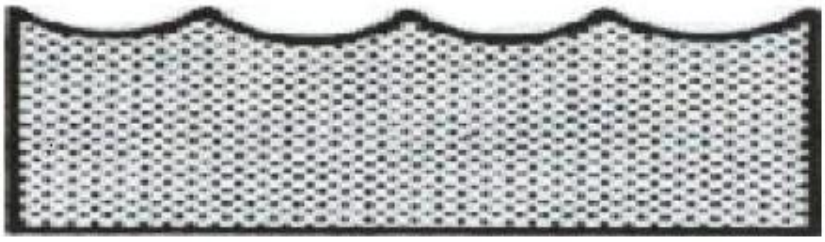
3.3.2.1 Scanning Electron Microscopy

A Hitachi S-4700 Scanning Electron Microscope[2] was used to characterize the pore size and distribution of the anodized aluminum oxide. Normally, nonconducting samples need to be coated with a conductor (e.g., gold, palladium, or carbon) to prevent charging during SEM; unfortunately, coating the sample reduces pore size, and it is hard to control the thickness of the coating. Charging is a problem encountered when imaging electrically insulating materials, whereby electrons become trapped on the surface of a nonconductive sample because it is insufficiently grounded. When there is charging on

[2] SEM work was done at the High Temperature and Materials Laboratory (HTML), and the Center of Nanophase Materals Sciences (CNMS) at Oak Ridge National Laboratory.



1st Anodization step: A thin film of porous aluminum oxide forms on the metal surface



Acid Treatment: The chromic/phosphoric acid mixture dissolves the porous membrane that leaves a textured surface.



2nd Anodization step: A hexagonally oriented porous structure forms

Figure 3-4 Summary of the synthetic steps to produce the anodized aluminum oxide.

the sample, it can be almost impossible to get a clear image from the SEM. To overcome charging on the AAO samples, the voltage of the electron beam was decreased and the working distance was brought from the normal 10 mm down to 3 mm. Making these two adjustments dramatically decreased the amount of charging on the sample and allowed imaging without a conductive coating.

3.3.2.2 Atomic Force Microscopy

A Digital Instruments Multimode AFM, manufactured by Veeco and controlled using a Nanoscope III electronic controller, was used in this study. The microscope has the capability of achieving atomic resolution using a Type A scanner. All images in this study were made with the Type A scanner in tapping mode. Tap300 tapping mode tips manufactured by Budget Sensors were used. They have a resonance frequency of 300 ± 100 kHz and a force constant of 40 N/m (with a range of 20-75 N/m).

3.3.2.3 Nitrogen Adsorption/Desorption Isotherm

Nitrogen adsorption/desorption isotherms were performed using the same type of apparatus as for the propane study (see Section 2.3.2 Gas Handling System). For each dataset, the adsorption isotherm was acquired first, then the LABVIEW program used to control the gas handling system was switched to desorption mode, and the desorption isotherm was collected. The pore size distribution was calculated using the modified Kelvin equation, Equation 3.2.3.

3.4 Results

Many experimental parameters can be varied in the synthesis of anodized aluminum oxide, including the type of acid used as the electrolyte, concentration of the acid, temperature of the acid bath, applied voltage, and anodization time. The first two parameters, type and concentration of acid, will be discussed further in this section. This section begins with the types of results obtained from the SEM and AFM work, along with a description of how the images were analyzed. This section will conclude with the results of the adsorption/desorption isotherm work.

3.4.1 Microscopy Results

More than fifty samples of anodized aluminum oxide were synthesized and imaged using SEM. The SEM images were analyzed using SIMAGIS by Smart Imaging Technologies. This software package has the ability to determine the size of individual pores, so that each detected pore can be included in the calculation of the statistical average pore size for the entire sample. The following procedures were employed when using SIMAGIS for data analysis:

1. The SEM image file was imported into SIMAGIS. Typically, TIFF or JPEG format was used.

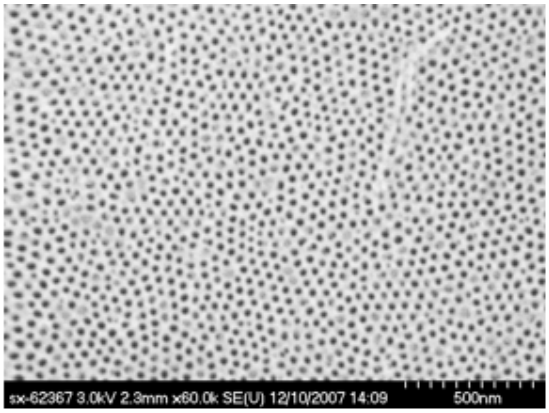
2. The scaling factor for each image was determined by measuring the pixels per nanometer for the reference scale included on the image.

3. A mask was made of the image that converts the image into a black and white picture, where white indicates the area of interest (in this case the pores).

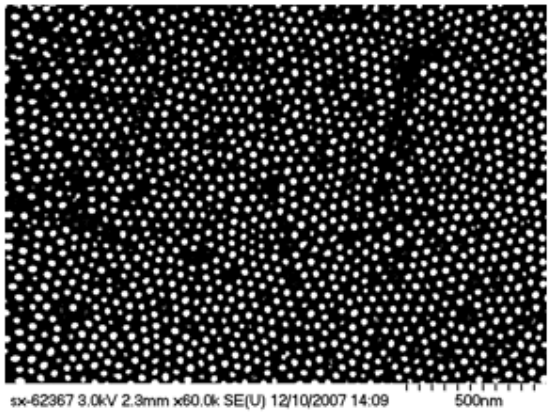
4. Each pore was then individually marked for analysis. For each pore, SIMAGIS determines 128 possible diameters and then returns the average of those values.

5. A table was made, listing the average diameter of every pore chosen in the mask. The data was imported into Excel, where a histogram was made of the pore diameters. Finally, this histogram data was imported into Kaliedagraph, where a Gaussian was fitted to the data and the mean pore diameter for the image was calculated. The standard deviation in pore size for the image was found from the Gaussian fit parameters.

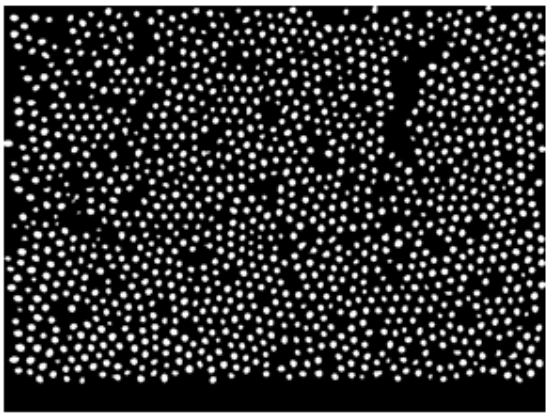
Figure 3-5 shows intermediate results for each of the steps followed in determining the average pore diameter for an image. A minimum of ten images were taken of each sample at various locations on the surface. The images were analyzed as



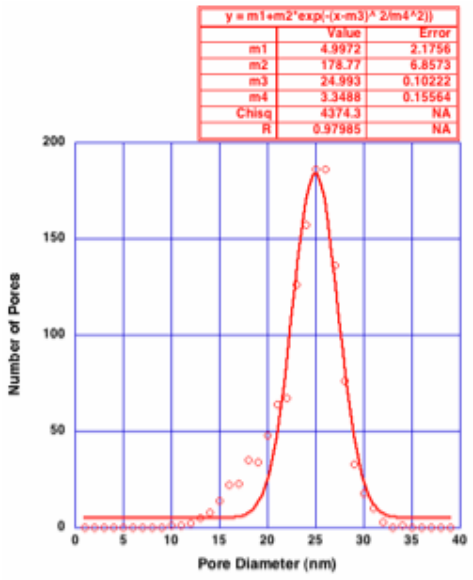
SEM Image



Mask



Selected Pores



Histogram with Gaussian fit

Figure 3-5 Steps involved in processing an SEM image.

described above to obtain an average pore diameter for each image. Then, data from all the images for a given sample were pooled to find the overall average pore size and standard deviation for the sample.

Figure 3-6 and Figure 3-7 show results of an image analysis done for a sample anodized in 0.5 M sulfuric acid at 20 V. Every sample of anodized aluminum oxide synthesized was imaged and analyzed in the same manner, and the images and results presented here are representative of that analysis. In Figure 3-6, the top left image shows a portion of the sample that formed a nonporous layer, and so this image was not used for pore size analysis. There are regions on every sample that exhibit the nonporous oxide, these locations typically occur where the aluminum is shielded by the Lexan holder or near the electrical connections. The other ten images shown in Figure 3-6 were analyzed using SIMAGIS according to the procedure outlined above. Figure 3-7 shows a summary histogram (top left), which cumulates all data for the sample (data from all ten images is included). The remaining histograms display the data for each of the ten separate images used in the analysis. For this sample, the average pore diameter was found to be 23.2 nm, with a standard deviation of 4.3 nm.

AFM images were also acquired for some of the AAO samples. Figure 3-8 shows an image obtained using tapping mode for a sample anodized in 0.78 M sulfuric acid at 5 V. This figure is representative of the AFM images obtained for the AAO samples synthesized. Analysis of the AFM images for the sample shown in Figure 3-8 reveal an

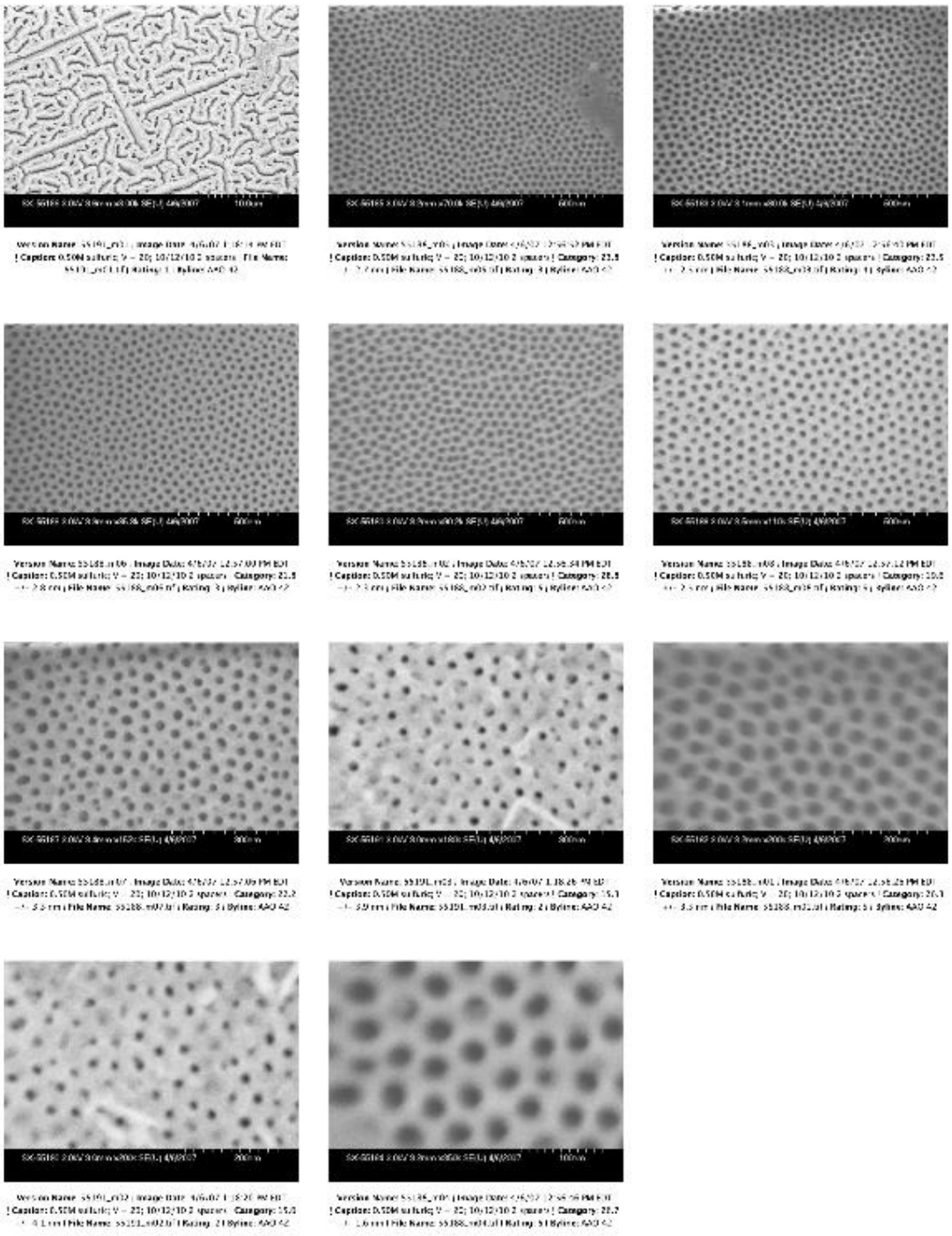


Figure 3-6 SEM images of a sample of anodized aluminum oxide.

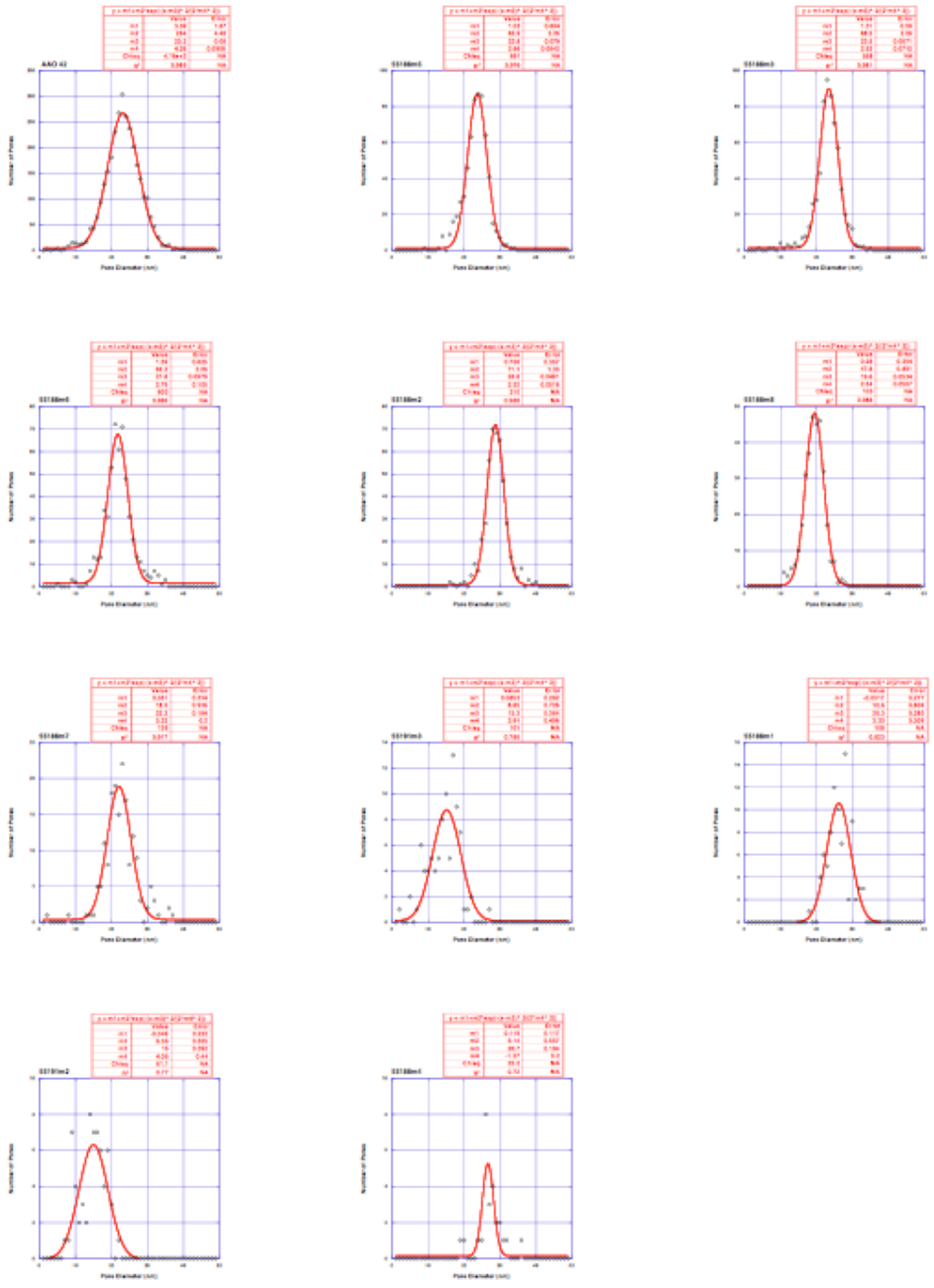


Figure 3-7 Pore distributions for the images in Figure 3-6.

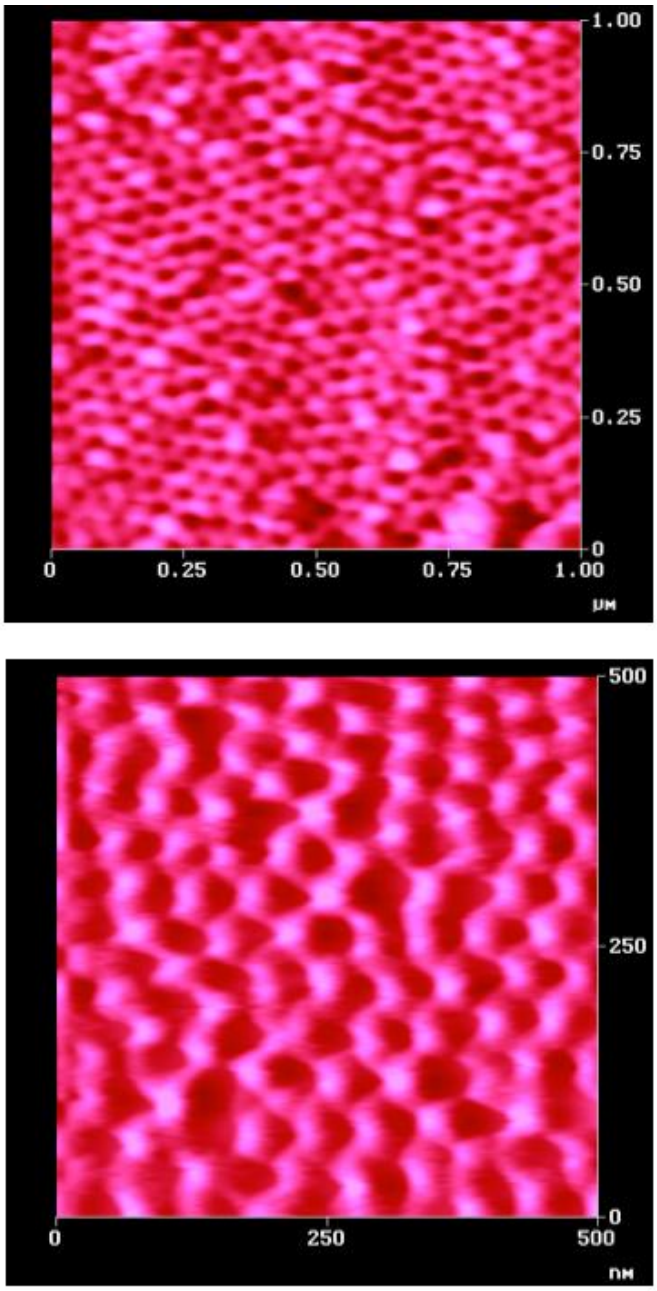


Figure 3-8 AFM image of a sample of anodized aluminum oxide.

average pore diameter of approximately 20 nm, in good agreement with the SEM results.

As discussed previously, one of the advantages of AFM is that three-dimensional topography can be obtained. Figure 3-9 shows a sectional analysis of an AFM image; the y-axis gives tip deflection, which corresponds to surface elevation, while the x-axis shows displacement along the straight line path in the lower image. The AFM image in Figure 3-9 shows a sample that was synthesized in a manner similar to the one in Figure 3-6 and Figure 3-7. The oscillation seen in the line profile indicates the locations of pores; the line profile does not, however, show the true depth of the pores, but is limited by the size of the tip. The actual pore depth is shown in the SEM images of Figure 3-10. As seen in the cross sectional images, the pores have lengths on the order of microns. It must be noted that the pores do not go all the way through the metal. This was determined using the SEM and Energy-dispersive X-ray spectroscopy (EDX). By using the EDX to probe successive locations along the cross sections of several samples (moving parallel to the pore axes), we know that a central layer of metal remains between the oxide layers covering the sample surface. In general, the synthesized templates exhibit pore depths ranging from 5 – 50 microns.

3.4.2 Types of Acid

The type of acid used as the electrolyte plays a critical role in the pore formation of the anodized aluminum oxide. As mentioned in the background, a competition

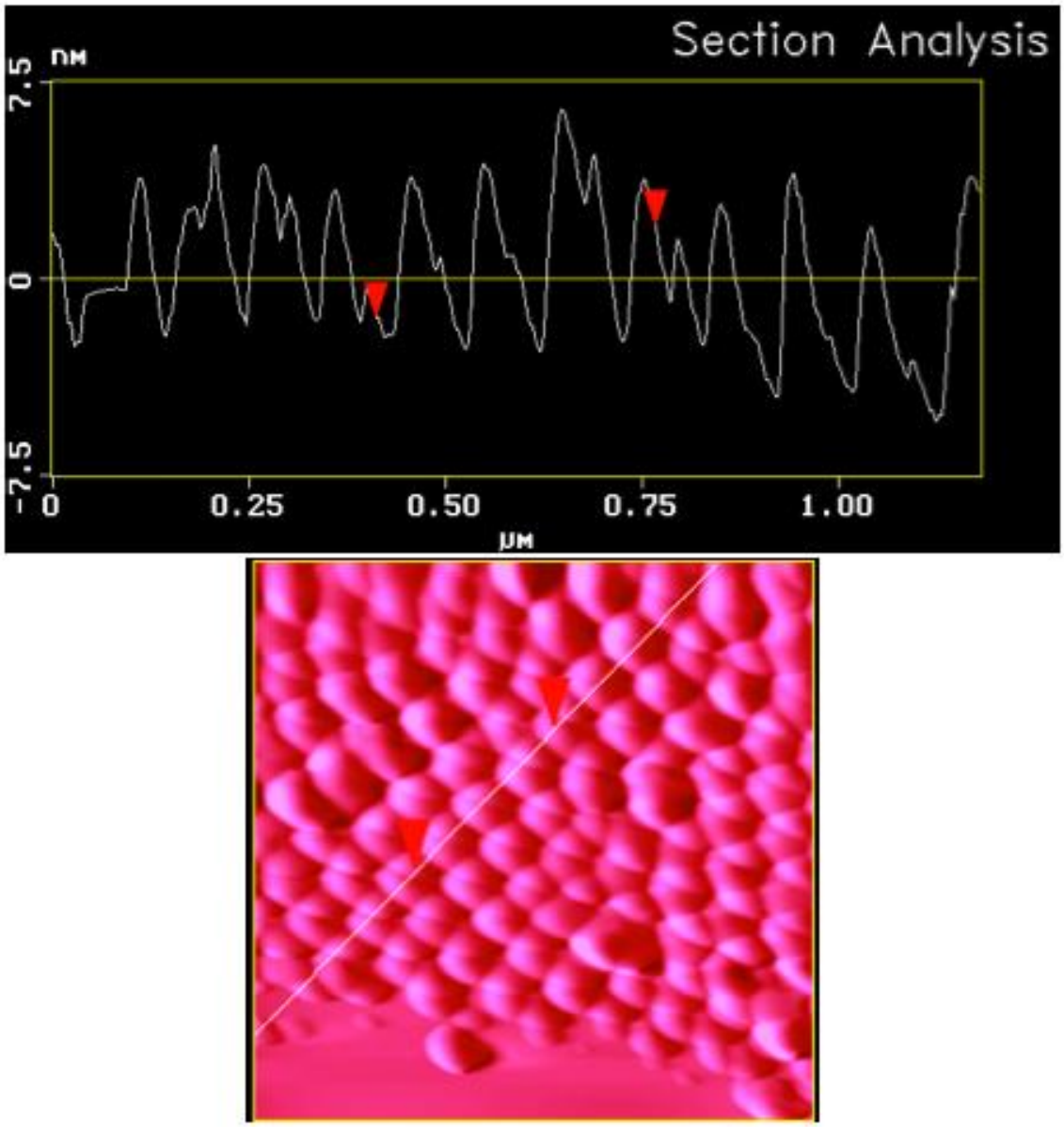


Figure 3-9 Depth analysis of an AFM image.

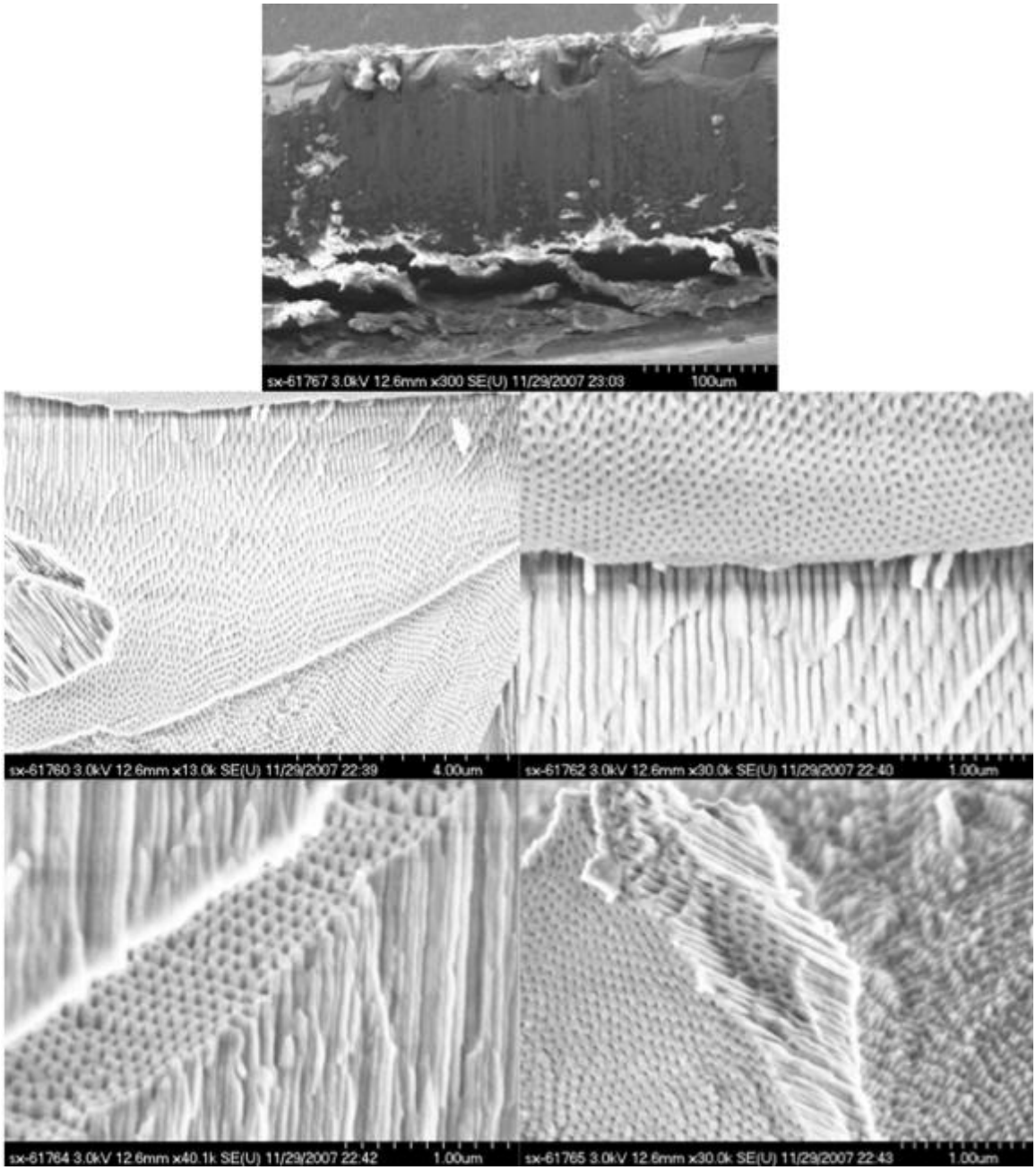
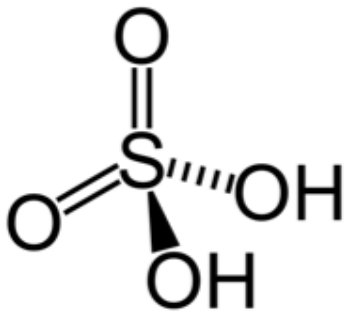


Figure 3-10 Cross sectional analysis of AAO.

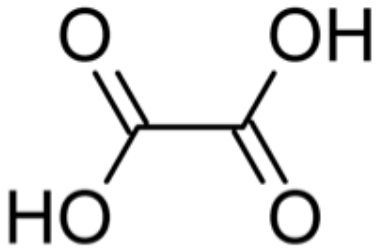
between the solvation and formation of the oxide layer exists; hence, the type of acid used is important. A balance between the dissolving power of the acid and the ability for the acid to promote pore formation must exist. The acid types compared in this study were sulfuric acid, oxalic acid, malonic acid, and succinic acid. The structures of each acid are depicted in Figure 3-11. Table 3.1 gives some basic information about each acid, including the molecular weight and the pK_a values for each proton that dissociates from each acid.

The following figures show SEM images obtained for samples synthesized in each acid. Figure 3-12 displays the images for a sample made in sulfuric acid. Figure 3-13, Figure 3-14, and Figure 3-15 show samples made in oxalic, malonic, and succinic acids, respectively. Figure 3-16 shows a representative image obtained for each acid for easy comparison. All the samples in this series were synthesized with first and second anodization times of ten hours, at a temperature of 2 °C.

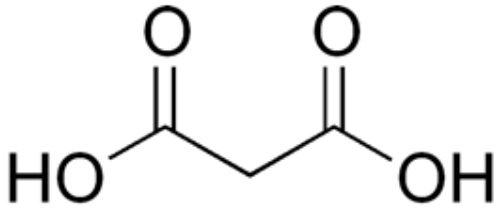
As can be seen in Figure 3-16, the sulfuric acid sample shows pores on the order of 10 nm in diameter. Given similar conditions, oxalic acid produces a pore size of approximately 60 nm. Samples made in both the sulfuric acid and oxalic acid formed fairly uniform, hexagonally oriented pores. The longer chain dioic acids, however, produces samples whose pores look like they are not fully formed. This could be due to a number of reasons. First, the acids might not be strong enough to sufficiently dissolve the oxide layer. Second, the large size of the anion in the acid could negatively effect the



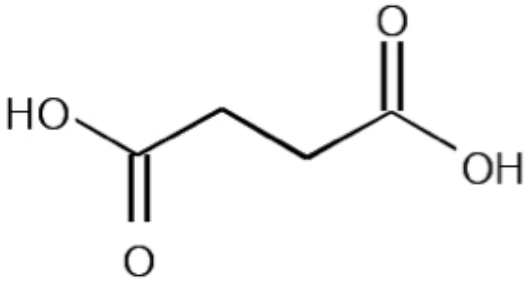
Sulfuric Acid



Oxalic Acid



Malonic Acid



Succinic Acid

Figure 3-11 The structure of the various acids used in the synthesis.

Table 3.1 Properties of the various acids used in the synthesis.

Type of Acid	pKa1	pKa2	Molecular Weight
Sulfuric acid	< 0	1.92	98.078
Oxalic acid	1.23	4.19	90.03
Malonic acid	2.83	5.63	104.03
Succinic acid	4.16	5.61	118.09

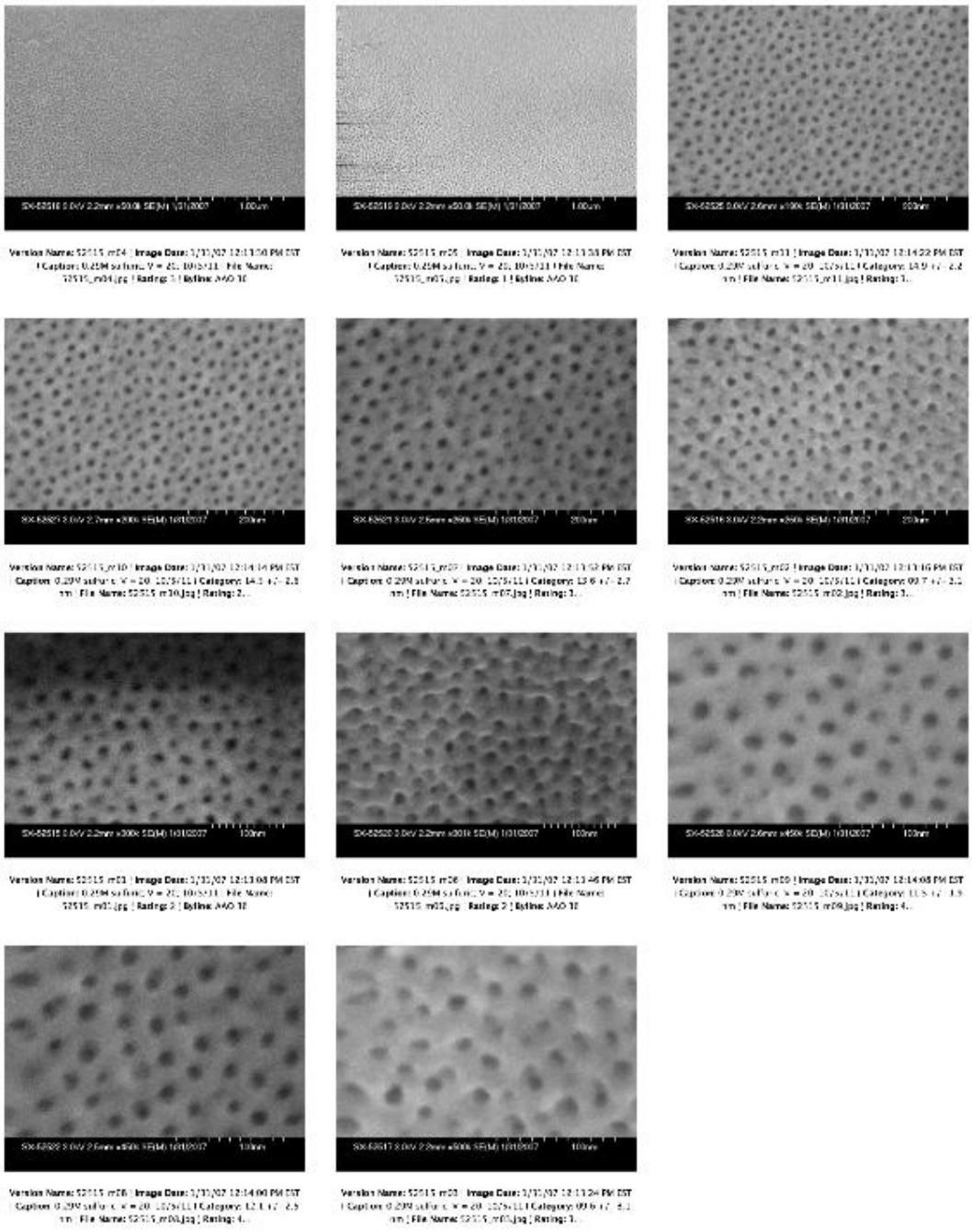
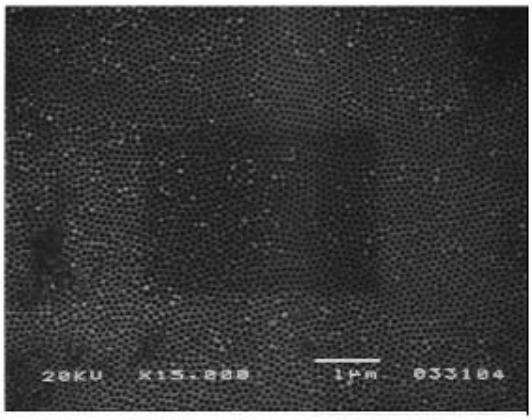
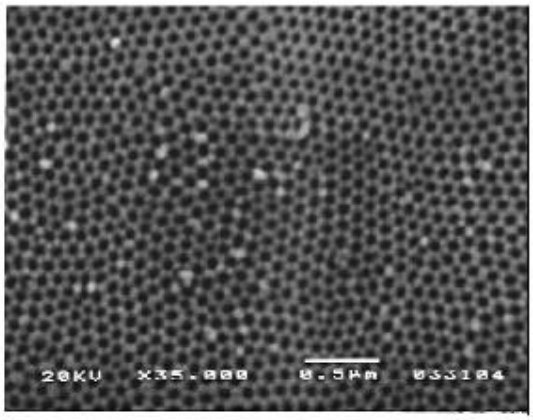


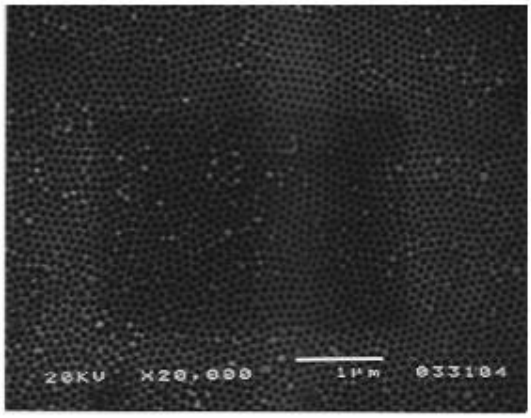
Figure 3-12 Anodized aluminum oxide synthesized in sulfuric acid.



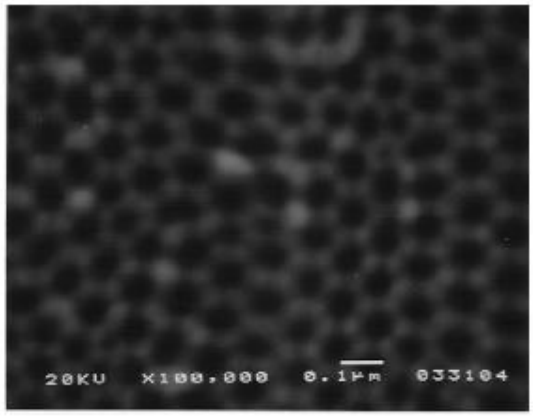
Version Name: AAO4 15000 | Image Date: 4/20/06 9:37:19 AM EDT | Caption: 0.3M oxalic; V = 40; 12/12/24 annealed 24hr under vacuum | Category: 61.2 +/- 8.1 nm



Version Name: AAO4 35000 | Image Date: 4/20/06 9:38:40 AM EDT | Caption: 0.3M oxalic; V = 40; 12/12/24 annealed 24hr under vacuum | Category: 63.9 +/- 5.8 nm



Version Name: AAO4 20000 | Image Date: 4/20/06 9:39:53 AM EDT | Caption: 0.3M oxalic; V = 40; 12/12/24 annealed 24hr under vacuum | Category: 59.8 +/- 7.4 nm



Version Name: AAO4 100000 | Image Date: 4/20/06 9:40:59 AM EDT | Caption: 0.3M oxalic; V = 40; 12/12/24 annealed 24hr under vacuum | Category: 66.4 +/- 8.1 nm

Figure 3-13 Anodized aluminum oxide synthesized in oxalic acid.

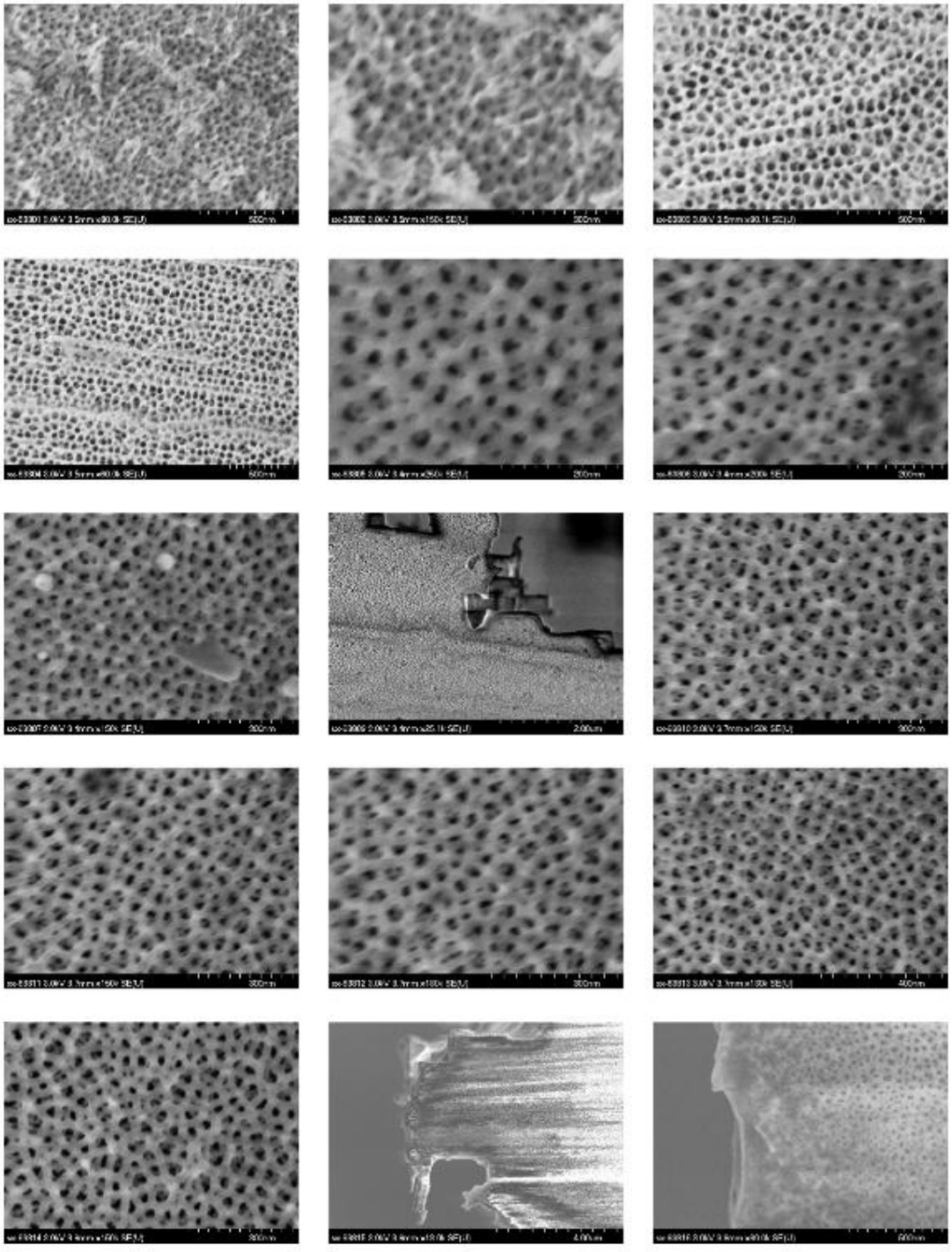


Figure 3-14 Anodized aluminum oxide synthesized in malonic acid.

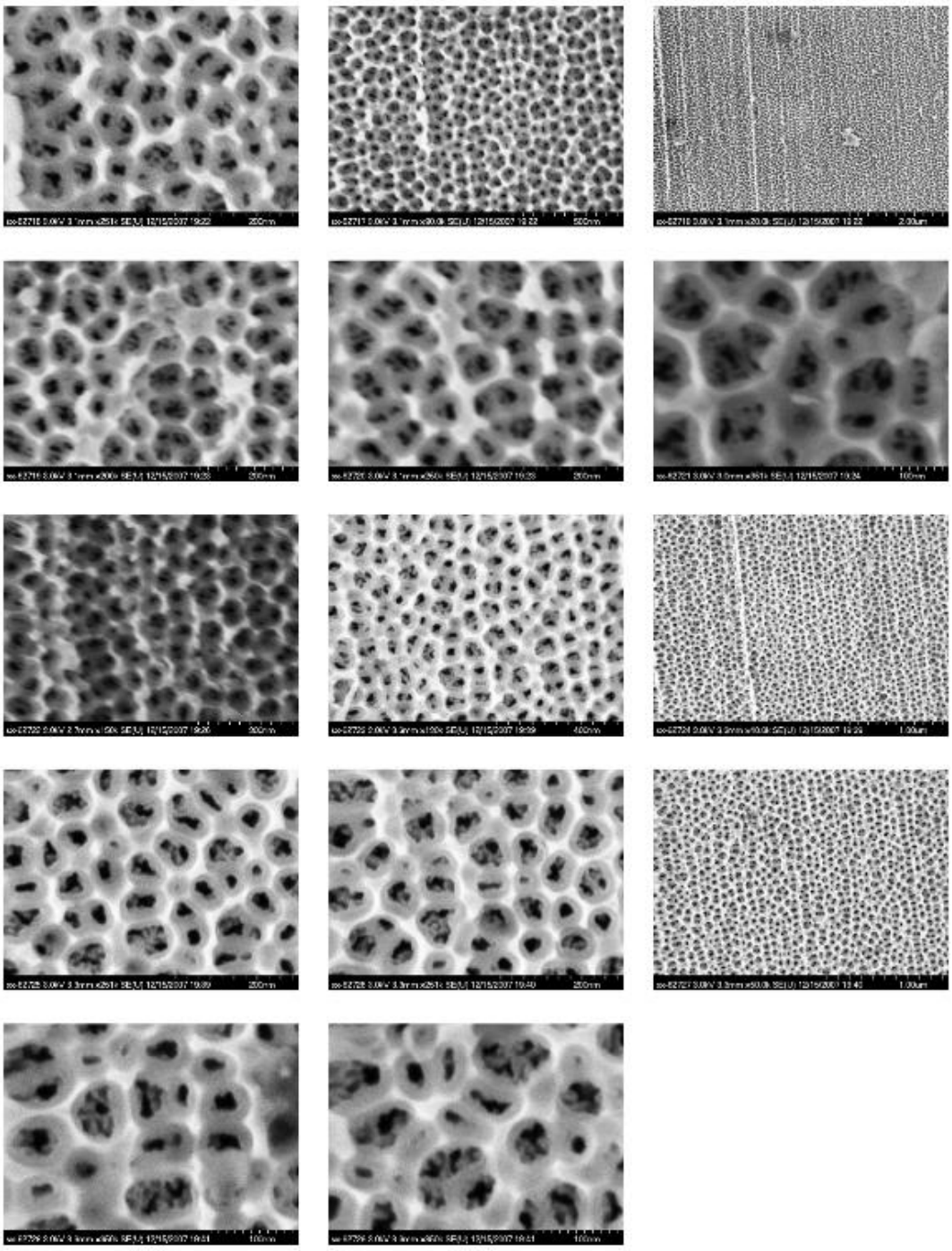
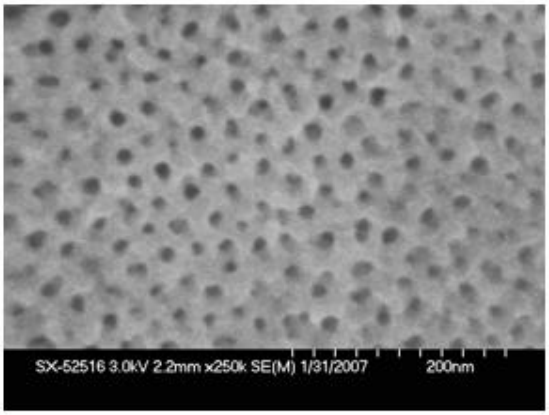
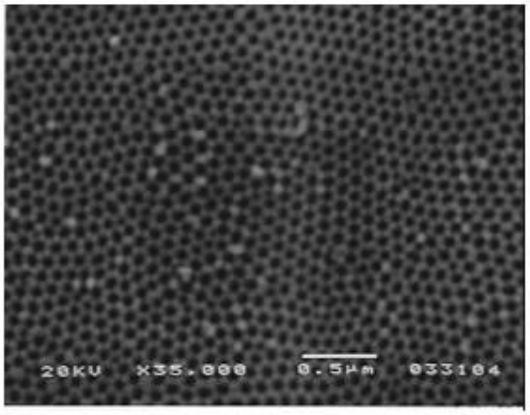


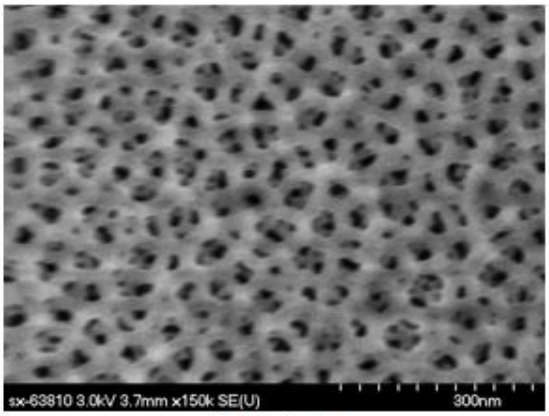
Figure 3-15 Anodized aluminum oxide synthesized in succinic acid.



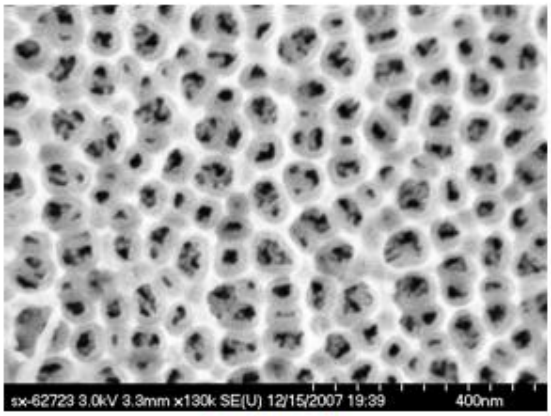
Sulfuric Acid



Oxalic Acid



Malonic Acid



Succinic Acid

Figure 3-16 Summary of all four acid types used in the synthesis.

pore formation; as the anion increases in size, the mobility of the acid through the pore becomes hindered. Finally, it could simply be that the voltage was not high enough or the time of anodization was not long enough to produce the hexagonally oriented pores.

3.4.3 Concentration of Acid

The larger motivation for trying to understand the synthesis of anodized aluminum oxide was to create a porous membrane with average pore diameters below ten nanometers. After examining preliminary results from the last section, sulfuric acid was chosen as the optimum electrolyte. The strength of the acid and its high viscosity make it an ideal electrolyte to promote pores that exhibit a small diameter. The strength of the acid is determined by the pK_a values, listed in Table 3.1. Sulfuric acid, like the other acids considered, is diprotic, with the first hydrogen dissociating readily. The second hydrogen also dissociates quickly, as compared with the other acids studied. The dissociated H^+ ions attack and dissolve the oxide layer, causing pore formation.

A series of samples were synthesized by varying the sulfuric acid concentration. The reaction time for the first and second anodization step was kept constant for the entire set of samples at 10 and 11 hours, respectively. The voltage applied between the anode and cathode was held constant at 20 V. The temperature was kept at 2 °C. Figure 3-17 shows a summary of the SEM image analysis results for this series of samples. As shown in the figure, the pore diameters decrease with decreasing acid concentration, and

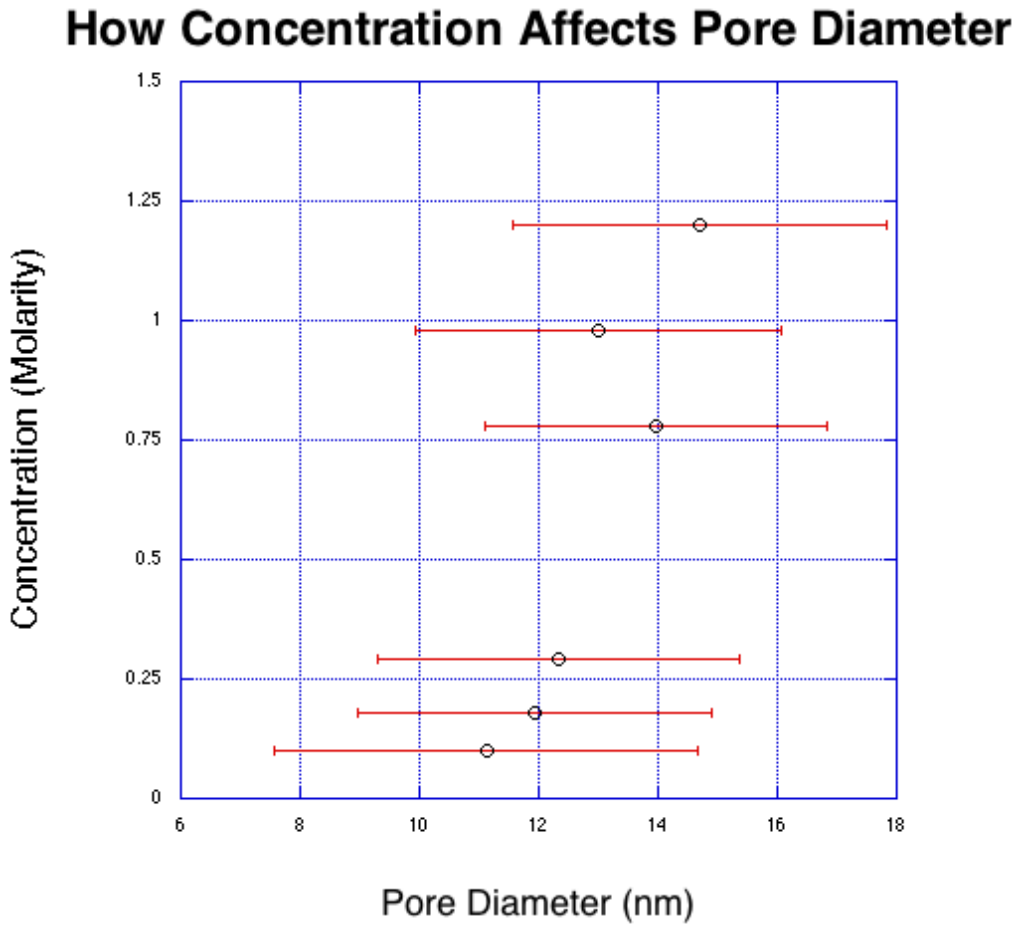


Figure 3-17 The effect of concentration on the pore diameter.

seem to approach a value of approximately ten nanometers. The error bars depicted on the graph are approximately ± 2-3 nm and represent ±1σ, the standard deviation obtained from the Gaussian fit of the SIMAGIS data.

3.4.4 Adsorption/Desorption

As a complement to the electron microscopy data, a nitrogen adsorption/ desorption isotherm was performed on eight AAO samples. Each sample was synthesized in 0.40 M sulfuric acid at 20 V. All eight samples were placed together in a sample cell similar to the one described in the propane study. The temperature was controlled using a Neocera LTC-21. The isotherm study was done at 77K. Prior to the study, the samples were heat treated under vacuum at 400 °C for approximately five hours, in order to remove any adsorbed water or solvent present in the pores. Figure 3-18 is a representative plot obtained from one of several identical adsorption/desorption isotherms performed on the same sample set. The red triangles (pointing up) represent adsorption, and the blue triangles (pointing down) represent desorption.

The AAO isotherm shown in Figure 3-18 resembles Type C in that the desorption curve is narrowly separated from the adsorption curve and the hysteresis persists across the entire pressure range. However, both the adsorption and desorption curves are very steeply sloped near the saturated vapor pressure. The isotherm shape suggests a homogenous distribution of pore sizes, consisting of pores that are slightly constricted

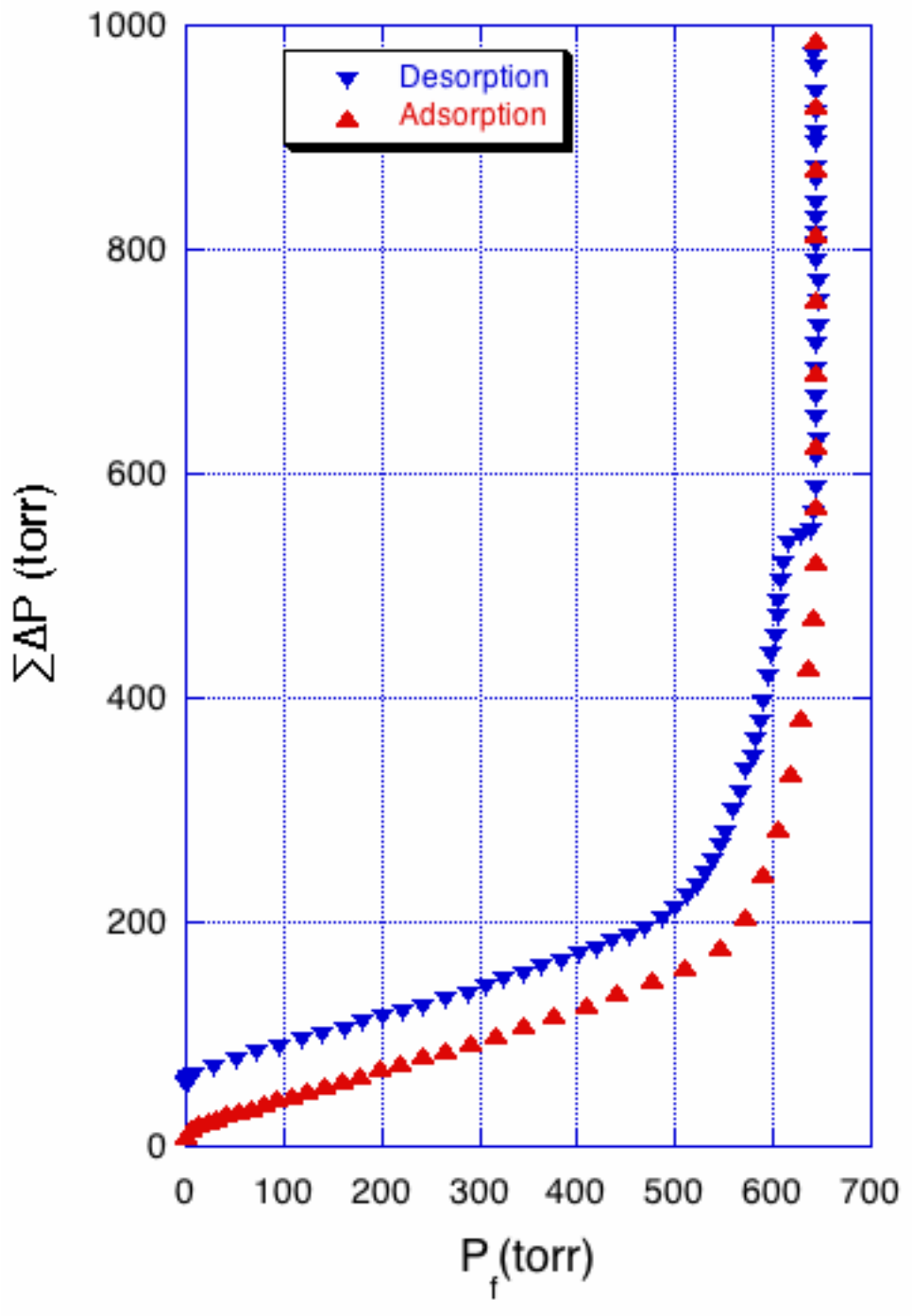


Figure 3-18 Adsorption/Desorption Isotherm of anodized aluminum oxide.

near the surface, or have constricting irregularities within the length of the pore. A noticeable feature of the isotherm is the absence of a lower closure point. It would be expected that a nitrogen isotherm would have its lower closure point at low pressure, since nitrogen is small and could make its way into tiny pores. But, that the desorption loop does not return to zero at all suggests that there could be some residual adsorbate trapped in the substrate. The pore size distribution for these samples is shown in Figure 3-19. The average pore diameter was calculated to be 14 nm, which corresponds exactly with the pore diameter shown on the microscopy image.

3.5 Concluding Remarks

The ultimate goal motivating this work is the study of confinement effects for adsorbed molecules. To do this properly, a porous medium needs to be synthesized with a tunable and homogeneous pore structure. Ideally, the pore size would have a small distribution of less than five nanometers. This study was a preliminary investigation into the synthesis of anodized aluminum oxide with desirable pore structures.

As reported, porous aluminum oxide films were grown on an aluminum substrate, with the possibility of varying the pore diameter. The nature of the pores is highly dependent on the type of acid used as the electrolyte, as well as the concentration of the acid. The samples synthesized in sulfuric acid and oxalic acid showed pores on the order of 10 nm and 60 nm in diameter, respectively. The longer chain dioic acids also

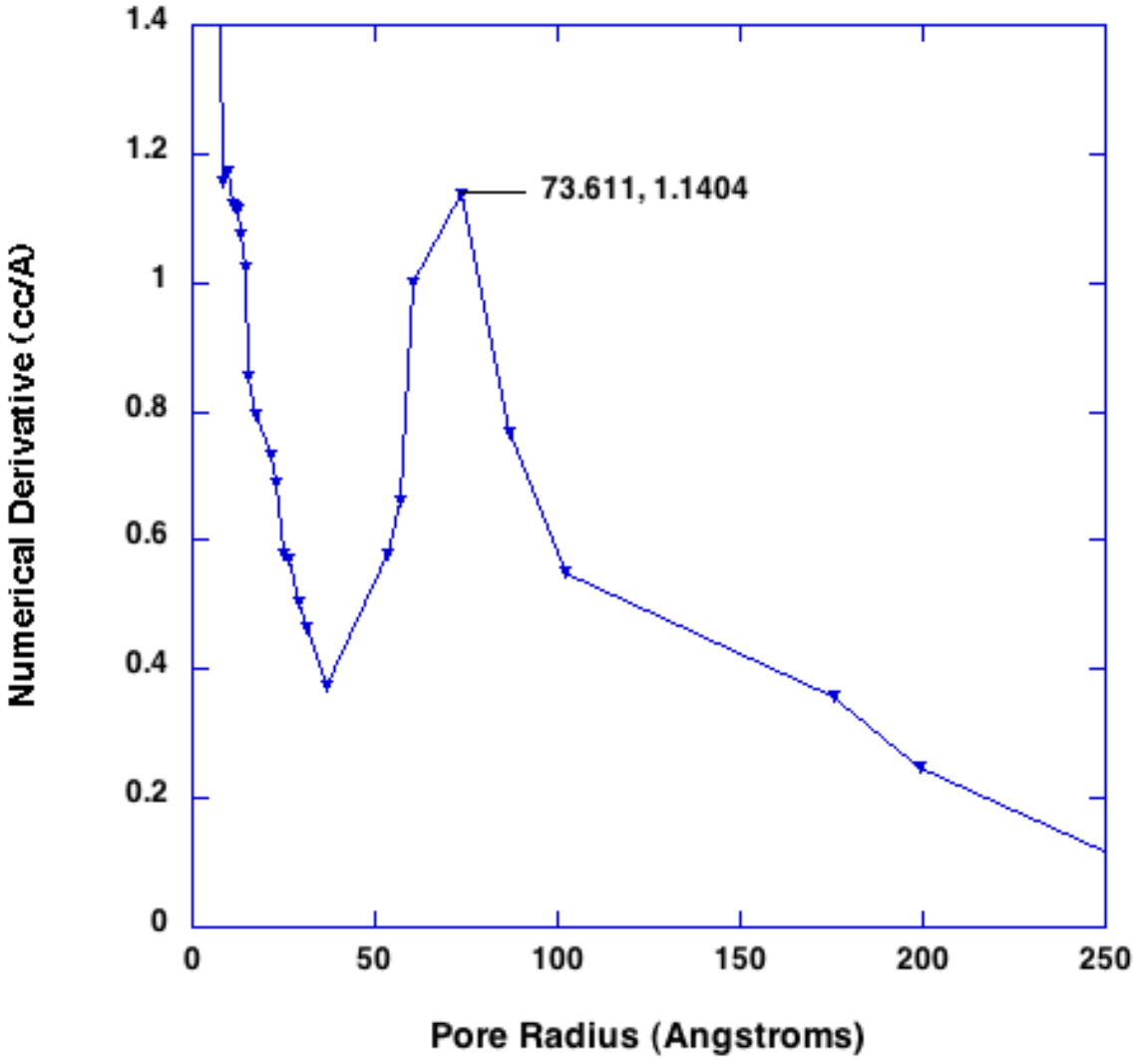


Figure 3-19 Pore Size Distribution of the anodized aluminum oxide.

produced porous films; however, the pores synthesized in this acid media were not as well formed as the films grown in sulfuric and oxalic acids. Possibilities for this result include the strength or size of the dioic acids, or simply the experimental parameters of the synthesis. Finally, it was found that the smallest pores were formed in a dilute sulfuric acid solution, and the minimum pore diameter obtained was 11.1 ± 3.5 nm.

Multiple techniques were used to investigate the size of the pores; including scanning electron microscopy, atomic force microscopy, and adsorption/desorption isotherms. The SEM work, accompanied by EDX, showed that the pores did not extend throughout the entire metal substrate. The length of the synthesized pores was in the range of 5 to 50 microns. All of these techniques (SEM, AFM, and adsorption/desorption isotherms) gave consistent results and were useful for examining the pore size in anodized aluminum oxide.

Much work still needs to be done to completely understand the formation of the AAO. A continuation of this study could include a systematic investigation of how the voltage between the anode and cathode, as well as the distance between the plates, affects the porous membrane. A concentration study on other acids could be useful in understanding the pore formation process. In addition, it would be interesting to change the geometry of the electrochemical cell, i.e. using rods or wires for the anode or cathode. Other appealing work includes the study of the kinetics involved in the formation of the porous membrane and the competition between the dissolution and formation

mechanisms. A well-executed kinetics study could nail down the mechanism involved in pore formation.

Multiple uses of the porous membrane could also be investigated. As mentioned in the introduction, these membranes can be used as templates for nanowire growth. The AAO has the potential of making high aspect ratio nanowires, with possible applications in the electronics industry. In addition, it would be interesting to investigate the effect of temperature, pore size, and adsorbate dependence on the hysteresis observed in the adsorption/desorption isotherms. These projects would represent the next steps in using AAO to study confinement effects.

References

(2008). "Nobelprize.org." from http://nobelprize.org.

Adamson, A. W. and A. P. Gast (1997). Physical Chemistry of Surfaces. New York, John Wiley & Sons, Inc.

Arnold, T., S. Chanaa, et al. (2006). "Structure of an n-butane monolayer adsorbed on magnesium oxide (100)." Physical Review B **74**(8).

Arnold, T., R. E. Cook, et al. (2006). "Neutron scattering and thermodynamic investigations of thin films of n-alkanes adsorbed on MgO(100) surfaces." Physica B-Condensed Matter **385**: 205-207.

Arnold, T., R. E. Cook, et al. (2005). "Thermodynamic investigation of thin films of ethane adsorbed on magnesium oxide." Journal of Physical Chemistry B **109**(18): 8799-8805.

Arnold, T. R. E. C., J. Z. Larese (2005). "Thermodynamic Investigations of Thin Films of Ethane Adsorbed on Magnesium Oxde." Journal of physical Chemistry B **109**: 8788.

Aveyard, R. and D. A. Haydon (1973). An Introduction to the Principles of Surface Chemistry. Cambridge, University Press.

Bancroft, W. D. (1921). Applied Colloid Chemistry: General Theory. New York, McGraw-Hill Book Company, Inc.

Bandyopadhyay, S., A. E. Miller, et al. (1996). "Electrochemically assembled quasi-periodic quantum dot arrays." Nanotechnology **7**(4): 360-371.

Baumgarten, E., F. Weinstrauch, et al. (1977). "Adsorption isotherms of hydrocarbons on g-alumina." Journal of Chromatography **138**(2): 347-54.

Beaglehole, D. (1992). "Liquid to gas transition in the adsorption of alkanes on smooth gold surfaces." Langmuir **8**(4): 1033-5.

Bonaccurso, E., M. Kappl, et al. (2008). "Thin liquid films studied by atomic force microscopy." Current Opinion in Colloid & Interface Science **13**(3): 107-119.

Bovey, E. (1943). "The Anodic Oxidation of Aluminium and Aluminium Alloys." Journal of Scientific Instruments **20**: 92 - 97.

Brunauer, S. (1943). The Adsorption of Gases and Vapors. London, Oxford University Press.

Brunauer, S., P. H. Emmett, et al. (1938). "Adsorption of Gases in Multimolecular Layers." J. Am. Chem. Soc. **60**(2): 309-319.

Butt, H. J., R. Berger, et al. (2007). "Impact of atomic force microscopy on interface and colloid science." Advances in Colloid and Interface Science **133**(2): 91-104.

Chanaa, S. (2008). Materials Chemistry of Nanocubes and Mesoporous Silicas: Characterization and Adsorption Studies. Chemistry. Knoxville, University of Tennessee. **Ph. D.:** 144.

Chi, G. J., S. W. Yao, et al. (2002). "Antibacterial activity of anodized aluminum with deposited silver." Surface and Coatings Technology **157**(2-3): 162-165.

Choy, J.-H., H.-C. Lee, et al. (2001). "A novel synthetic route to TiO2-pillared layered titanate with enhanced photocatalytic activity." Journal of Materials Chemistry **11**: 2232-2234.

Chu, Y. F. and E. Ruckenstein (1976). "Design of Pores in Alumina." Journal of Catalysis **41**: 384-396.

Cook, R. E. M. T. F. T., J. Z. Larese (submitted 2008). "Thermodynamic and Neuton Investigation of n-Petane Thin Films Adsorbed on Magnesium Oxide Powders ".

Cooke, P. M. (1996). "Chemical microscopy." Analytical Chemistry **68**(12): R333-R378.

Cooke, P. M. (1998). "Chemical microscopy." Analytical Chemistry **70**(12): 385R-423R.

Cox, P. A. and V. E. Hendrich (1994). The Surface Science of Metal Oxides. New York, Cambridge University Press.

Dabrowski, A. (2001). "Adsorption - from theory to practice." Advances in Colloid and Interface Science **93**(1-3): 135-224.

Dawson, P. H. (1977). "SIMS and EID observations of propane adsorbed on aluminum." Journal of Vacuum Science and Technology **14**(3): 786-8.

Dedkov, G. V. (2000). "Experimental and theoretical aspects of the modern nanotribology." Physica Status Solidi a-Applied Research **179**(1): 3-75.

Derose, J. A. and R. M. Leblanc (1995). "SCANNING TUNNELING AND ATOMIC-FORCE MICROSCOPY STUDIES OF LANGMUIR-BLODGETT-FILMS." Surface Science Reports **22**(3): 73-126.

Di Corcia, A. and R. Samperi (1973). "Hydrogen-treated graphitized carbon blacks. Limiting isosteric heats and entropy changes upon adsorption of hydrocarbons." Journal of Physical Chemistry **77**(10): 1301-6.

Flood, E. A., Ed. (1967). The Solid-Gas Interface. New York, Marcel Dekker, Inc.

Freitag, A. and J. Z. Larese (2000). "Layer growth of methane on MgO: An adsorption isotherm study." Phys. Rev. B **62**(12): 8360-8365.

Freitag, A. and J. Z. Larese (2000). "Layer growth of methane on MgO: An adsorption

isotherm study." Physical Review B **62**(12): 8360-8365.

Friedbacher, G. and H. Fuchs (1999). "Classification of scanning probe microscopies - (Technical report)." Pure and Applied Chemistry **71**(7): 1337-1357.

Frommer, J. (1992). "SCANNING TUNNELING MICROSCOPY AND ATOMIC FORCE MICROSCOPY IN ORGANIC-CHEMISTRY." Angewandte Chemie-International Edition in English **31**(10): 1298-1328.

Gapin, A. I., X. R. Ye, et al. (2006). CoPt patterned media in anodized aluminum oxide templates, AIP.

Grande, C. A., V. M. T. M. Silva, et al. (2003). "Adsorption of propane and propylene onto carbon molecular sieve." Carbon **41**(13): 2533-2545.

Hamza, A. V., H. P. Steinruck, et al. (1987). "The dynamics of the dissociative adsorption of alkanes on iridium(110)." Journal of Chemical Physics **86**(11): 6506-14.

Hansma, H. G. (2001). "SURFACE BIOLOGY OF DNA BY ATOMIC FORCE MICROSCOPY." Annual Review of Physical Chemistry **52**(1): 71-92.

Hawkes, P. W. (1997). Electron microscopy and analysis: the first 100 years. Electron Microscopy and Analysis 1997**:** 1-8.

Herzberg, G. (1955). "Heinrich Kayser. 1853-1940." Biographical Memoirs of Fellows of the Royal Society **1**: 135-143.

Ho, W. (2002). "Single-molecule chemistry." Journal of Chemical Physics **117**(24): 11033-11061.

Hoar, T. P. and N. F. Mott (1959). "A mechanism for the formation of porous anodic

oxide films on aluminium." Journal of Physics and Chemistry of Solids **9**(2): 97-99.

Holmes, F. L. and T. H. Levere (2000). Instruments and Experimentation in the History of Chemistry, MIT Press.

Holmes, J. M. and R. A. Beebe (1957). "An Example of Desorption Hysteresis at Low Relative Pressures on a Non-porous Adsorbent: Ammonia on Graphitized Carbon Black." J. Phys. Chem. **61**(12): 1684-1686.

Hoory, S. E. and J. M. Prausnitz (1967). "Adsorption of hydrocarbons on graphitized carbon*." Transactions of the Faraday Society **63**(2): 455-60.

Hopkins, B. J. and G. R. Shah (1972). "Adsorption of methane, ethane, and propane on the (100) face of a tungsten single crystal*." Vacuum **22**(7): 267-71.

Jahanmir, J., B. G. Haggar, et al. (1992). "THE SCANNING PROBE MICROSCOPE." Scanning Microscopy **6**(3): 625-660.

Jalili, N. and K. Laxminarayana (2004). "A review of atomic force microscopy imaging systems: application to molecular metrology and biological sciences." Mechatronics **14**(8): 907-945.

Joy, D. C. (1997). "Scanning electron microscopy for materials characterization." Current Opinion in Solid State & Materials Science **2**(4): 465-468.

Keller, F., M. S. Hunter, et al. (1953). "Structural Features of Oxide Coatings on Aluminum." Journal of the Electrochemical Society **100**: 411.

Kiselev, A. V. (1961). "Surface Chemistry, Adsorption Energy, and Adsorption Equilibria." Quarterly Reviews **15**: 99-124.

Kittel, C. (1996). Introduction to Solid State Physics. New York, John Wiley & Sons, Inc.

Knoll, M. (1935). "Aufladepotentiel und Sekundäremission elektronenbestrahlter Körper." Zeitschrift fur technische Physik **16**: 467-475.

Kolasinski, K. W. (2002). Surface Science: Foundations of Catalysis and Nanoscience. West Sussix, England, John Wiley & Sons, Ltd.

Kunnmann, W. and J. Z. Larese (2001). U.S.

L.H., C. (1938). Journal of the American Chemical Society **60**: 433.

Lal, M. and D. Spencer (1974). "Interaction of alkanes with graphite." Journal of the Chemical Society, Faraday Transactions 2: Molecular and Chemical Physics **70**(5): 910-19.

Lambert, B. and A. M. Clark (1929). "Studies of Gas-Solid Equilibria. Part II. Pressure-Concentration Equilibria between Benzene and (a) Ferric Oxide Gel, (b) Silica Gel, Directly Determined under Isothermal Conditions." Proceedings of the Royal Society of London. Series A, Containing Papers of a Mathematical and Physical Character **122**(790): 497-512.

Lane, N. (2003). Benjamin Franklin, Civic Scientist. Physics Today. **56:** 41-46.

Langmuir, I. (1918). "THE ADSORPTION OF GASES ON PLANE SURFACES OF GLASS, MICA AND PLATINUM." J. Am. Chem. Soc. **40**(9): 1361-1403.

Larese, J. Z. (1998). "Neutron scattering studies of the structure and dynamics of methane absorbed on MgO(100) surfaces." Physica B **248**: 297-303.

Larher, Y. (1992). Physics and Chemistry of Materials with Low-Dimensional Structures

16: 261.

Li, A. P., F. Muller, et al. (1998). "Hexagonal pore arrays with a 50-420 nm interpore distance formed by self-organization in anodic alumina." Journal of Applied Physics **84**(11): 6023-6026.

Li, F., L. Zhang, et al. (1998). "On the Growth of Highly Ordered Pores in Anodized Aluminum Oxide." Chem. Mater. **10**: 2470-2480.

Li, F., L. Zhang, et al. (1998). "On the Growth of Highly Ordered Pores in Anodized Aluminum Oxide." Chem. Mater. **10**(9): 2470-2480.

Louder, D. R. and B. A. Parkinson (1994). "SCANNING PROBE MICROSCOPY." Analytical Chemistry **66**(12): R84-R105.

Lowell, S., J. E. Shields, et al. (2004). Characterization of Porous Solids and Powders: Surface Area, Pore Size and Density, Springer.

Majer, V. and V. Svoboda (1985). Enthalpies of Vaporization of Organic Compounds: A Critical Review and Data Compilation. Oxford, Blackwell Scientific Publications.

Masuda, H., H. Yamada, et al. (1997). "Highly ordered nanochannel-array architecture in anodic alumina." Applied Physics Letters **71**(19): 2770-2772.

Mayorga, G. D. and D. L. Peterson (1972). "Adsorption in mordenite. II. Gas chromatographic measurement of limiting heats of adsorption of nonpolar molecules." Journal of Physical Chemistry **76**(11): 1647-50.

McMullan, D. (2004). A history of the scanning electron microscope, 1928-1965. Advances in Imaging and Electron Physics, Vol 133. **133:** 523-545.

Murat, M. (1975). "SCANNING ELECTRON-MICROSCOPE - PRINCIPLES,

APPARATUS, USE IN CHEMISTRY OF SOLIDS AND MATERIALS." Chimica & L Industria **57**(2): 99-113.

Mursic, Z., M. Y. M. Lee, et al. (1996). "Computer-controlled apparatus for performing high-resolution adsorption isotherms." Review of Scientific Instruments **67**(5): 1886-1890.

Myers, A. L. and J. M. Prausnitz (1965). "Hindered rotation in physical adsorption*." Transactions of the Faraday Society **61**(508): 755-64.

Nakahara, T., M. Hirata, et al. (1974). "Adsorption of Hydrocarbons on Carbon Molecular Sieve." Journal of Chemical and Engineering Data **19**(4): 310-313.

Newbury, D. E. and D. B. Williams (2000). "The electron microscope: The materials characterization tool of the millennium." Acta Materialia **48**(1): 323-346.

Oatley, C. W. (1982). "THE EARLY HISTORY OF THE SCANNING ELECTRON-MICROSCOPE." Journal of Applied Physics **53**(2): R1-R13.

Oatley, C. W., D. McMullan, et al. (1985). "THE DEVELOPMENT OF THE SCANNING ELECTRON-MICROSCOPE." Advances in Imaging and Electron Physics: 443-482.

Ohgai, T., L. Gravier, et al. (2005). "CdTe semiconductor nanowires and NiFe ferro-magnetic metal nanowires electrodeposited into cylindrical nano-pores on the surface of anodized aluminum." Journal of Applied Electrochemistry **35**(5): 479-485.

Pacchioni, G. (2001). Theory of point defects at the MgO surface. Oxide Surfaces. D. P. Woodruff. Amsterdam, Elsevier. **9**.

Peters, T. A. (1981). "THE SCANNING ELECTRON-MICROSCOPE - A POWERFUL TOOL OF THE MINERALOGIST - AN OVERVIEW." Scanning Electron Microscopy: 603-623.

Ross, S., J. K. Saelens, et al. (1962). Journal of Physical Chemistry **66**: 696.

Sault, A. G. and D. W. Goodman (1988). "Dissociative adsorption of alkanes on nickel(100): comparison with molecular beam results." Journal of Chemical Physics **88**(11): 7232-9.

Schramm, L. L. (2004). "Famous Colloid & Interface Scientists." 2008, from http://www.ucalgary.ca/~schramm/biogrs.htm.

Seiler, H. (1983). "SECONDARY-ELECTRON EMISSION IN THE SCANNING ELECTRON-MICROSCOPE." Journal of Applied Physics **54**(11): R1-R18.

Sheasby, P. G. and R. Pinner (2001). The Surface Treatment and Finishing of Aluminum and its Alloys. Materials Park, Ohio, ASM International & Finishing Publications.

Stevenson, R. M. and S. Malanowski (1987). Handbook of the Thermodynamics of Organic Compounds. New York, Elsevier.

Sun, H. (1998). "COMPASS: An ab Initio Force-Field Optimized for Condensed-Phase Applications-Overview with Details on Alkane and Benzene Compounds." J. Phys. Chem. B **102**(38): 7338-7364.

Szuromi, P. D., J. R. Engstrom, et al. (1985). "Adsorption and reaction of n-alkanes on the platinum(110)-(1 * 2) surface." Journal of Physical Chemistry **89**(12): 2497-502.

Taylor, G. L. and J. H. Atkins (1966). "Adsorption of propane on carbon black*." Journal

of Physical Chemistry **70**(5): 1678-80.

Thomas, J. M. (1996). Principles and Practice of Heterogeneous Catalysis, Wiley-VCH.

University, P. (2006). "Scanning Electron Microscope."

Verwey, E. J. W. (1935). "Electrolytic conduction of a solid insulator at high fields The formation of the anodic oxide film on aluminium." Physica **2**(1-12): 1059-1063.

Weiser, H. B. (1946). Colloid Chemistry (A Textbook). New York, John Wiley & Sons, Inc.

Wiesendanger, R. (1999). "Surface magnetism at the nanometer and atomic scale." Current Opinion in Solid State & Materials Science **4**(5): 435-440.

Wittrig, T. S., P. D. Szuromi, et al. (1982). "The interaction of ethane, propane, isobutane, and neopentane with the (110) surface of iridium." Journal of Chemical Physics **76**(6): 3305-15.

Yaron, P. N., M. T. F. Telling, et al. (2006). "Thermodynamic investigation of n-hexane thin films adsorbed on magnesium oxide." Langmuir **22**(17): 7203-7207.

Yeung, K. L. and N. Yao (2004). "Scanning probe microscopy in catalysis." Journal of Nanoscience and Nanotechnology **4**(7): 647-690.

Zsigmondy, Z. (1911). Anorg. Chem. **71**: 356.

Vita

Michael John Felty was born Michael John Farinelli on Long Island, New York in 1979 to Jeanne Felty. He spent a majority of his childhood in Savannah, Georgia and Greenup County, Kentucky. The world of science first sparked his interest while attending Greenup County High School. He pursued his Bachelors of Science degree at Western Kentucky University, where he majored in Chemistry and Physics, and minored in Mathematics. At WKU, he worked with Thandi Buthelezi, studying the UV-Vis spectrum and Laser Induced Fluorescence of crown ethers. He graduated from WKU in 2002, and went on to accept a chemical physics fellowship and a graduate teaching assistantship at the University of Tennessee Knoxville. At UTK, he performed his doctoral research under the direction of John Z. Larese. In August 2006, Michael was adopted by his stepfather George (Danny) Felty and married the love of his life, Jenee. He will graduate with a Doctor of Philosophy degree in Chemistry, with a concentration in Chemical Physics, in December 2008.